Towards the Quantum Regime: Ultracoherent Diamond Spin-Mechanical Resonators

by

Xinzhu Li

A dissertation accepted and approved in partial fulfillment of the requirements for the degree of

Doctor of Philosophy

in Physics

Dissertation Committee:

Daniel Steck, Chair

Hailin Wang, Advisor

Jens Noeckel, Core Member

Andy Marcus, Institutional Representative

University of Oregon

Spring 2025

DISSERTATION ABSTRACT

Xinzhu Li

Doctor of Philosophy in Physics

Title: Towards the Quantum Regime: Ultracoherent Diamond Spin-Mechanical Resonators

Hybrid quantum systems combine the advantages of individual components and pave the road to practical quantum computing and information processing. Among varieties of candidates, spin-mechanical systems based on color centers in diamond utilize the extraordinary optical properties of nitrogen-vacancy centers or silicon-vacancy centers in diamond, combined with the advantages of mechanical systems. To this date, quantum computers based on color centers in diamond have not been achieved. One central challenge is to reach the quantum regime of spin-phonon coupling where effects of single phonons become important. This dissertation will present the efforts in developing ultracoherent diamond spin-mechanical resonators as the cornerstone of reaching this regime. Through the design, fabrication and characterization of diamond nanomechanical resonators with phononic bandgap engineering, we achieved highest up-to-date quality factors of above 10^6 in diamond cantilevers at frequencies of up to 100MHz and 10^7 in Lamb wave resonators at frequencies of 1GHz. For the latter, we developed an all-optical approach that excites the fundamental compression mode with optical gradient force in a Lamb

wave resonator. This thesis will then discuss the applications of our spin-mechanical system in mechanical sensing and quantum networking. Combined with superior optial properties of nitrogen vacancy and silicon vacancy centers in diamond, spin-mechanical system enables a promising platform for spin-based quantum computing and quantum networking.

This dissertation contains previously published as well as unpublished co-authored materials.

CURRICULUM VITAE

NAME OF AUTHOR: Xinzhu Li

GRADUATE AND UNDERGRADUATE SCHOOLS ATTENDED:

University of Oregon, Eugene, OR, USA
University of Science and Technology of China, Anhui, China

DEGREES AWARDED:

Doctor of Philosophy, Physics, 2025, University of Oregon
Bachelor of Science, Physics, 2018, University of Science and Technology of China

AREAS OF SPECIAL INTEREST:

Nanomechanical resonators
Color centers in diamond
Hybrid quantum systems

PROFESSIONAL EXPERIENCE:

Research Assistant, University of Oregon, 2019 – 2025

Teaching Assistant, University of Oregon, 2019 – 2025

GRANTS, AWARDS AND HONORS:

EMANUEL Optical, Molecular, and Quantum Sciences Scholarship, University of Oregon, 2024

USTC Excellent Bachelor Thesis Award (top 5%), University of Science and Technology of China, 2018

PUBLICATIONS:

Shu-Hao Wu, Xinzhu Li, Ian Gallagher, Benjamin Lawrie, and Hailin Wang. Coherent population trapping and spin relaxation of a silicon vacancy center in diamond at millikelvin temperatures. *Physical Review B*, 111(3): 035421, 2025.

Shu-Hao Wu, Xinzhu Li, Ian Gallagher, Lexington Mandachi, Benjamin Lawrie, and Hailin Wang. Experimental determination of energy-level structures of diamond silicon-vacancy centers in off-axis magnetic fields. *Physical Review B*, 111(15): 155426, 2025.

Xinzhu Li, Ignas Lekavicius, Jens Noeckel, and Hailin Wang. Ultracoherent gigahertz diamond spin-mechanical lamb wave resonators. *Nano Letters*, 24(35): 10995–11001, 2024.

Xinzhu Li and Hailin Wang. Mechanical photoluminescence excitation spectra of a strongly driven spin-mechanical system. *Physical Review Applied*, 19(6): 064068, 2023.

Ethan Turner, Shu-Hao Wu, Xinzhu Li, Hailin Wang. Real-time magnetometry with coherent population trapping in a nitrogen-vacancy center. *Physical Review A*, 105(1): L010601, 2022.

Ethan Turner, Shu-Hao Wu, Xinzhu Li, Hailin Wang. Spin-based continuous Bayesian magnetic-field estimations aided by feedback control. *Physical Review A*, 106(5): 052603, 2022.

Xinzhu Li, Ignas Lekavicius, and Hailin Wang. Diamond nanomechanical resonators protected by a phononic band gap. *Nano Letters*, 22(24): 10163–10166, 2022.

Xinzhu Li, Mark C Kuzyk, and Hailin Wang. Honeycomblike phononic networks of spins with closed mechanical subsystems. *Physical Review Applied*, 11(6): 064037, 2019

ACKNOWLEDGEMENTS

I would like to first thank my advisor, Prof. Hailin Wang, for providing tremendous amounts of help and support throughout my entire PhD study. I wouldn't have gained such valuable skills and knowledge in both experimental and theoretic physics without his mentorship, timely guidance, unwavering support and great physics insight. I am deeply grateful for all I've learnt from Wang Lab.

I thank Ignas Lekavicius for teaching and providing answers to my fabrication questions. I thank my labmate Shuhao for sharing his wisdom in experiments, theories, coding and many joyful conversations about quantum and grad school. I would like to thank our collaborator Dr. Benjamin Lawrie and Oak Ridge National Laboratory for their substantial support and assistance with our experiments. I am deeply grateful to Prof. Jens for his constant kindness, willingness to help, and valuable input on our project. Many thanks to my colleagues Ethan, Abby, Lexi, and Philip for the many joyful and memorable conversations.

I would like to thank all my committee members for their great help. I would like to thank OMQ staff Jorjie for her patience to my many purchase requests. I thank Stephanie Majewski for her very kind help and support. I thank all UO table tennis club members for bringing me happiness outside of work. I thank my families for their support and understanding.

TABLE OF CONTENTS

LIST OF FIGURES

Figure Page

CHAPTER I

INTRODUCTION

1.1 Quantum Computation

As classical computers revolutionize s to obtain greater computation power - building a quantum computer. This goal requires the finding of an optimal system that is capable of storing, processing and transmitting information [12], and there is no easy answer on what the best quantum "hardware" will be leading to the final practical quantum computers.

For the development of various physical platforms for quantum computing, a few common prerequisites are well-known [12, 13]: Firstly, a quantum computer's internal operation while under the programmer's control, must otherwise be isolated from the rest of the universe. This is for preventing large decoherence rate of the system compared to the time needed for the computation. Second, the computer must operate in a Hilbert space whose dimensions can grow exponentially without an exponential cost in resources. Superposition and entanglement facilitate this requirement, but scalable 'classical' resources are also important, demanding engineering techniques for large-scale infrastructures. Besides these, the system needs available a universal set of quantum logic gates, and it must be possible to extract entropy from the computer to maintain its quantum state, namely correctability.

A number of physical platforms have seen rapid developments in the last few decades [14, 15, 16, 17, 18]. Superconducting qubits working at ultralow temperatures feature macroscopic size and are made of superconducting circuits that can be controlled by microwave and tuned by adjusting inductances or capacitance [19]. The

qubits feature fast operation speed and can be readily fabricated with semiconductor technologies [20]. Trapped-ion qubits on the other hand are atomic-like systems that are operated by lasers cooling and trapping charged particles [21]. They feature high gate-fidelities but suffer from difficulties in scalability and need many lasers [15]. Other atom-like systems include neutral atom systems [17] and silicon quantum dots [22], where neutral-atom arrays can realize very high number of qubits connected in two or even three dimensions, but face difficulties in programming and control of individual qubits. Silicon quantum dots on the other hand benefit greatly from the mature and high precision semiconductor fabrication procedures [16]. Other physical platforms for quantum computing include topological qubits which can greatly reduce errors [23] and diamond defect centers that can feature long spin coherence time at even room temperature [3]. Fig. 1.1 shows an overview and comparison of different quantum "hardware" platforms that have been developed in the past few decades [1]. Among different choices, atom-like systems feature unique benefits.

1.2 Atomic-Like Quantum Systems

Trapped-ion systems have the potential of making a great quantum computer for their perfect reproducibility, controllability with lasers and ultra-long lifetime, benefitting from the abilities of localizing individual ions for a long period of time [15]. The ion-trapping technology gave rise to the world's very first quantum logic gates [24], following shortly after the discoveries of Shor's algorithm [25]. Different types of ion traps including Paul traps and Penning traps create various configurations of fields including static, oscillating electric or magnetic fields, trapping the ions in a specific location. For quantum operations, laser cooling techniques can cool the trapped ions to near zero temperatures to minimize motion

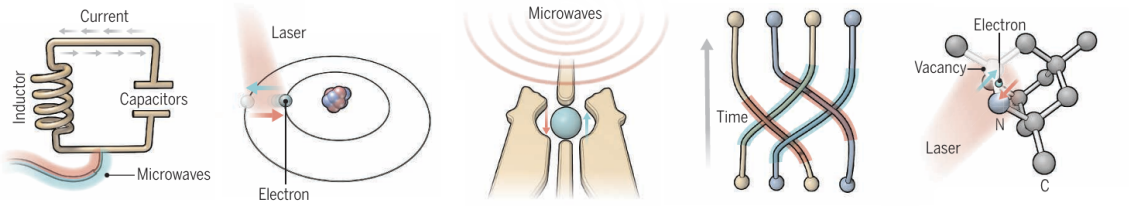

	Superconducting loops	**Trapped ions**	**Silicon quantum dots**	**Topological qubits**	**Diamond vacancies**
	A resistance-free current oscillates back and forth around a circuit loop. An injected microwave signal excites the current into super-position states.	Electrically charged atoms, or ions, have quantum energies that depend on the location of electrons. Tuned lasers cool and trap the ions, and put them in superposition states.	These "artificial atoms" are made by adding an electron to a small piece of pure silicon. Microwaves control the electron's quantum state.	Quasiparticles can be seen in the behavior of electrons channeled through semi-conductor structures.Their braided paths can encode quantum information.	A nitrogen atom and a vacancy add an electron to a diamond lattice. Its quantum spin state, along with those of nearby carbon nuclei, can be controlled with light.
Longevity (seconds)	0.00005	>1000	0.03	N/A	10
Logic success rate	99.4%	99.9%	~99%	N/A	99.2%
Number entangled	9	14	2	N/A	6
Company support	Google, IBM, Quantum Circuits	ionQ	Intel	Microsoft, Bell Labs	Quantum Diamond Technologies
Pros	Fast working. Build on existing semiconductor industry.	Very stable. Highest achieved gate fidelities.	Stable. Build on existing semiconductor industry.	Greatly reduce errors.	Can operate at room temperature.
Cons	Collapse easily and must be kept cold.	Slow operation. Many lasers are needed.	Only a few entangled. Must be kept cold.	Existence not yet confirmed.	Difficult to entangle.

FIGURE 1.1. A comparison of different physical platforms for the realization of practical quantum computing, each with their own characteristics, strengths and weaknesses. Taken from Ref. [1].

and facilitate precise control. $|0\rangle$ and $|1\rangle$ qubit states are represented by different internal electronic states of ions, where initialization and readout of qubit states can be performed with lasers and microwaves controlling the internal and motional states of ions.

Entanglement among trapped ions can be mediated by their collective motional modes as a bus and happen through the mutual Coulomb interaction. Quantum gates such as the CNOT two-qubit gate can be generated with laser interactions and have been demonstrated with high fidelity under several schemes for both optical qubits [26] and hyperfine qubits [27]. Overall, advantages of trapped ion qubits include the exceptionally long coherence times, high fidelity quantum gates,

straightforward state preparation and readout process and the identicality of all ions of a given species and isotope which enhances the qubits reproductivity [15].

Much similar to trapped ions in vacuum, spin qubits in semiconductors including silicon quantum dots and defect centers in diamond are atomic systems trapped in a solid. The well-developed growth of ultra-pure GaAs/AlGaAs heterostructures gave rise to the first semiconductor qubits formed with group III/V materials [28]. Heterostructures can confine electrons and holes into reduced dimensions and form a quantum dot (QD) which contains a single spin. In contrast, color centers in diamond are naturally formed or artificially implanted atomic defects that reside in the wide band gap (∼5.5eV) of diamond. These defect centers are optically active and can be manipulated with lasers for quantum control such as state initialization and population transfer. Especially, negatively charged nitrogen vacancy centers (NV^-) have long spin coherence time at even room temperature and have drawn substantial attention for quantum sensing and quantum information processing uses [3]. Group IV defect centers such as negatively charged silicon vacancy (SiV^-) [29] and tin vacancy [30] otherwise show strong strain coupling to ground-state orbital degrees of freedom while presenting better optical properties such as a prominent zero-phonon line (ZPL). Compared to trapped-ion systems or other qubit platforms, spins in semiconductors benefit from the host lattice of different materials which could give widely tunable and unique qubit properties.

1.3 Hybrid Quantum Systems

1.3.1 Overview

Different platforms provide unique advantages in spin coherence time, operation speed, controllability and scalability. The ultimate "hardware" for a quantum

computer will likely to be a hybrid platform combining the advantages of its individual components. For example, with superconducting qubits processing fast algorithms, solid-state qubits with long coherence time for storing information and photons interchanging information between different parts. "One can imagine we'll have an environment in which several types of qubits exist and play different roles." [1]

An interface will be required to transfer information and facilitate interactions. A natural candidate is photons or often called "flying qubits". Photons have been successfully used in optical communications and are compatible with free-space and fiber optics technologies [18, 31]. However, information transfer between quantum systems in disparate energy levels remains difficult [2]. Another candidate of quantum interface – phonons, provide a solution to this due to their wide coupling capabilities to different quantum systems. In particular, phonons couple to photons through radiation pressure force, to charge qubits with Coulomb interactions and to solid-state qubits through stress and strain [2], as is shown in Fig. 1.2.

The most distinct advantage of phonons versus photons is the immunity to vacuum scattering loss. Besides this, compared to electromagnetic waves, mechanical oscillations also enable transitions that are forbidden by optical selection rules, for example spin non-conserving transitions in solid-state qubits. The orders-of-magnitude slower velocity of sound compared to light also facilitates time-tagging measurements in some experiments.

Hybrid quantum systems facilitated by mechanical waves have so far been demonstrated with different qubit systems, including superconducting circuits [32], quantum dots [33] and solid-state spins [34]. In the ensuing chapters, we will discuss

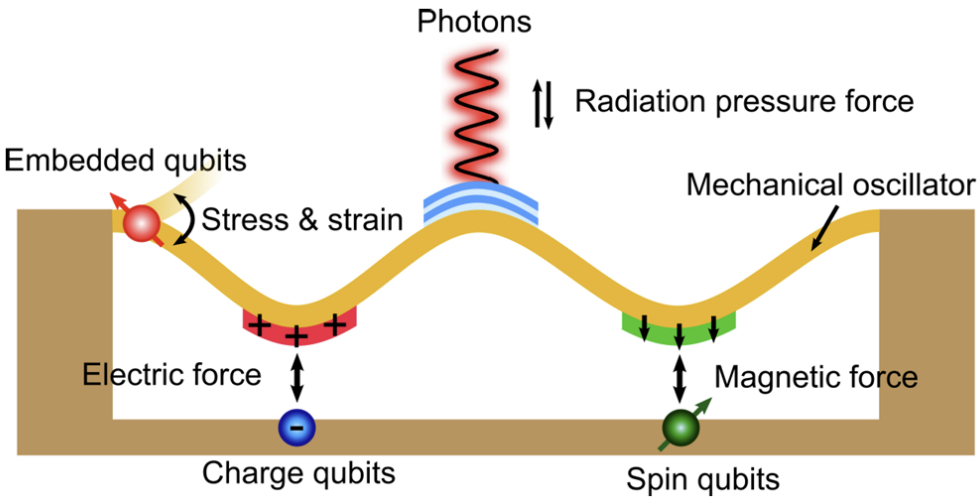

FIGURE 1.2. Phonons as a quantum interface interacting with different systems including photons, charge qubits, spin qubits and embedded qubits through various types of interactions. Taken from Fig. 1 in Ref. [2].

briefly electromechanical systems then introduce spin-mechanical systems as our focus in this thesis.

1.3.2 Electromechanical Systems

Hybrid mechanical systems with superconducting qubits have made significant progress in recent years [32, 35, 36, 37]. Mechanical motions can couple to superconducting circuits through Lorentz force or electrostatic interactions. Coupling at the single-phonon level has been realized, such as the generation of phonon Fock states and phonon-mediated entanglement between two superconducting qubits through deterministic emission and capture of surface acoustic wave (SAW) phonons [32]. Entanglement of two mechanical drumheads have been demonstrated [38], where quantum state tomography was performed through nearly quantum-limited measurements and shows direct observation of entanglement. These hybrid electromechanical systems with quantum-regime coupling contribute

to fundamental tests of quantum mechanics, inspire hybrid quantum networks with phonons and further form the steppingstone towards phonon-based quantum communication protocols.

1.3.3 Spin-Mechanical Systems

The remarkable experimental success of electromechanical systems inspired the efforts on spin-mechanical hybrid systems. A spin-mechanical system is where mechanical oscillations couple to spins, including crystal defect centers and quantum dots, and one prominent example is the negatively charged nitrogen-vacancy centers (NV^-) – by embedding color centers inside diamond nanomechanical resonators such as cantilevers or nanobeams [2, 39]. Crystal strain created by resonator motions could change the effective potential the color center goes through, altering the energy level positions and creating phonon sidebands [40]. Fig. 1.3 shows a simple diagram of a spin-mechanical resonator where different types of color centers in diamond could be embedded near the clamping area of the cantilever, where the strain value is the highest. For a two-level system coupling to a mechanical mode, the strength of spin-phonon coupling can be characterized by a dimensionless parameter – Cooperativity C, defined as

$$C = 4g^2/(\gamma_s\gamma_m) \tag{1.1}$$

Where γ_s and γ_m are the decoherence rates of the two-level system and the mechanical resonance, g is the single-phonon coupling rate defined by

$$g = x_{zpf}Dk_m \tag{1.2}$$

where x_{zpf} is the zero-point fluctuation, D is the diamond deformation potential characterizing how much of energy level changes for a given strain, and k_m is the wave vector. To reach the quantum regime of spin-phonon coupling, cooperativity C is expected to be larger than 1 where quantum control can happen at the single phonon level. This is also the regime leading to applications such as cooling the mechanical resonator to its quantum ground state, long-range phonon-mediated spin–spin interactions or generating non-Gaussian quantum states like Fock states.

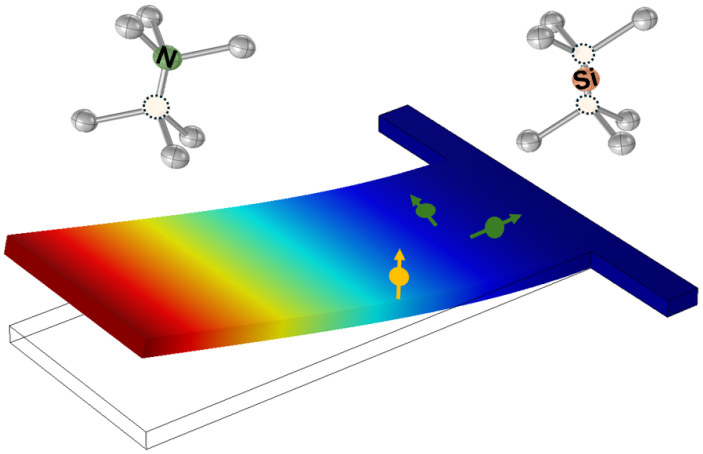

FIGURE 1.3. A simple diagram of a diamond spin-mechanical resonator. Different types of solid-state spin qubits (SiV^- and NV^-) can be embedded near the base of a diamond cantilever, where the strain value is the highest.

From expression (1), it is straightforward to see what factors determine the value of cooperativity. A small γ_s means a stable spin system with low decoherence rate, a small g means bigger zero-point fluctuations (ZPF) which requires smaller mass of mechanical oscillators since x_{zpf} is defined as

$$x_{zpf} = \sqrt{\hbar/(2m_{eff}\omega_m)} \tag{1.3}$$

Smaller masses also offer the mechanical resonator the ability to better detect small external perturbations and therefore function as great force or mass sensors [41]. Meanwhile, a small γ_m means coherent mechanical resonators with high quality factors (Q-factor) – defined as the ratio of the mechanical resonance frequency over the full-width at half maximum (FWHM). Q-factors characterize the dissipation of energy of the mechanical resonator to its surrounding environment, therefore the higher the Q, the longer the mechanical lifetime and the better a mechanical oscillator can store information.

In addition to smaller mass and high Q-factor, another critical factor is the frequency. For applications requiring the resolved sideband regime, for example coupling of phonons to the orbital transitions of NV^- or realizing phonon cooling or lasing of mechanical resonators, frequencies of the mechanical oscillators need to be sufficiently high [42].

In summary, spin-mechanical systems as hybrid quantum systems could harvest the extraordinary coherence properties of solid-state qubits while making use of the advantages of phonons compared to photons. The realization of the quantum regime of spin-phonon coupling will ultimately hinge on the development of ultra-coherent spin-mechanical resonators featuring stable, coherent spin systems with high-Q, low effective mass mechanical modes.

1.4 Dissertation Overview

In this dissertation, I will report our progress on the development of an ultra-coherent diamond spin-mechanical resonator for the pursuit of spin-phonon coupling studies in the quantum regime. Solid-state defect centers in diamond including NV^- and SiV^- are utilized as stable and coherent spin systems while high-Q mechanical

systems including cantilevers and Lamb wave resonators are developed with the design of phononic band gaps.

Chapter II gives an overview on color centers in diamond including NV^- and SiV^-. Energy level structures and experimental quantum control protocols will be discussed in detail, along with the confocal microscope setup. Theories on strain coupling of color centers in diamond are presented as preparation for the following chapters on spin-phonon coupling and mechanical resonators.

Chapter III covers the review of nanomechanical resonators based on different material platforms and geometries. Loss mechanisms are discussed, leading to the key technique for enabling high Q-factor mechanical resonators – phononic band gap engineering.

Chapter IV follows the last chapter and focuses on the procedures for fabricating diamond nanomechanical resonators with phononic band gap structures. Detailed descriptions on fabrication steps, techniques and parameters control will be presented in detail.

Chapter V then presents the work of implementing phononic band gap structures on diamond cantilevers. We talk about our design, fabrication and characterization of diamond mechanical modes with a Q-factor as high as 10^6 at frequencies of up to 100MHz. Temperature dependence and characterization will also be presented. This part of work was done in collaboration with Ignas Lekavicius and Hailin Wang and has been published in Nano Letters as Ref. [43].

Chapter VI presents the work on a gigahertz frequency ultra-coherent spin-mechanical resonator with the geometry of a Lamb wave resonator. The characterization and detection of in-plane compression motion is made possible with the use of optical gradient force from a highly focused telecom laser beam and strain

coupling to a silicon vacancy center. A Q-factor of 10^7 is reported for a mechanical resonance at 977MHz. This part of work was done in collaboration with Ignas Lekavicius, Jens Noeckel and Hailin Wang and has been published in Nano Letters as Ref. [44].

Chapter VII shows experimental studies of a strongly driven spin-mechanical system, where a nitrogen vacancy (NV^-) center couples to a diamond cantilever. This work shows the potential application of a spin-mechanical system in mechanical sensing, for example mass and frequency sensing. This part of work was done in collaboration with Hailin Wang and has been published in Physical Review Applied as Ref. [45].

Chapter VIII presents the design of a diamond honeycomb-like phononic network of spins, where a nanomechanical oscillator couples to three phononic waveguides with different band structures. This work shows the potential application of spin-mechanical systems in quantum networking and computing, overcoming the scaling problems with large mechanical systems. This part of work was done in collaboration with Mark Kuzyk and Hailin Wang and has been published in Physical Review Applied as Ref. [46].

Chapter IX is the outlook for future work with our ultracoherent diamond spin-mechanical resonators platform. We discuss future phononic cavity-QED experiments with SiV^- in diamond and phononic networks with coupled Lamb wave resonators.

The Appendix presents experimental studies of the quenching and broadening effects of telecom lasers on SiV^- centers. Theoretical calculations on strain coupling are included, and discussions on the broadening of mechanical-Q factor under

sideband coupling with color centers in diamond is presented. This part of content was done in collaboration with Hailin Wang and will be published in future.

CHAPTER II

COLOR CENTERS IN DIAMOND

2.1 Introduction

Defects in solid materials are often regarded as imperfections. Formed by impurity atoms, vacancies, or a combination of both, these defect centers in the crystal lattice give rise to unique colors and properties to a wide range of solids. Diamond as a wide band-gap semiconductor is a host to many color centers. Nitrogen-vacancy centers (NV^-) formed by a substitute nitrogen atom and a nearby vacancy host extraordinary properties for quantum applications at even room temperature [3]. Experimental techniques for the creation and quantum control of NV^- centers have been extensively studied, including the preparation, manipulation and readout of quantum states [4].

While NV^- centers remain to this date the most prominent and studied defect center in diamond, other types of defects offer distinct properties, such as silicon-vacancy in diamond (SiV^-). Formed by an interstitial Si atom with two vacancies, SiV^- features a narrow and intense zero-phonon line [47]. It also possesses inversion symmetry which leads to insensitivity to electric field fluctuations. The progress of building quantum computers based on NV^- centers and SiV^- centers however has remained elusive, where one of the obstacles being the difficulties of coupling the color centers together. In this chapter we introduce the important properties of NV^- and SiV^-, then we discuss the strain coupling of color centers to phonons. At the end we talk about the prospects for experimentally reaching the full quantum regime of spin-mechanics with color centers in diamond.

2.2 Nitrogen-Vacancy Center in Diamond

2.2.1 Overview

A nitrogen-vacancy center in diamond is formed by one substitutional nitrogen atom with one lattice vacancy nearby, as is shown in Fig. 2.1 (a). A thorough understanding of its energy level structures selection rules and polarization benefits from a group theory approach [3]. For NV^- centers in diamond, the lattice vacancy creates four sp^3 dangling bonds $\{\sigma_1, \sigma_2, \sigma_3, \sigma_N\}$ from unpaired electrons, where three of them center on the three carbon atoms and the fourth one is on the nitrogen atom. The geometry therefore belongs to the C_{3v} symmetry group and the group elements include identity, rotations by $\pm 120°$ around the NV^- axis and three vertical reflection planes which each contain one nitrogen and one carbon atom as is shown in Fig.2.1 (b), denoted as $\{E, C_{3+}, C_{3-}, \sigma_d, \sigma_e, \sigma_f\}$ [3].

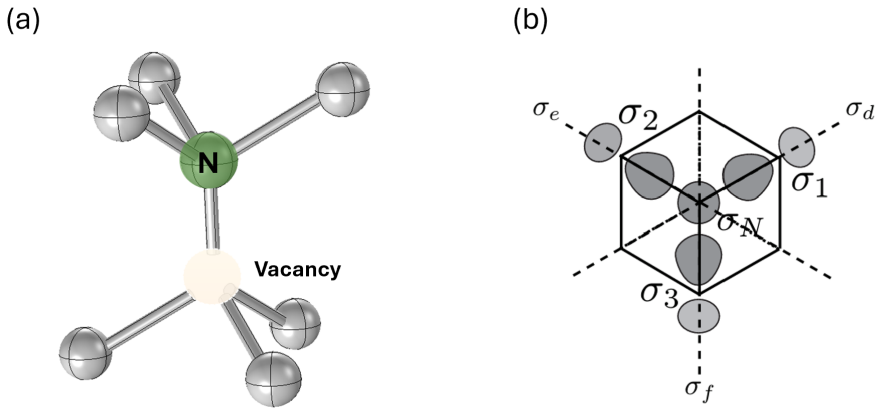

FIGURE 2.1. (a) Lattice structure of a nitrogen-vacancy center(NV^-) in diamond, containing one substitutional nitrogen atom and one nearby vacancy. (b) Symmetry properties of NV^- center in diamond, with the symmetry axis or the NV axis pointing out of the plane of the page. The dashed lines represent the three vertical reflection planes of the C_{3v} group. Taken from Fig. A.1 in Ref. [3].

The characters and irreducible representations for C_{3v} group have been well studied and established [48]. Electron orbitals of NV^- centers $\{\phi_r\}$ are formed by combinations of dangling bonds and can be calculated by projecting the bonds onto each irreducible representation of the C_{3v} group:

$$\phi_r = P^{(r)}\sigma_i = \frac{l_r}{h}\sum_e \chi_e^r R_e \sigma_i \tag{2.1}$$

where $P^{(r)}$ is the projective operator, χ_e^r is the character of operation Re, l_r is the dimension of the $IR^{(r)}$ and h is the order of the group. This leads to the electron orbital basis of $\{a_1(1) = \alpha a_c + \beta a_N, a_1(2) = \alpha a_N + \beta a_c, e_x = (2\sigma_1 - \sigma_2 - \sigma_3)/\sqrt{6}, e_y = (\sigma_2 - \sigma_3)/\sqrt{2}\}$ where $a_c = (\sigma_1 + \sigma_2 + \sigma_3)/3$ and $a_N = \sigma_N$. $a_1(1)$ and $a_1(2)$ transform as IR A_1 and e_x, e_y transform as IR E as two degenerate states.

NV^- centers possess six electrons in total – one each from the three carbon atoms, two from the nitrogen atom and one more electron from the environment. Therefore, it is straightforward that the ground state (e^2) should consist of two electrons occupying each of $\{a_1(1), a_1(2)\}$ and two electrons paring up in $\{e_x, e_y\}$ orbitals. The excited state (ae) will then be one electron from $a_1(2)$ being promoted to $\{e_x, e_y\}$ orbitals, and 2nd excited state (a^2) being the remaining electron promoted from $a_1(2)$ to $\{e_x, e_y\}$ orbitals. The complete Hamiltonian of NV^- centers need to consider the effects of crystal field potential, spin–spin, spin–orbit and Coulomb interactions, as well as expansions, contractions and stress [3].

The NV^- center ground state is a triplet $^3A_2$ state, according to the first Hund's rule [49]. Spin–orbit interaction lifts the degeneracy of states with non-zero angular momentum, for example between the excited states $A_{1,2}$ and $E_{x,y}$ and between $E_{x,y}$ and $E_{1,2}$. The weak spin-orbit interaction of NV^- center in diamond also contributes

to its long spin coherence times and intersystem crossing between singlet and triplet states. On the other hand, states with different spin projections and $A_{1,2}$ states are split by spin-spin interactions. This interaction also leads to mixing of excited states such as $E_{1,2}$ and $E_{x,y}$, resulting from the lack of inversion symmetry of NV^- center. Lastly, strain happens when there are atom displacements in the crystal lattice which can happen through applied force, electric field or temperature change [50]. It breaks the xy-symmetry and causes splitting and mixing of states. For NV^- centers, the excited states are much more sensitive to strain and feature a spin-phonon coupling rate several orders of magnitude stronger than ground states coupling [51]. The strain distribution also varies at different points of the crystal, and therefore each NV^- center feature unique energy splitting and mixings. Fig. 2.2 shows the energy level strucure, effects of spin-orbit and spin-spin coupling on energy level splitting and mixing, along with the emission spectrum of NV^- centers [4].

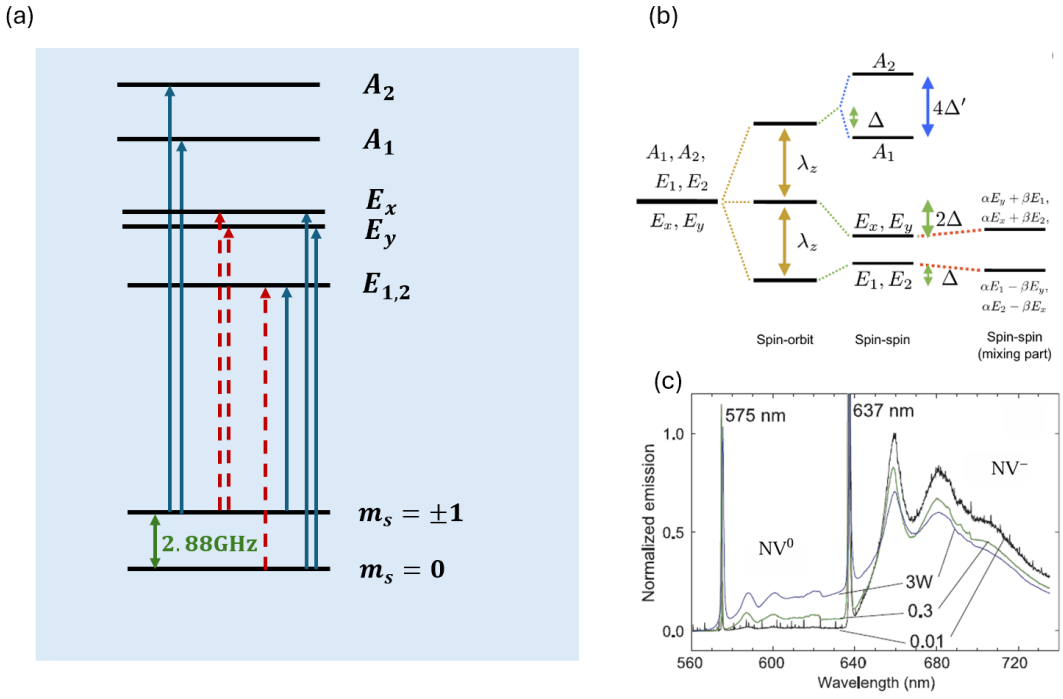

FIGURE 2.2. (a) Energy level structure of the negative nitrogen-vacancy center. Transitions from the ground states to excited states are labeled with dashed and solid lines where dashed lines indicate dipole transitions enabled by strain mixing. (b) Effects of spin-orbit coupling, spin-spin interactions on the energy level structure of NV^-. Taken from Fig. 2 from Ref. [3]. (c) Emission spectrum of NV^- and NV^0. Taken from Fig. 1 from Ref. [4].

2.2.2 Quantum Control of NV^- Centers

2.2.2.1 Confocal Microscopy. We introduce confocal microscopy as a powerful tool for creating high resolution three-dimensional imaging for color centers. The advantage of confocal imaging compared to conventional imaging comes from the ability of rejecting out-of-focus light from both z and x,y directions [52]. This is crucial in quantum optics experiments where accurate addressing and manipulation of individual color center or emitter is required.

Major components of a confocal microscope include a high numerical aperture (NA) objective, a pinhole and a detector. Fig. 2.3 shows an example of a simplified

confocal setup [5], where laser gets reflected by a dichroic mirror then passes through an objective and focuses onto the sample. For a fluorescent specimen such as a bulk diamond sample, fluorescence gets collected by the high NA objective and follow the same path back until reaching the dichroic mirror, where it passes through and gets to the detector and pinhole plane. The pinhole serves as the essence of the confocal microscope and rejects emission contributed by out-of-focus points in both lateral and axial directions.

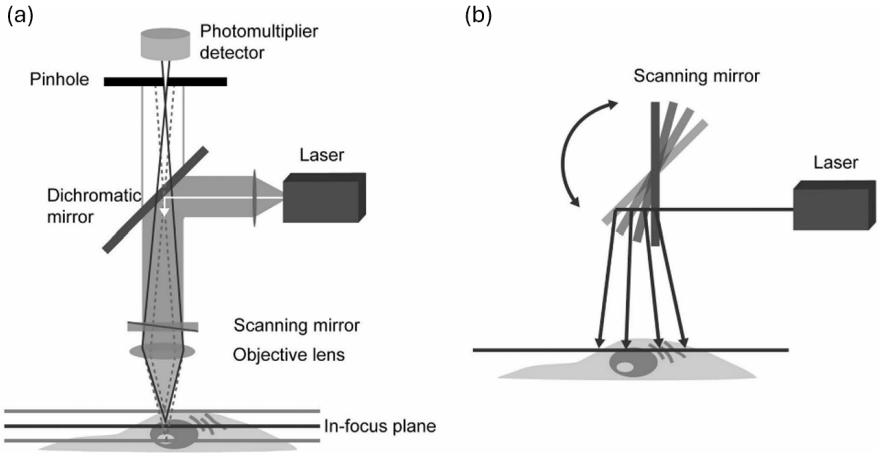

FIGURE 2.3. (a) A simplified confocal setup. Laser light gets reflected by the dichroic mirror then focus onto the sample with the objective lens, after which fluorescence is collected and goes through the dichroic mirror to the photodetector. (b) A scanning mirror controlling the focal position of the laser spot, imaging and collecting fluorescence from different points on the sample. Taken from Fig. 1 from Ref. [5].

Resolution and contrast gauges the performance of all optical microscopes. Resolution is defined by the minimum separation between two distinguishable points, or in other words the ability to see fine details. Rayleigh criterion states that two points are resolved when the first minimum of one Airy disk is aligned with the

central maximum of the second Airy disk. Lateral resolution is therefore [52]

$$r_{lateral} = 1.22\lambda/(2 \cdot NA) = 0.6\lambda/NA \tag{2.2}$$

where NA is the numerical aperture of the objective and λ is the optical wavelength. For confocal fluorescence detections however, the intensity point spread function (psf) becomes the product of the illumination intensity and detection intensity point spread functions, leading to a reduced point spread function and the resulting formula becomes

$$r_{lateral} = 0.4\lambda/NA \tag{2.3}$$

Similarly for axial direction, contrast between two points in the specimen on the axis happens when the distance between them exceeds the central maximum and the first minimum of the axial point spread function component. For confocal configurations, one common equation for the axial resolution is

$$r_{axial} = 1.4\lambda \cdot \eta/NA^2 \tag{2.4}$$

where η is the refraction index. Compared to conventional microscopy, confocal microscopy stands out especially for its optical sectioning capability in thick specimens and features a dramatic improvement in the axial resolution, since the integrated intensity point spread function has a maximum in the focal plane.

Fig. 2.4 shows the experimental setup for our confocal microscopy. The sample containing NV^- centers is mounted vertically on a L-shape copper bracket with silver paste and cooled down to a sample temperature of 4K with Montana Cryostation

s50. Green laser at 532nm (Laserglow Technologies) is used for initialization of NV^- centers and a 637nm tunable laser (New Focus 6701) is for resonant excitation of NV^- centers. The lasers are combined at a dichroic mirror (Semrock Di02-R594) and get reflected at another dichroic mirror (Semrock Di02-R635) which distinguishes the excitation and collection path. The lasers then go through a Galvanometer system (GVS-210) which sweeps the excitation beam over the diamond sample point by point. A high numerical aperture (NA=0.8) objective (NiKon L Plan 100x) is used for focusing onto the sample and collecting fluorescence from the color centers.

The collected fluorescence goes through the objective, Galvanometer system, then transmitted through the dichroic mirror and gets collected by a multi-mode fiber (Thorlab M64L02) with a core diameter of 10μm. The fiber serves as a pinhole and rejects light not coming from focal points. Due to the trade-off between collection efficiency and imaging resolution, sometimes a higher core-diameter (up to 50 μm) multimode fiber is used to get higher photon counts and better signal-to-noise ratio.

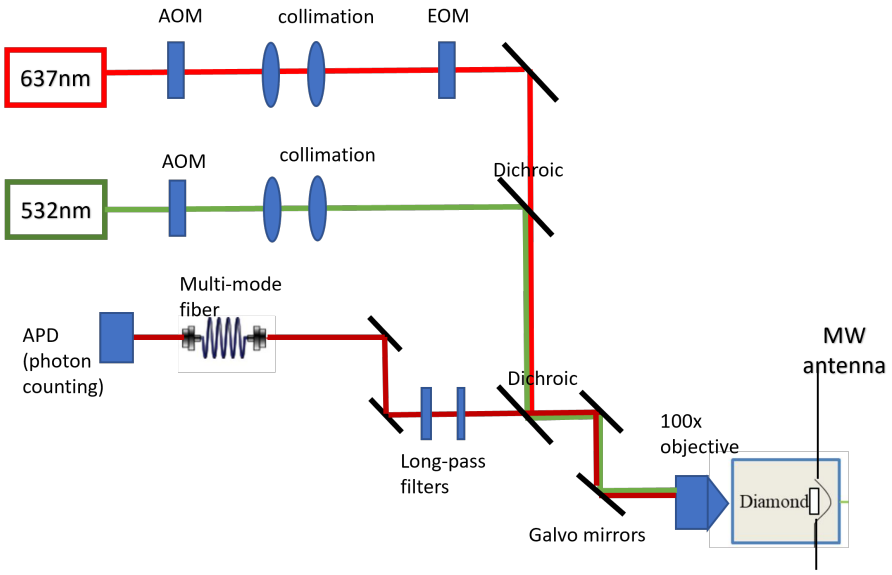

FIGURE 2.4. A detailed confocal optical microscope for experiments on color centers in diamond. A green laser is used for state initialization and a red laser is for resonant excitation. Diamond sample is mounted in a Montana Cryostation where temperature gets cooled down to below 10K.

2.2.2.2 Ground States Control of NV^- Centers. Ground states control of NV^- centers can happen in a room-temperature setup, due to their long spin coherence times without the need of cryogenic operations. In earlier section we discussed the ground ^3A and excited ^3E states triplets of NV^- centers. Two other intermediate states ^1A and ^1E are singlets and play a crucial part in the spin initialization [4]. A green off-resonant laser light at ~532nm is able to excite the population from ^3A to the phonon vibronic bands then relax into ^3E in a spin-preserving way. Population starting at ^3A with $m_s = 0$ will end up at ^3E with $m_s = 0$ and decay back to $m_s = 0$ in ^3A while emitting a red photon. Population starting at ^3A with $m_s = 1$ will be driven to the $m_s = 1$ state in ^3E however then has a preferrable path of decaying through a metastable state in a non-radiative way. This path is also non-spin conservative that the population falls to $m_s = 0$ state.

After many cycles of green illumination, nearly all population initially in $m_s = 1$ will be pumped into $m_s = 0$. This also shows the difference in fluorescence intensity for NV^- center population starting at $m_s = 0$ and $m_s = 1$.

Based on this, we're able to pinpoint the locations of NV^- centers by doing a large scan with green laser and collect the fluorescence from the phonon sideband, creating a photoluminescence (PL) map. As is shown in Fig. 2.5(a), multiple single bright spots with high photon counts indicate locations of single NV^- centers. The collection is then optimized at a single point through adjustment of x,y,z and fiber collimation. The red circle indicates a bright optimized NV^- that we will be using in the following quantum control experiments.

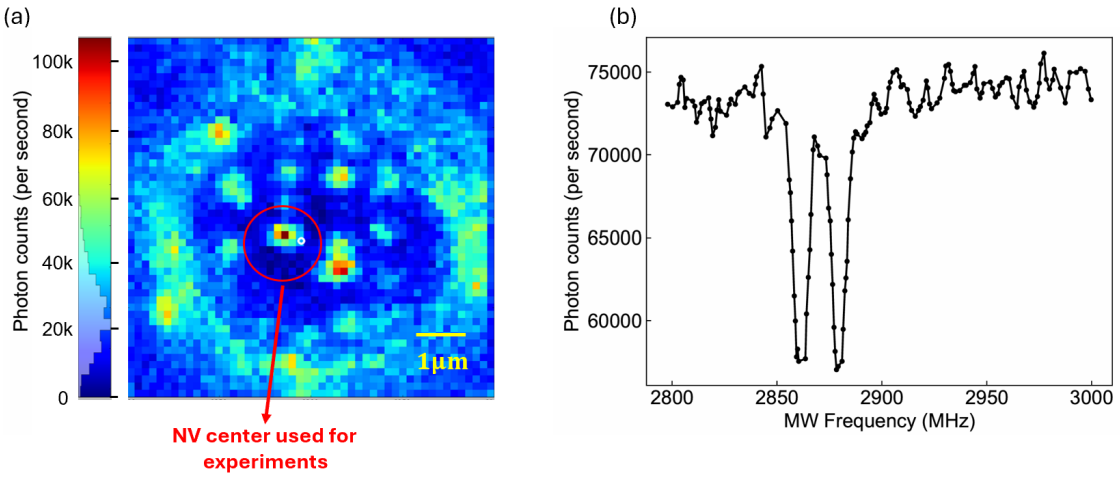

FIGURE 2.5. (a) A photoluminescence (PL) map of diamond NV^- centers showing locations of single NV^- in a solid immersion lens (SIL). (b) Optically detected magnetic resonance (ODMR) for the single NV^- indicated in (a) under an external magnetic field.

Without any external magnetic field, the separation between the NV^- $|m_s = 0\rangle$ and $|m_s = 1\rangle$ states is around 2.88GHz due to magnetic interactions. By applying an external magnetic field along the NV^- axis, $|m_s = -1\rangle$ and $|m_s = 1\rangle$ states split due to Zeeman effect. The separation in energy can be probed by applying a continuous-

wave microwave field around 2.88GHz that drives the population cycling between different spin states. While scanning the frequency of the microwave field, two dips in the fluorescence intensity will show up, due to the non-radiative decay path from $|m_s = 1\rangle$ states. This process is called optically detected magnetic resonance (ODMR) and Fig. 2.5 (b) shows an example of the ODMR spectrum.

A Bloch sphere is an effective way of representing a two-level system where any pure state can be indicated as a point on the sphere [53]. Rabi oscillations is a process where an oscillating driving field interacts with a two-level system and drives the population flopping between the two states. This can be visualized as rotations on the Bloch sphere with stronger driving field leading to higher Rabi frequencies, which indicates atom-field interaction strength and is defined as:

$$\Omega = \sqrt{|\Omega_0|^2 + \delta^2}, \Omega_0 = \mu_{12} E/\hbar \tag{2.5}$$

Where E is the amplitude of driving field, μ_{12} is the dipole moment element and δ is the field detuning. Fig. 2.6 shows the pulse sequence and time evolution for Rabi oscillation at a frequency of about 13MHz.

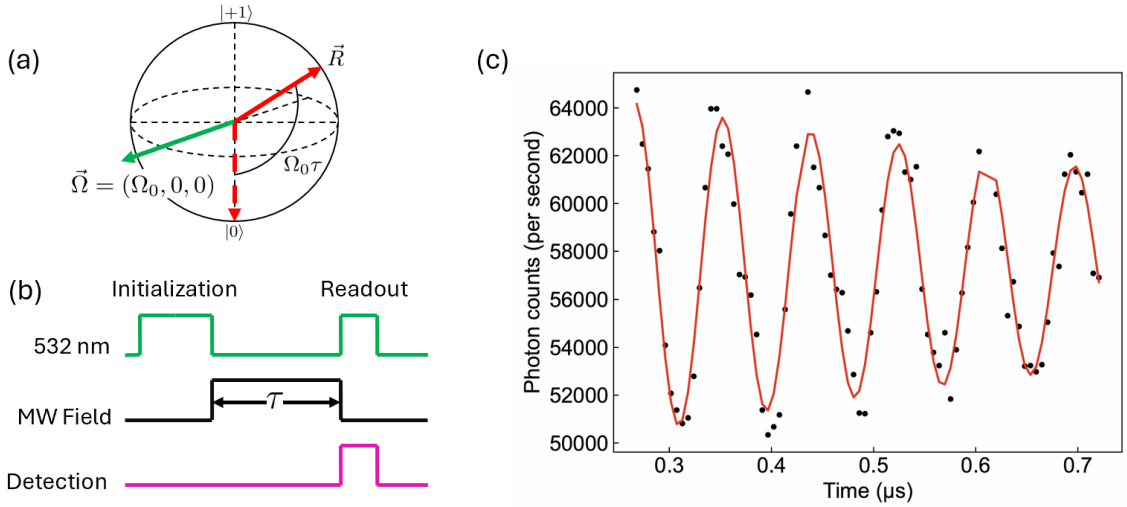

FIGURE 2.6. (a) A Bloch sphere representation of a two-level system. (b) Pulse sequence for Rabi oscillations with green laser, microwave field control and photon detection. (c) Rabi oscillations of a NV^- center with a fitted frequency of 13MHz.

When lowering the microwave field power, hyperfine structures of NV^- spin states due to the magnetic field from the nitrogen nucleus show up corresponding to different nuclear spin orientations. For the common isotope of ^{14}N which has a spin of 1, each of the $|m_s = 1\rangle$ levels split into $|m_N = 0, 1, -1\rangle$ with a separation of 2.2MHz under low driving power, as is shown in Fig. 2.7 (a).

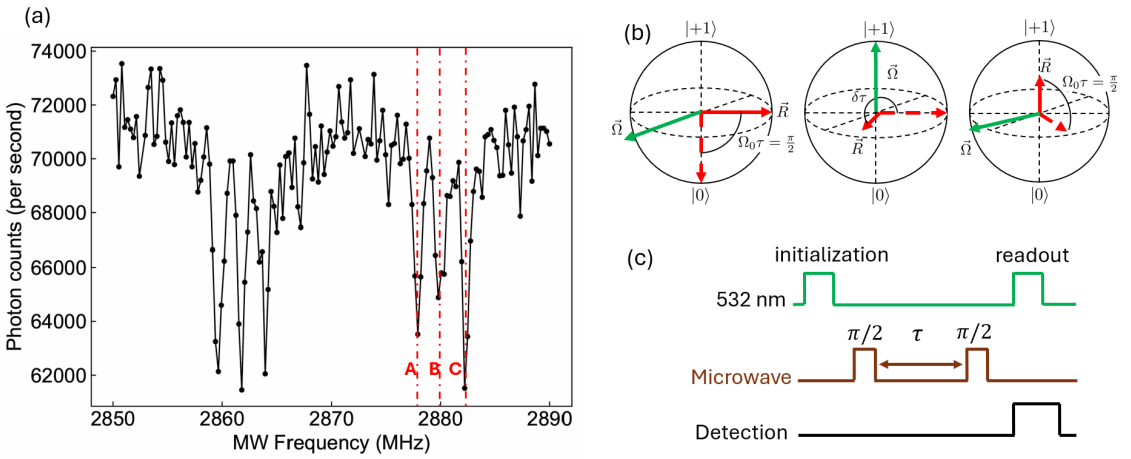

FIGURE 2.7. (a) Hyperfine structures of NV^- spin states under low MW power. The three dashed vertical lines are aligned to the splittings with a frequency separation of 2.2MHz. (b) Bloch sphere representation for Ramsey interferometry. (b) Pulse sequence for Ramsey interferometry.

Ramsey interferometry on the other hand can be used to measure the frequency of atomic transitions from its precession frequency and the decay of polarization. Fig. 2.7 (b) (c) shows the Bloch sphere representation and pulse sequence for the interferometry where a $\pi/2$ pulse is applied to a two-level system followed by a delay of τ and then another $\pi/2$ pulse. The frequency of the driving pulses features a detuning of δ and the upper state population is measured as a function of τ. By rotating on the Bloch sphere, the resulting fringes precess at the frequency of δ. Fig. 2.8 shows the Ramsey fringes when the driving field is set at position A and B in Fig. 2.7(a), showing a beating frequency of 2.2MHz plus 4.4MHz at position A and 2.2MHz at B. By fitting the curve with a Gaussian envelope $e^{-(t/T_2^*)^2}$, we can extract T_2^* which characterizes the qubit dephasing information. For the data shown in Fig. 2.8 (b), we obtain a T_2^* of about 2μs.

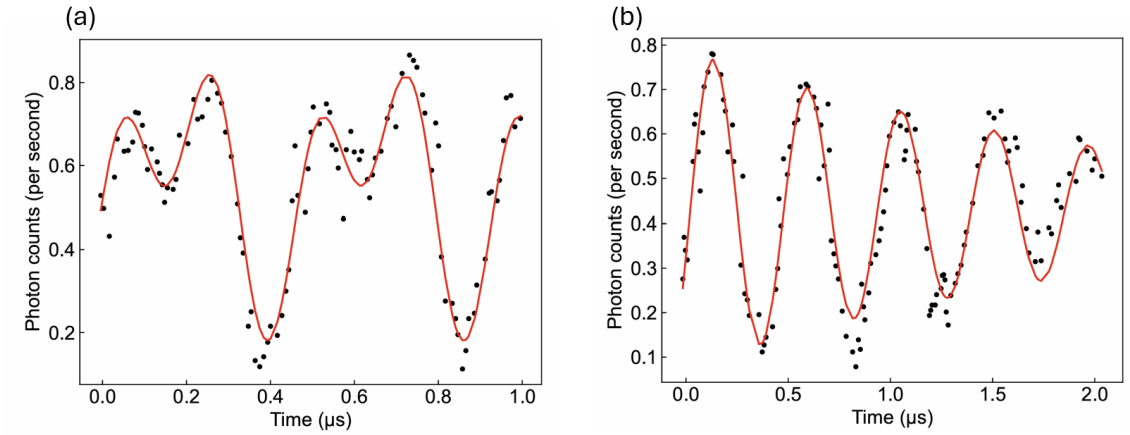

FIGURE 2.8. Ramsey interferometry of a single NV^- center. (a) Ramsey fringes when the MW frequency is set at the position of line A in Fig. 2.7 (a) which features frequency detunings of 2.2MHz and 4.4MHz relative to the positions of line B and line C. (c) Ramsey fringes when the MW frequency is set at the position of line B in Fig. 2.7 (a) which features frequency detunings of 2.2MHz relative to the positions of line A and line C.

2.2.2.3 Excited States Control of NV^- Centers . Excited states manipulation of NV^- centers involves resonant excitation with laser frequencies near the zero-phonon line (ZPL) of 637nm. This needs to be carried out at cryogenic temperatures since NV^- optical transitions at room temperatures are significantly broadened by phonons. We scan the frequency of a tunable laser diode across the NV^- resonances while collecting phonon sideband fluorescence to find the linewidth of the optical transitions. Tuning of laser frequencies can be done through piezo voltage control through an external analog voltage source such as a lock-in amplifier or an Arbitrary Function Generator (AFG). Fig. 2.9 shows the excitation spectrum of a single NV^- center where the two distinct peaks correspond to $|0\rangle$ to $|E_x\rangle$ and $|0\rangle$ to $|Ey\rangle$ transitions. The laser pulse sequence indicates where a green laser is turned on for 3μs for initialization, followed by a 10μs of 637nm red laser and a collection window. The NV^- center shown here features an optical linewidth of 200MHz.

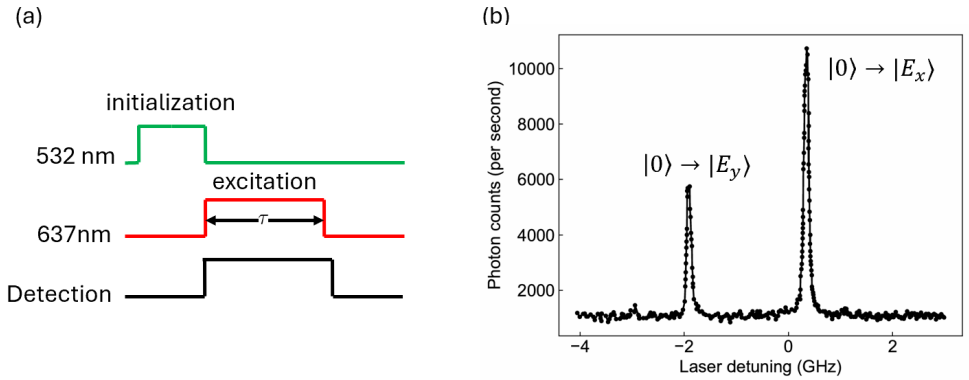

FIGURE 2.9. Photoluminescence excitation (PLE) of a single NV^- center. (a) Pulse sequence for the PLE experiment. (b) PLE spectrum of a single NV^- center with two distinct peaks showing the NV^- excited state transitions.

2.2.2.4 Coherent Population Trapping of NV^- Centers. Instead of microwave control, an all-optical approach for detecting NV^- ground state spin resonances can be achieved with Coherent Population Trapping (CPT). In a Λ-type configuration, when two optical fields simultaneously drive the two transitions from the lower states to the common upper state, destructive interference between the two pathways leading to a "dark state" which is a coherent superposition of the two lower levels [53]. For NV^- centers, the Λ-type system can be formed with the ground states $|0\rangle$ and one of the $|1\rangle$ as two lower levels and excited state $|E_y\rangle$ as the upper level. The originally forbidden transition $|+1\rangle$ to $|E_y\rangle$ due to selection rule is permitted due to state mixing caused by strain in the diamond lattice. The Hamiltonian can be written as

$$H = \frac{\hbar}{2}(\Omega_-|0\rangle\langle e| + \Omega_+|1\rangle\langle e|) \tag{2.6}$$

which features a dark eigenstate

$$|D\rangle = \frac{1}{\sqrt{\Omega_+^2 + \Omega_-^2}}(\Omega_-|1\rangle - \Omega_+|0\rangle) \tag{2.7}$$

In the experiment, we use a phase electro-optical modulator (EOM Jenoptic PM635) for generating optical sidebands for driving Ω_- and Ω_+ transitions. Due to the fact that $|1\rangle$ to $|E_y\rangle$ transition is much weaker than $|0\rangle$ to $|E_y\rangle$, the optical carrier is set at the frequency of $|1\rangle$ to $|E_y\rangle$ while the RF input of the EOM is scanned across the magnetic resonance $|0\rangle$ to $|1\rangle$, creating a dip in the fluorescence when the system is in Raman resonance, which means δ=0 in Fig. 2.10 (a). Fig. 2.10 shows the diagram of a Λ-type system and a typical CPT scan of a single NV^- center, indicting a spin resonance at around 2880MHz.

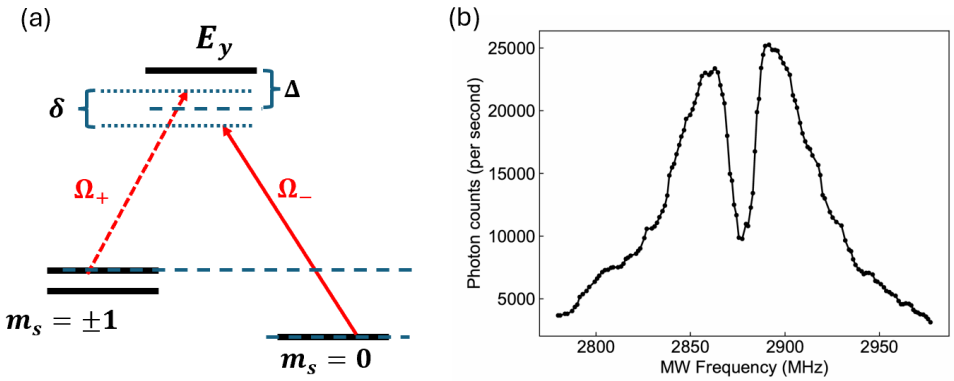

FIGURE 2.10. Coherent population trapping (CPT) of a single NV^- center. (a) Energy level diagram used for the CPT process. Raman resonance forms when δ=0. (b) A scanned CPT spectrum of a single NV^- center with the dark state formed at a microwave frequency of 2.88GHz.

2.2.2.5 Raman Transitions of NV^- Centers. Based on the Λ-system for CPT, we can further implement a two-photon Raman transition driving the population between the spin states of an NV^- center. Compared to MW control, an

all-optical approach mitigates the difficulties of incorporating electronic feedthroughs and reduces heating. To drive rabi oscillations between $|m_s = 0\rangle$ and $|m_s = 1\rangle$ ground state, we use $|E_y\rangle$ as the upper level and use $|m_s = 1\rangle$ to $|A_2\rangle$ as a readout path. An alternate approach is to use $|0\rangle$ to $|E_y\rangle$ or $|E_x\rangle$ as readout to detect the population affected by the two-photon process in $|0\rangle$. The Hamiltonian of the Λ-system can be written as [40]:

$$H = \begin{bmatrix} \Delta - \delta/2 & 0 & \Omega_-/2 \\ 0 & \Delta + \delta/2 & \Omega_+/2 \\ \Omega_-/2 & \Omega_+/2 & 0 \end{bmatrix} \tag{2.8}$$

Where δ is the detuning from Raman resonance, Δ is the average dipole detuning, and Ω_- and Ω_+ are the Rabi frequencies for the two driving fields. When δ=0 and $|\Delta| \gg \Omega_+, \Omega_-$, the effective Hamiltonian can be written as:

$$H_{eff} = -\frac{1}{4\Delta} \begin{bmatrix} \Omega_-^2 & \Omega_+\Omega_- \\ \Omega_+\Omega_- & \Omega_+^2 \end{bmatrix} \tag{2.9}$$

This is equivalent to a two-level system with a Rabi frequency of

$$\Omega_R = \Omega_+\Omega_-/2|\Delta| \tag{2.10}$$

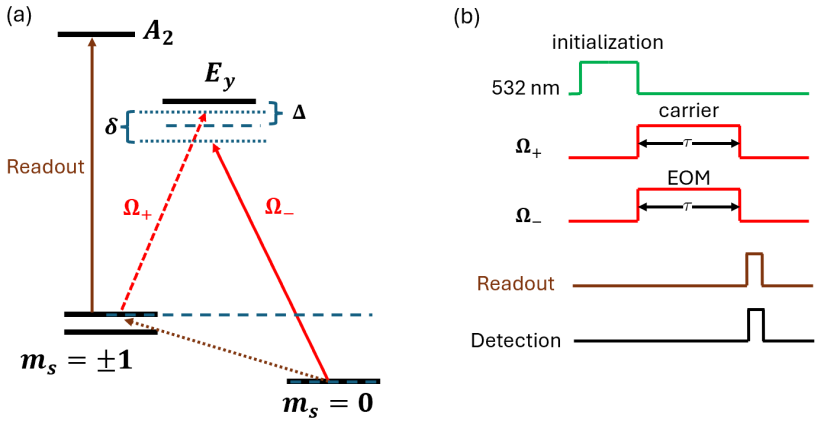

FIGURE 2.11. (a) A Λ-type system for optically driving spin transitions through a Raman process. Raman resonance forms when δ=0. Population can be readout through the A_2 state. (b) Pulse sequence for driving the population transfer between two spin states. Two optical driving fields originate from a same laser through the carrier and sidebands from a phase EOM.

Fig. 2.11 (a) shows the energy levels used in our two-photon process. We choose a dipole detuning of Δ=500MHz and scan the Raman resonance across the spin states separation. The pulse sequence is shown in (b) where a green laser initializes the NV^- center, then the two-photon pulse transfers the population from $|m_s = 0\rangle$ to $|m_s = 1\rangle$ and the state is read out by a second red laser (Toptica DL Pro) with a pulse duration of 100ns driving the transition from $|m_s = 1\rangle$ to $|A_2\rangle$. A shorter readout pulse is necessary to avoid fast optical pumping. Fig. 2.12 (a) shows the result of the scan, with a Raman resonance at 2900MHz under an external magnetic field. Next we vary the pulse duration τ of the two-photon laser and therefore see Rabi oscillations between $|m_s = 0\rangle$ and $|m_s = 1\rangle$ at a frequency of about 1MHz, as shown in Fig. 2.12 (b).

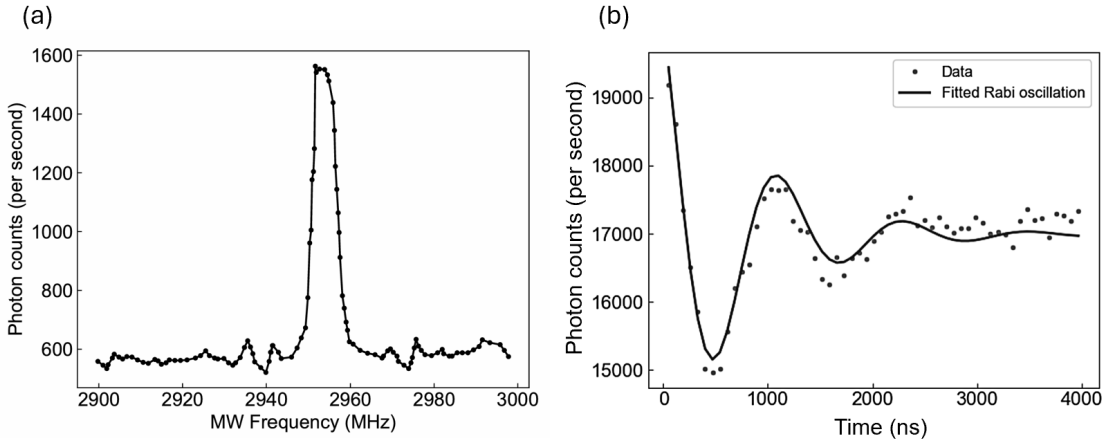

FIGURE 2.12. (a) Spin resonance measured through a Raman process with the energy level structures shown in Fig. 2.11 (a) for a NV^- center. (b) Optically-driven rabi oscillations between the two spin states $|m_s = 0\rangle$ and $m_s = |1\rangle$ through the Raman process.

2.3 Silicon-Vacancy Center in Diamond

2.3.1 Overview

Compared to NV^- centers in diamond, a silicon-vacancy center (SiV^-) is formed by one interstitial silicon atom between two lattice vacancies nearby, as is shown in Fig. 2.13(a). The fundamental difference in lattice structure determines that SiV^- belongs to a different symmetry group D_{3d}. From the defect geometry, twelve symmetry operations belonging to six symmetry classes can be identified for the SiV^-: $\{E, 2C_3, 3C_2, i, 2S_6, 3\sigma\}$. Following similar procedures described for NV, we can find the irreducible representations (IR) for the SiV^- dangling bond representation, obtaining four representations E_g, E_u and A_{1g}, A_{2u} which leads to four possible SiV^- electronic states with two being non-degenerate and two being two-fold degenerate. Fig. 2.13 (b) (c) shows an example of energy levels of a SiV^- center in diamond [6].

The SiV^- center is a spin S = 1/2 system so both the ground and excited states are degenerated. This degeneracy is lifted by a combination of the spin-orbit (SO) coupling and the Jahn-Teller (JT) effect and together, they split the four-fold degenerate states into two sets of two-fold degenerate levels, leading to two degenerate ground states and two excited states. Each of these states is again doubly degenerate by spin. All four transitions between the ground and excited states are dipole allowed, as labeled in Fig. 2.13(b) as transitions a, b, c, d.

The inversion symmetry of SiV^- centers becomes especially crucial when it comes to experiments with diamond nanostructures which went through heavy fabrication processing steps. Nanofabrication steps including ion implantation, reactive-ion etching have shown to induce surface roughness and contamination into the diamond lattice [54, 55, 56], which in the case of NV^- centers, cause severe charge fluctuations and broadening of optical linewidth due to the non-zero electric dipoles of NV^- centers [54].

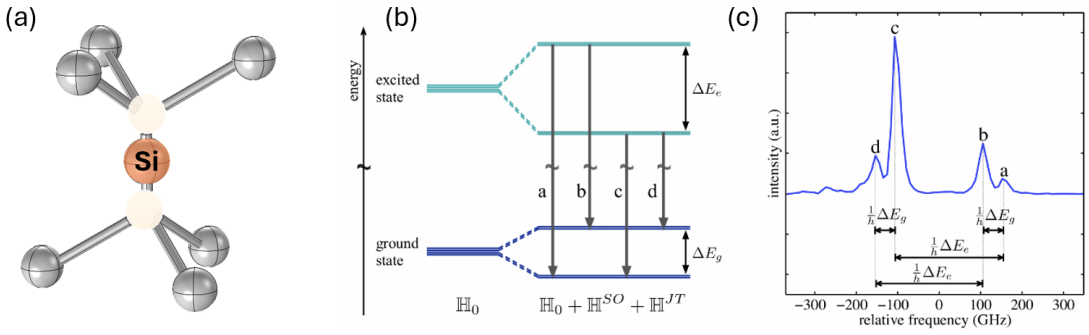

FIGURE 2.13. Silicon-vacancy centers in diamond (SiV^-). (a) Lattice structure of a single SiV^- center where a interstitial silicon atom is placed between two nearby vacancies. (b) Energy level diagram of a SiV^- under spin-orbit coupling and Jahn-Teller effect. (c) Four dipole-allowed transitions from the energy level structure shown in (b), labeled as a, b, c, d. Taken from Fig. 2.16 from Ref. [6].

2.3.2 Quantum Control of SiV^- Centers

2.3.2.1 Experimental Setup. A confocal microscope is necessary for collecting fluorescence coming from SiV^- centers. Differently from NV^- centers, over 70% of photoluminescence from SiV^- is concentrated in the zero-phonon line around 737nm with a much smaller portion remaining in the phonon sideband [29], leading to lower photon collection in the experiment. Compared to an NV^- confocal setup, a dichroic mirror (Semrock FF757-Di01) is for collecting sidebands around 737nm and a Tunable long-pass filter (TLP01-790) is for filtering out the ZPL. Besides these, a band-pass filter at 740±10nm is for spectral cleaning of the Toptica 737nm red laser.

For SiV^- centers applications, one severe limitation is spin-dephasing induced by phonon mediated transitions between the orbital branches [57]. At a temperature of above 1K, the rich phonon environment at around 50GHz frequencies matches the splitting of the SiV^- orbital frequency, causing severe decoherence of the spin states. Therefore, applications making use of the coherence of SiV^- spin states either require the system being cooled down to mK temperatures or require strain engineering processes [58].

2.3.2.2 Excited States Control of SiV^- Centers. Our characterization of SiV^- centers were carried out in a diamond membrane sample with fabricated nanomechanical structures. Fig. 2.14 (a) shows a photoluminescence map (PL) of a diamond Lamb Wave Resonator surrounded by phononic crystals. For the single SiV^- indicated in the picture, a photoluminescence excitation (PLE) spectrum is shown in Fig. 2.14 (b). This corresponds to transition C at about 737.08nm for this SiV^- with an optical linewidth of 300MHz.

It is worth noting that the optical linewidth and charge stability of SiV^-s are also affected by surface roughness possibly brought by nanofabrication steps, although not as severely affected as the case of NV^- centers. For diamond thickness of below 1μm, blue laser has proven to be very effective at stabilizing charges and reducing spectral diffusions [59], which was also believed to work on other group IV defect centers. The mechanism is related to the conversion of SiV^{2-} to SiV^- by capturing of holes from the nearby environment [60]. For our experiments, the specific SiV^- being worked on has been illuminated with blue laser (450nm CivilLaser) for prolonged hours. After that, green initialization is no longer required and the optical linewidth in thin diamond membranes could be as low as 150MHz.

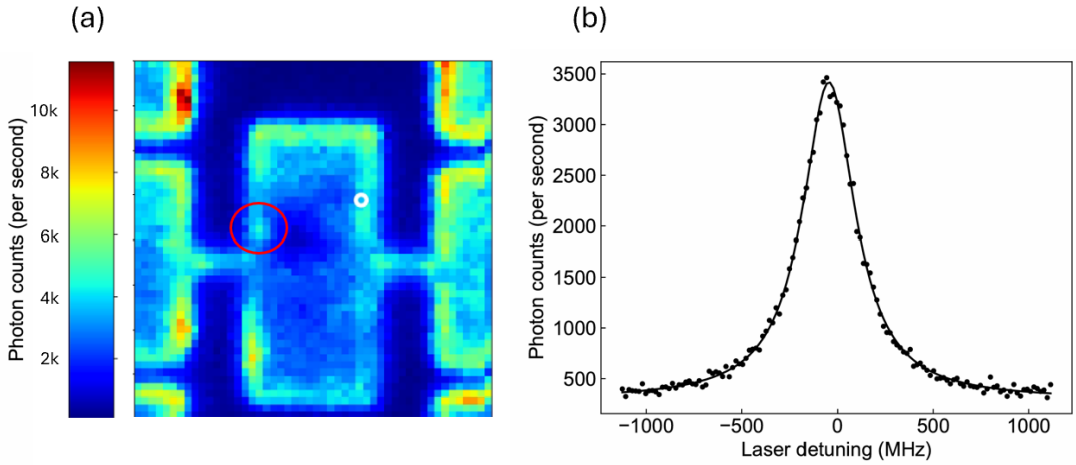

FIGURE 2.14. (a) Photoluminescence (PL) of a diamond Lamb wave resonator containing implanted SiV^- centers. (b) PLE spectrum of the single SiV^- center indicated in (a) with a distinct peak showing transition c as in Fig. 2.13.

2.4 Strain Coupling of Colors Centers in Diamond

Here we briefly explore the strain coupling of color centers in diamond as a basis for the discussions in following chapters. Displacements of atoms in the diamond lattice cause changes in the effective potential the color center experiences, therefore

lattice vibrations at a certain frequency periodically modulate the color center optical transition frequency, leading to sidebands in the optical transition [3], as is shown in Fig. 2.15(a). Blue and red sidebands correspond to the optical driving frequency at one or multiple phonon frequencies above or below the optical resonance, as is shown in Fig. 2.15(b). Beyond phonon-assisted sideband transitions, spin-phonon coupling could also happen through direct transitions, for example the coupling of a mechanical wave to the spin states of a color center, as is shown in (c).

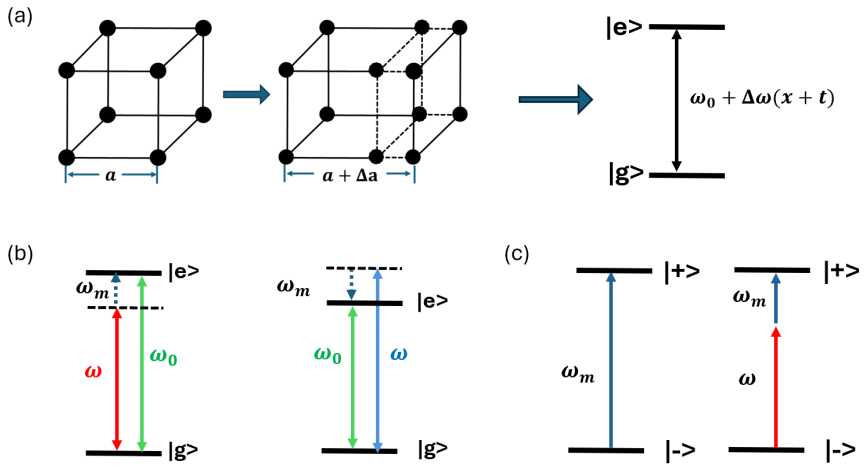

FIGURE 2.15. Simplified spin-phonon coupling diagrams. (a) Lattice vibrations modulate the energy level of a two-level system and induce phonon sidebands as shown in (b). (c) Diagram of spin-phonon coupling through either direct transition or phonon-assisted sideband transitions.

For a two-level system coupled directly to a mechanical resonator, the spin-phonon coupling Hamiltonian can be written as:

$$V = \hbar g(\hat{b} + \hat{b^+})(|e\rangle\langle g| + |g\rangle\langle e|) \tag{2.11}$$

where $|e\rangle$ and $|g\rangle$ represents the two-level system and g is the single-phonon coupling rate. As discussed earlier in Eq.1.2, g is related to the deformation potential

D which describes how much of energy level changes for a given strain. Under rotating wave approximation, the system reduces to the Jaynes-Cummings model and resembles a cavity-QED system. We defined the dimensionless parameter C in Eq.1.1 as cooperativity for characterizing the spin-phonon coupling strength. When cooperativity is larger than 1, meaning $2g > \sqrt{\gamma_s \gamma_m}$ where γ_s and γ_m are the decay rates of the two-level system and the mechanical mode, we enter the full quantum regime where effects of single phonons become important.

In the case of NV^- centers in diamond, strain can be categorized as axial or transverse strain. Axial strain retains the crystal symmetry and shifts the energy structure while transverse strain causes state mixing. For the experimental realization, strain can therefore induce the transition between either $m_s = \pm 1$ states or between $m_s = 0$ and $m_s = \pm 1$ states, leading to a potential all-acoustic control of NV^- spin states. However for NV^- centers, the robust spin coherence time at room temperature manifests an overall weak strain coupling coefficient,making it difficult to reach high cooperativity with ground states strain coupling. In comparison for SiV^- centers, spin-orbit coupling results in the formation of two doublets for both ground and excited states, and phonon coupling to the orbital components is much stronger than to the spin components. To make use of this, an external off-axis magnetic field can help mix the spin states and enable direct mechanical transition between the spin states, as is shown in Fig. 2.16. The coupling rate now becomes [39]

$$g = k_m x_{zpf} D(\gamma_{SiV} B_\perp / 2\lambda_{SO}) \tag{2.12}$$

which includes the amount of spin mixing described by $\gamma_{SiV} B_\perp / 2\lambda_{SO}$, with γ_{SiV} being the spin gyromagnetic ratio and $B_\perp$ being the transverse field intensity. With a good mixing ratio, g can be orders of magnitude greater than the case of NV^- by

taking advantage of the ground-state orbital strain coupling, making group IV color centers a better candidate for cavity-QED type of experiments.

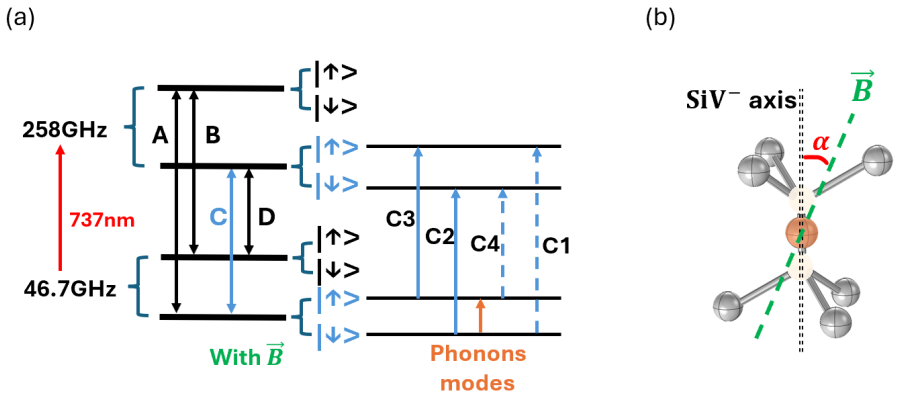

FIGURE 2.16. Coupling of the SiV^- ground state spin levels to a mechanical mode under an off-axis magnetic field B. (a) Energy level structure of a SiV^- center under an external B field as shown in (b).

In summary, a greater g is crucial for reaching the quantum regime of spin-phonon coupling and can be achieved by making use of different spin and orbital properties of SiV^- and NV^- centers. However, increasing g along wouldn't suffice, and a smaller γ_s and γ_m could help increase the cooperativity greatly, according to Eq. 1.1. As discussed earlier, γ_s is limited by the intrinsic linewidth of SiV^- and NV^-, however γ_m can be reduced by orders of magnitude through minimizing mechanical loss. So next we first give a brief review on nanomechanical resonators including their loss mechanism, then we explore ways of reducing loss and obtain ultra-coherent spin-mechanical resonators.

CHAPTER III

NANOMECHANICAL RESONATORS

3.1 Introduction

In this chapter we talk about nanomechanical resonators. Much like a vibrating guitar string, nearly every object can be seen as a harmonic oscillator, with its resonant frequencies determined by its geometry structure and material properties. Nanomechanical resonators have found broad applications in areas such as force and mass sensing [41], timekeeping [61] and quantum information processing [62]. For these applications, three fundamental parameters are emphasized to characterize the utility of mechanical resonators – frequency, mass and quality factor.

Mechanical resonators at different frequencies enable applications across various fields. For quantum spin-mechanics, the development of GHz frequency resonators is crucial for reducing effects of thermal phonons and for matching the mechanical resonance with spin transitions. Through scaling down the dimensions, higher frequency mechanical resonators with reduced mass can be obtained. For ultra-sensitive detection, a smaller effective mass is crucial, where effects of a single atom or molecule could be experimentally characterized. For quantum spin-mechanics studies, the importance of small effective mass is indicated in the zero-point fluctuation (ZPF). A large ZPF is crucial in realizing the quantum regime of spin-mechanics, where effects of single phonons become important.

A quality factor (Q-factor) quantifies the energy exchange of mechanical resonators with its surrounding environment. It is defined as the ratio of the initial energy stored in the resonator to the energy lost in one radian of the cycle

of oscillation, also can be described as the full width at half maximum of the experimentally measured resonance peak. A higher quality factor indicates longer mechanical lifetime and lower damping. Since mechanical waves are not subject to scattering loss into vacuum, the primary loss mechanisms for a mechanical resonator in vacuum are clamping loss and materials loss, also can be categorized as external and internal loss, as is shown in Fig. 3.1.

3.2 Loss Mechanisms of Mechanical Resonators

3.2.1 Material Loss

Intrinsic damping losses in nanomechanical resonators typically arise from material or device defects and imperfections, such as surface losses due to two-level systems (TLS) and thermoelastic dissipation resulting from heat flow across the device induced by resonator deformation [63, 64, 65, 66]. The fundamental intrinsic dissipation mechanisms can be described by thermoelastic, phonon-electron, and phonon-phonon interactions [63].

At low temperatures, phonon damping in nanomechanical systems can be described by a process known as Landau-Rumer damping [67], which occurs when the thermal phonon relaxation rate is much smaller than the acoustic frequency. In this regime, phonon-phonon interactions can be explained by a quantum model of three-phonon scattering which leads to damping and thermalization of acoustic modes. Landau-Rumer damping typically scales with temperature as

$$Q \propto 1/T^4 \tag{3.1}$$

At even lower lattice temperatures (≤ 10 K), Landau-Rumer damping diminishes, and residual damping emerges - primarily due to material defects, such as surface two-level systems (TLS) [65]. These TLS are commonly found in amorphous materials and their electric and acoustic transition dipole moments allow the coupling to both electric fields and strain fields. TLS are also among the most important sources of loss limiting the performance of superconducting quantum circuits [68]. Fluctuating surface TLS also contributes to frequency noise, such as flicker or low-frequency telegraph noise [64].

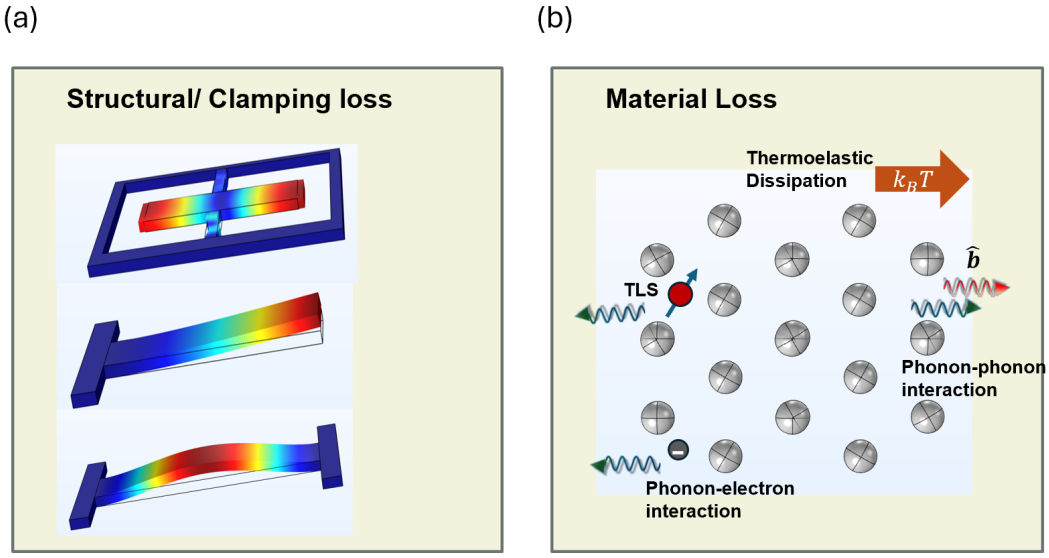

FIGURE 3.1. Loss channels of mechanical modes. (a) Structural loss originating from the clamping of different mechanical structures to their surrounding environment, for example the clamping points of a Lamb wave resonator, a cantilever or a doubly-clamped beam. (b) Material loss channels including thermoelastic dissipation, two-level system defects in the material,phonon-phonon interactions and phonon-electron interactions.

3.2.2 Structural Loss

Structural or clamping loss comes from the anchoring of mechanical resonators to their surrounding environment. Different designs of modes feature different anchoring structures. For example, cantilevers have clamping loss from the attachment to the bulk, double-clamped beams have anchoring loss from both ends, and surface acoustic wave devices have energy dissipation into the attached substrate [69]. The effects of clamping loss especially show up as frequencies of resonators go up where dimensions start to decrease.

In the ideal case, the nanomechanical oscillator is completely isolated from any supporting structure. A levitated mechanical system in ultrahigh vacuum is an example of platforms with minimized mechanical damping rates [70]. This type of system could manipulate a wide range of objects levitated in optical, electrical, and magnetic traps [71]. At a pressure of 7×10^{-11} mbar, a dissipation rate of $2\pi69(22)$nHz was reported [65], corresponding to a quality factor exceeding 10^{10}. For levitated objects, collisions with background-gas molecules are typically the dominant source of dissipation [72]. However, at significantly lower pressure, other factors become of concern, for example dissipation due to radiation damping for a particle confined in an optical tweezer.

3.2.2.1 Phononic Band Gap Engineering. When it is not feasible to levitate devices under test and the sample must be clamped to its surrounding environment, phononic band gap becomes a good way to mitigate acoustic loss by modifying or eliminating the scattering of phonons into the environment. Phononic band gaps are associated with phononic crystals, which are periodically patterned structures with the unit cell designed to feature a band gap around the desired frequency [73].

Extensive studies have been conducted on the choice of patterns and tailoring of parameters to create large band gaps at different frequencies [74]. Fig. 3.2 (a) to (f) shows two examples of designs with "cross" and "snowflake" patterns along with their respective band gap structures. The "cross" design features a large and robust band gap, while the "snowflake" design offers favorable optical properties, making it valuable for designing optomechanical devices that can manipulate both sound and light simultaneously. The mechanical simulations are carried out with COMSOL Multiphysics [75], a finite-element solver.

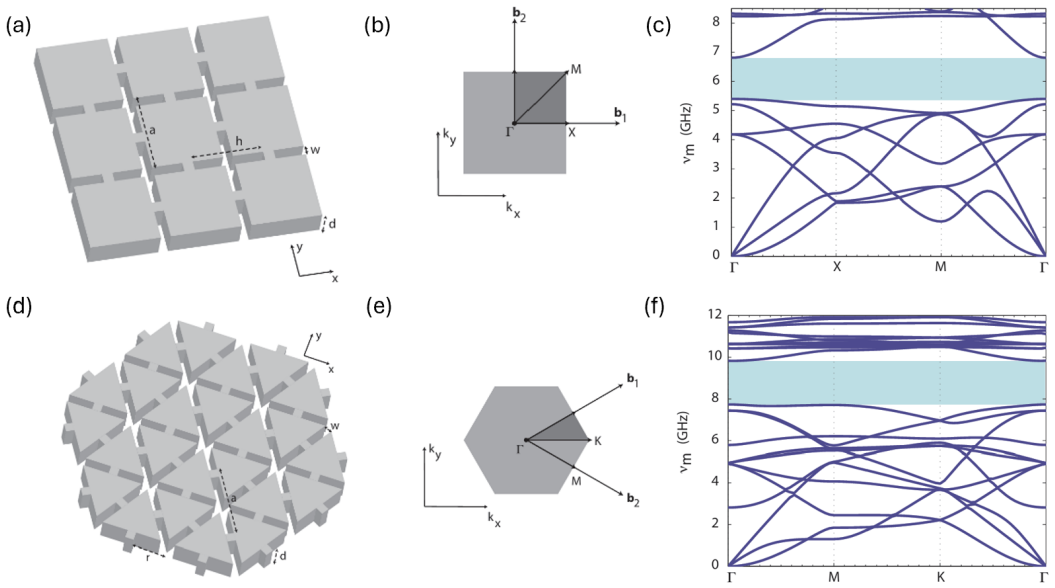

FIGURE 3.2. (a)(b) Square lattice design and its reciprocal space for phononic crystal shields. (c) Calculated band gap structure for the square lattice design shown in (a). (d)(e) "Snowflake" design and its reciprocal space for phononic crystal shields. (f) Calculated band gap structure for the "snowflake" design shown in (d). Taken from Fig. 3 and Fig. 5 from Ref.[74].

3.3 Si and Si_3N_4-Based Systems

Silicon has long been the leading material and industry standard for applications in both classical and quantum domains. No other semiconductor has achieved comparable dominance or undergone such extensive development, owing to silicon's excellent processing capabilities, low cost, high purity, and scalability [76]. Remarkable advances in the field of silicon quantum computing have been reported [77]. For optomechanical studies, with the implementation of phononic band gap engineering, acoustic modes with quality factor of Q=5×10^{10} has been reported [64], corresponding to a phonon lifetime of about 1.5 seconds.

Silicon Nitride (Si_3N_4) is another type of material that has drawn significant attention throughout the years. Earlier studies showed that in pre-stressed Si_3N_4 membranes and string nanomechanical resonators, high tensile stress dramatically reduces dissipation and leads to high Qf product [78, 79]. This phenomenon is called "dissipation dilution". Comparisons were made among high tensile-stress doubly clamped beams with doubly clamped beams and cantilevers made of a lower stress material, as well as cantilevers made of high stress material. In all cases, the doubly clamped high stress beams have the highest quality factors [80]. It was inferred that the high quality-factors be attributed to the increase in stored elastic energy rather than a decrease in energy loss [81].

Fig.3.3 shows the key features of a silicon nitride membrane device with honeycomb lattice as the phononic shield [7]. In the center, the lattice is interrupted by a small number of removed and displaced holes which forms a defect area where the mechanical mode is defined. This allows the mode to propagate evanescently into the soft clamping area and reduces the modes curvature which usually induces

dissipation. A Qf product exceeding 10^{14} Hz at MHz frequency combined with ng-masses has been achieved in this design.

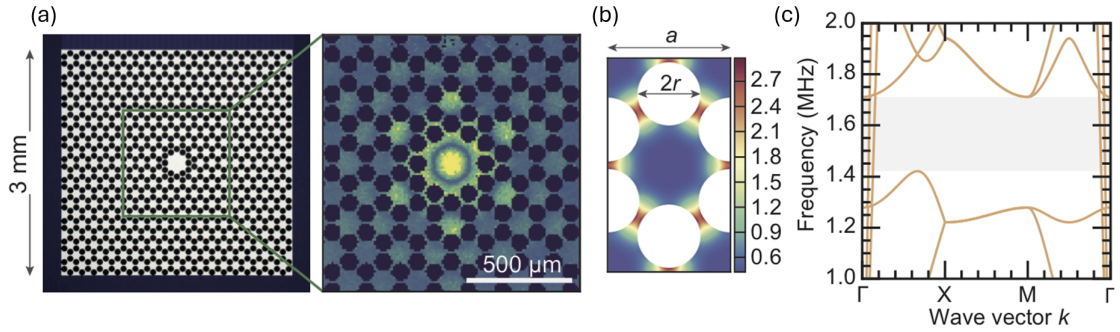

FIGURE 3.3. (a) A silicon nitride membrane patterned with honeycomb-shape phononic crystal structures and the out-of-plane mode displacement in the central defect area. (b) A unit cell of the phononic crystal lattice and its calculated phononic band gap structure (c). Taken from Fig. 1 from Ref.[7].

3.4 Diamond-Based Systems

Compared to silicon, diamond possess a large band gap and is the host material to many color centers with excellent properties for quantum applications. However, diamond processing has been difficult due to its high cost, chemical inertness and extreme hardness. Extensive studies and research have been devoted into the design and fabrication for diamond nanomechanical resonators [82]. Fig. 3.4 presents several types of designs that have been developed for the past few decades.

The simplest and widely used designs of resonators are cantilevers and double-clamped beams. They feature out-of-plane mechanical modes with relatively lower frequencies. The advantages of cantilevers and double-clamped beams include the convenience of driving and detection of mechanical modes, for example with optical interferometry and radiation pressure force for out-of-plane modes characterizations.

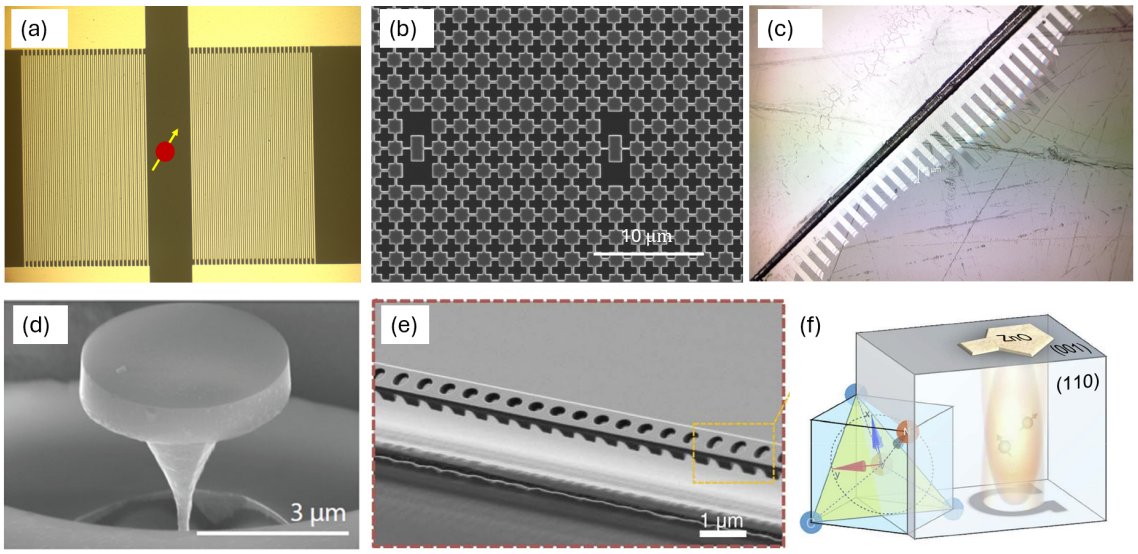

FIGURE 3.4. (a) Interdigital transducer (IDT) patterned on a layer of ZnO film on the surface of diamond for generating surface acoustic waves (SAW). (b) Electron microscope image of diamond Lamb wave resonators protected by phononic band gap structures. (c) A fabricated array of diamond cantilevers with varied length attached to the bulk of a diamond film. d) A diamond microdisk supporting both optical whispering gallery modes (WGM) and mechanical breathing modes. Image is taken from Fig. 3 from Ref.[8]. (e) Diamond optomechanical crystal taken from Fig. 2 from Ref.[9]. (f) A diamond high overtone bulk-mode acoustic resonator (HBAR) device that consists of a zinc oxide piezoelectric transducer patterned on the surface of a diamond substrate. Picture taken from Fig. 1 from Ref.[10].

Phononic engineering has also been implemented in diamond cantilever structures to mitigate clamping losses and enable a high Q-factor of up to 10^6 [43].

Diamond microdisk is a disk-shape resonator that works nicely as a cavity optomechanics platform [83]. The geometry supports both optical whispering gallery modes (WGM) and mechanical breathing modes that can be coupled to each other through radiation pressure force. The structure in Fig. 3.4 (d) shows a diamond microdisk that features a mechanical mode at GHz frequencies while supporting an optical mode with a high Q-factor. The dominant loss comes from the supporting pedestal connected to the base structure.

Diamond optomechanical crystals are great platforms for spin-mechanical studies [9]. These crystals support both optical cavity modes and mechanical modes, as can be seen in Fig. 3.4 (e). High frequency mechanical modes can be read out through the optical cavity with optomechanical interactions. Defect centers including SiV^- and NV^- centers can be implanted in the structure and interact with both the mechanical and optical fields due to the strong confinement. Up to date, acoustic Purcell effect has been observed with the spin states of a single SiV^- coupled to a 12GHz nanomechanical oscillator and a T_1-based spin-phonon cooperativity of 10 has been experimentally measured [84]. The challenges in the diamond optomechanical platform however include the requirement of tuning the optical cavity to the SiV^- resonance through either gas tuning or material deposition, which both induce significant damping to the mechanical mode.

As briefly discussed in Chapter I, surface acoustic wave (SAW) devices based on interdigital transducers (IDT) enabled success in electromechanical systems with superconducting qubits. In spin-mechanical studies, surface acoustic waves also coupled to single SiV^- centers through coherent and low-power acoustic control [85]. SAW structure is usually patterned on a piezo-electric material where electric signals convert to SAWs and the pitch determines the mechanical frequency, as is shown in Fig.3.4 (a).

Bulk acoustic resonators (BARs) on the other hand can support GHz mechanical modes while providing confinement of the modes through its Fabry-Perot cavity type of structure, as is shown in Fig. 3.4(f). The device typically is made of a thin piezoelectric film stacked between two planar boundaries which for the purpose of a high Q-factor, usually needs to be highly parallel. This can lead to large dimensions of BARs and sacrifice the spin-phonon coupling rate. New and better designs have

been realized in [86] where one surface is curved and matches the wavefront of the acoustic wave. This plano-convex design also works as a solid immersion lens (SIL) for enhancing photon collection efficiency.

Another type of resonator that could support high frequency GHz mechanical modes is a Lamb wave resonator (Fig.3.4(b)). It is a thin elastic plate with free boundaries and feature in-plane compression modes. Q-factors can potentially be greatly enhanced by embedding the resonator into a phononic band gap shield as previously discussed [44]. Mechanical clamping loss could also be reduced by connecting the resonator to the environment from the nodes of the mechanical modes.

In summary, mechanical structures vary from each other and each design or geometry feature their own advantages and weaknesses. It is crucial to explore an optimal design for a diamond nanomechanical resonator with compact mass, high Q-factor and desired frequency. In the following Chapter V and VI we will be presenting our success on diamond cantilevers and Lamb wave resonators. Before that, we will talk about diamond fabrication protocols in Chapter IV which is crucial for developing diamond nanostructures at the first place.

CHAPTER IV

FABRICATION OF DIAMOND NANOMECHANICAL RESONATORS

4.1 Overview

In this chapter, we discuss the fabrication of diamond nanomechanical resonators. Due to diamond's chemical inertness, extreme hardness, and high cost, its processing techniques are far less developed compared to those of other materials, particularly silicon. Significant research efforts have been devoted to developing methods for fabricating high-quality diamond nanostructures with excellent quality factors [43, 54, 82].

4.2 Diamond Thin Film Processing

In this section, we present our own diamond thin film processing procedure for fabrication of high-Q mechanical resonators for spin-mechanical studies. The process follows an approach developed earlier where a large-area suspended 2D structure is fabricated in a "membrane-in-bulk" way directly from a piece of bulk diamond [54]. This facilitates the robust handling of large area thin membranes. We'll first talk about the front side patterning including surface preparation and sample cleaning, then we introduce our backside thinning step to produce membranes at a thickness below 100nm or as thick as 3μm. At the end we introduce thermal annealing and wet chemical oxidization steps for post-fabrication treatment. Good coherence properties of color centers have been maintained after extensive processing steps.

4.2.1 Front Side Patterning

We purchase our bulk single-crystal diamond samples from Element Six, Inc. For spin-mechanical studies, we use electronic grade (EL) CVD diamond material with less than 5 ppb nitrogen concentration. The fabrication starts with a 4.5mm× 4.5mm bulk sample with a thickness of 0.5mm. For cutting and slicing, we send it to Applied Diamond, Inc and do easy axis polishing into 6 pieces of 30μm thick and 4mm×2mm membranes. The expected thickness wedge is less than 4μm while the actual turn-out wedge could be from less than 1μm to over 10μm along the 4mm-long side.

After receiving the sliced membrane samples, we rinse with acetone, IPA and DI water then check under the microscope for surface defects and contamination. After identifying a better side out of two surfaces, we mount the samples on a Si wafer with PMMA and let the worse surface face up. Then we use focused-ion-beam (FIB) to mill out labels for each sample near the edge of the surface. The patterns for the label are chosen such that they are asymmetric when viewing from the top and bottom, for the purpose of identifying the two surfaces. The energy for the ion beam is 21nA and the size of pattern is 100μm×50μm.

After labeling each sample, we use a hot mixture of sulfuric acid, nitric acid and perchloric acid with ratio 1:1:1 (tri-acid) to thoroughly clean the samples and remove possible damage or contamination induced during the slicing. The acid is set at 380°C and the process takes about 3.5 hours including cooling and heating up of the acid solution. Fig. 4.1 shows a setup for the tri-acid cleaning including a condensing part where housing water is flowing through for the entire cleaning. The flow rate of water is adjusted such that the air volume inside the apparatus tubing stays balanced, little or no hot acid vapor is escaping out of the waste bottle and no

water backflow is happening either. With the water cooling, hot acid vapor will keep flowing back into the container after evaporating. After the process, the samples are flushed out of the beaker and go through two DI water rinses to remove any acid residue.

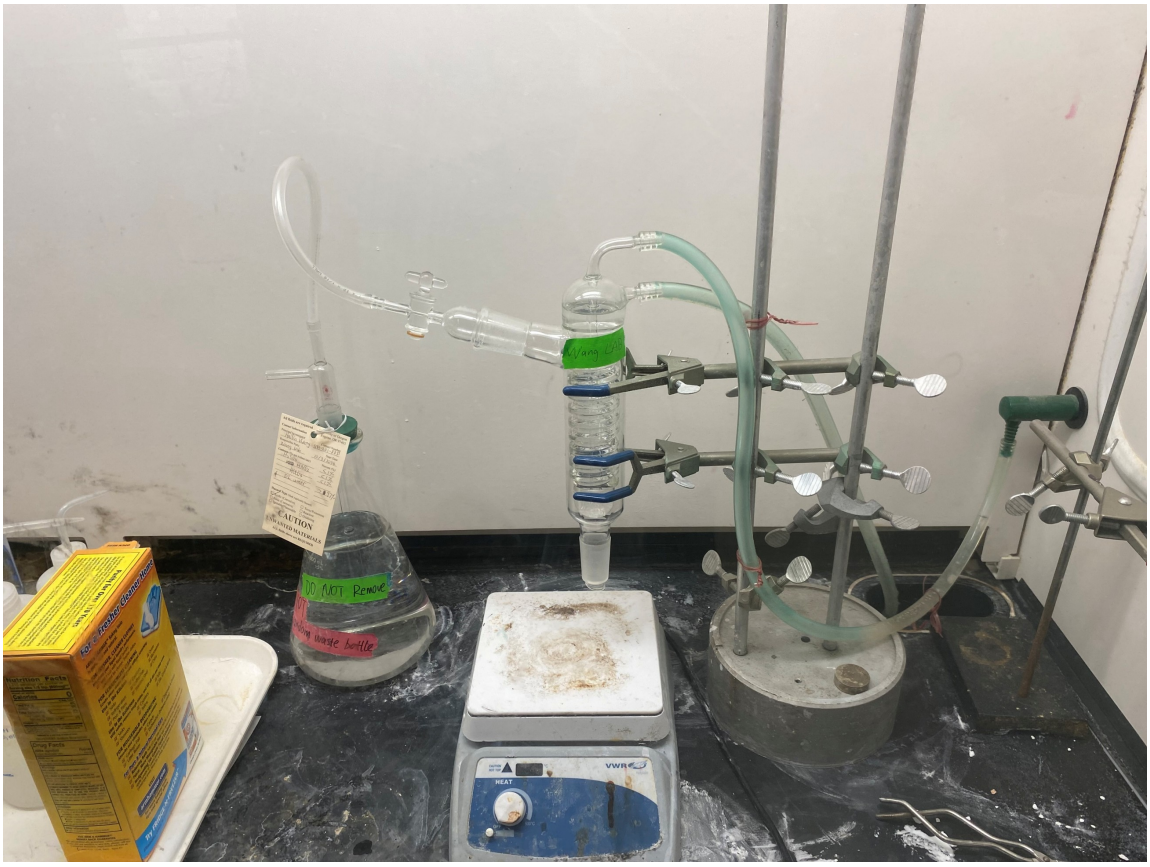

FIGURE 4.1. Tri-acid cleaning setup. A beaker with acids and the sample is placed on a hotplate and connected to a condenser with circulating cooling water. Upon heated up, acid vapors evaporate and condense, returning back to the beaker. The outlet of the condenser is connected to a waste collection bottle.

After tri-acid cleaning, the sample surface should be free from any contamination that would micro-mask during plasma etching. We then mount the samples with PMMA at the center of a two-inch sapphire wafer with the unlabeled (better) side facing up. The wafer is then loaded into an Oxford PlasmaPro 80 etcher for etching out about 2.5μm of surface layer with Ar/Cl_2 plasma. This step is for the

purpose of removing possible strained layer from the surface formed after the diamond cutting/slicing process, also smooth out the roughness [87]. After the Ar/Cl_2 plasma, we put the sample into tri-acid cleaning again for about 2.5 hours to remove the part of top layer that could be contaminated/roughened by the plasma etching.

The samples are then mounted with PMMA onto a 4-inch Si wafer with the etched surface facing up. The wafer is sent to Coherent, Inc or CuttingEdge Ions, Inc for N^{15+} or Si^{28+} ion implantation, depending on the purpose of experiments. Different implantation depths have been tested for samples with varied purposes. We chose an implantation angle of 7 degrees and at an ion energy of 150KeV for Si^{28}, the final stopping depth of implantation is about 100nm, which could be calculated with a simulation package called SRIM [88].

After obtaining the implanted samples, we do a sulfuric and hydrogen peroxide mixture with a ratio of 1:3 (piranha clean) to remove any dust from the membrane surface before further processing. The first step in the front side patterning is to deposit a layer of Si_3N_4 mask. The mask is required to have high selectivity against O_2 plasma etching during the future pattern transfer. To deposit high quality Si_3N_4 films, the diamond membrane is mounted with PMMA on a small Si_3N_4 wafer part and pre-baked at a temperature of about 150°C on a hot plate to get rid of any surface moisture, where bubbling or blistering of deposited films could happen otherwise. The sample is then transferred into the Oxford PlasmaPro 80 with a substrate temperature set at 25°C. The chamber is pumped down for a few hours for high vacuum into low 10^{-6} or 10^{-7}mtorr. Higher vacuum is crucial for rendering high quality Si_3N_4 film with good selectivity.

Plasma-enhanced chemical vapor deposition (PECVD) of Si_3N_4 happens at a gas composition of 16sccm SiH4 and 4sccm of N2. About 300nm of Si_3N_4 is deposited

for 5min and then baked on a hotplate at about 180°C for 10min. Baking of Si_3N_4 film was reported for improving film quality and selectivity. The sample is then checked under an optical microscope for any blistering or defects inside the film. When the chamber vacuum is bad, significant amounts of black dots can be seen inside the Si_3N_4 film, possibly due to interactions of Si with O_2. A selectivity check can be carried out at this step with a part of the membrane covered for O_2 plasma etching. The etching temperature is at 19℃ with 30sccm of O_2 flow rate. This step has reported very stable etch rate of 100nm/min on bare diamond. A good quality Si_3N_4 film shows a selectivity of above 1:20, corresponding to less than 5nm/min of etch rate with O_2. Fig. 4.2 shows a picture of blistering and black defects inside the Si_3N_4 film where low selectivity happened.

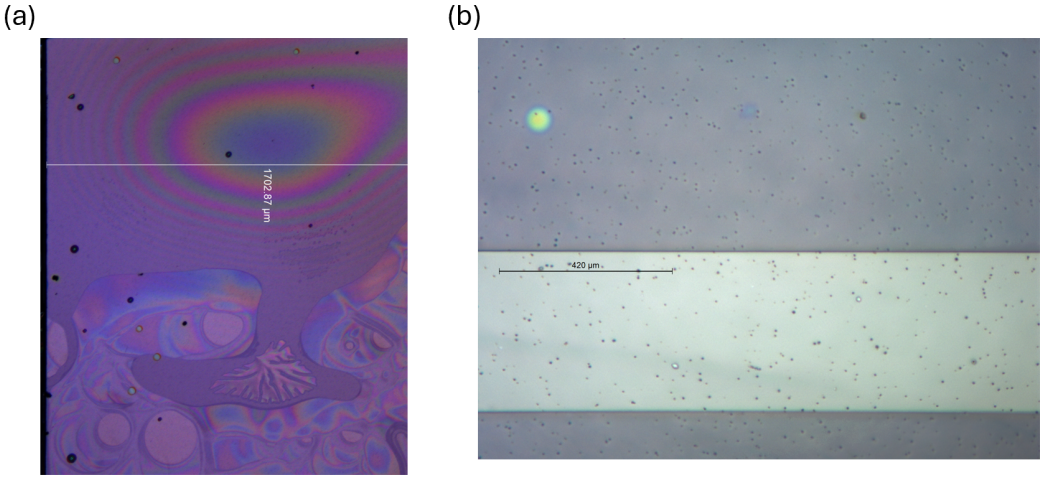

FIGURE 4.2. Blistering and bubbling of deposited silicon nitride film (a) and black defect dots (b) formed after PECVD process. Possibly due to bad vacuum or bad surface preparation.

The next step is to deposit a thin layer (10nm) of graphite as a conductive layer for the E-beam lithography. This is followed by a spin-coating of polymethyl methacrylate (PMMA) at a speed of 4000rps for 40s, rendering a 550nm layer of

E-beam resist on the diamond membrane. The coated PMMA layer is then baked on a hotplate with a temperature set at 180℃ for 10min. Depending on different types of experiments, various designs of patterns are imported into a Nanometer Pattern Generation System (NPGS) on an E-beam lithography tool (ThermoFisher Scientific Apreo 2 SEM). Before writing, a small scratch is made with a diamond scribe pen onto the PMMA layer at the corner of the diamond membrane to create defects or debris for later E-beam focusing. A dosage of about 300pA at 30keV was found to be optimal for lithography on 550nm thick of PMMA. After patterning, the sample was placed into a 1:3 mixture of MIBK: IPA for 1min for pattern developing, followed by IPA and DI water rinsing.

Pattern transfer was carried out with two steps of plasma etching. The first step is from PMMA to Si_3N_4 layer with CHF_3 plasma. This happens at a gas flow of 50sccm. The exact etch rate of CHF_3 on Si_3N_4 varies significantly according to chamber cleanness and vacuum condition, which could be indicated in the DC bias in the chamber. Too much dirt in the chamber will shorten the paths of plasma and therefore creates lower DC bias. It is especially crucial to tell when the Si_3N_4 is completely etched out. We intend to over-etch in this step to make sure all the Si_3N_4 near the corners and edges are completely gone, which would otherwise micro-mask in the O_2 plasma step and create rough profiles. The way we make sure that all Si_3N_4 is gone is through writing a long narrow rectangle at the other half of the diamond along with the real pattern. When the CHF_3 plasma step is close to an end, we use the diamond scribe pen to make small scratches on this long rectangular and check if the part exposed by the scratch shows signs of diamond surface getting etched, as could be seen from Fig. 4.3. If the part of diamond in the long rectangle

has been etched, the CHF_3 plasma then has removed all of Si_3N_4. Alternatively, a 10min etch usually is long enough for over-etching.

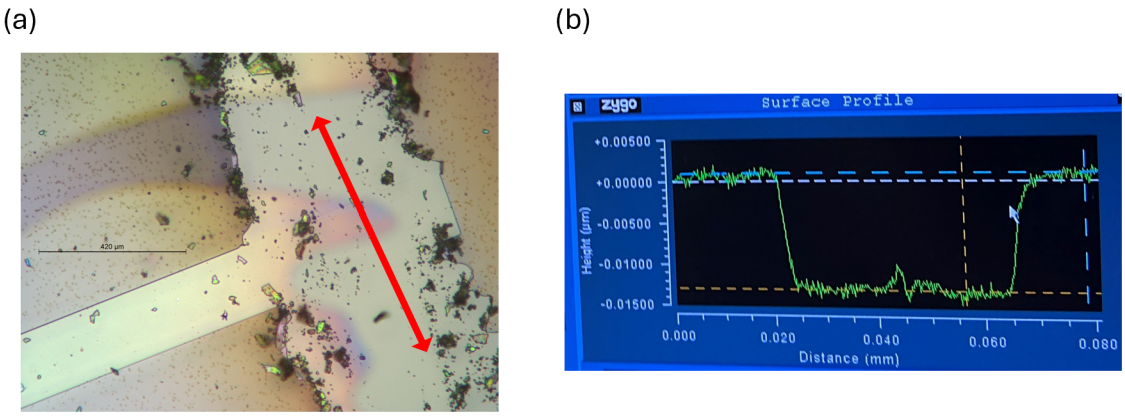

FIGURE 4.3. Over-etching of silicon nitride mask to prevent micro-masking in the following O_2 etching steps. The thickness step shown in (b) measured from the scratch (red arrow) in (a) shows the etching of bare diamond in the long rectangle area, indicating an over-etch of silicon nitride mask.

The second step of mask transfer is O_2 plasma etching of Si_3N_4 in the un-patterned part and diamond in the exposed (patterned) part. Based on the etch rate and selectivity, 10min of O_2 leads to 1μm of etched depth of diamond. It is worth noting that if the CHF_3 plasma etch in the previous step has removed the residual Si_3N_4 completely, then the O_2 plasma step should leave clean profiles in the etched diamond parts. Otherwise the micro-masking from residual Si_3N_4 would create dark spikes and grassy profiles in the part of diamond etched by O_2. A comparison of two cases can be seen in Fig. 4.4.

After the mask transfer, there should still be over 100nm thick of Si_3N_4 mask left in the un-patterned area. This part of Si_3N_4 will be important during the backside etching step to protect the front side diamond from getting etched by the Ar/Cl_2 plasma travelling underneath the sample. The sample will be submerged into acetone solution for an amount of time until the diamond membrane is released

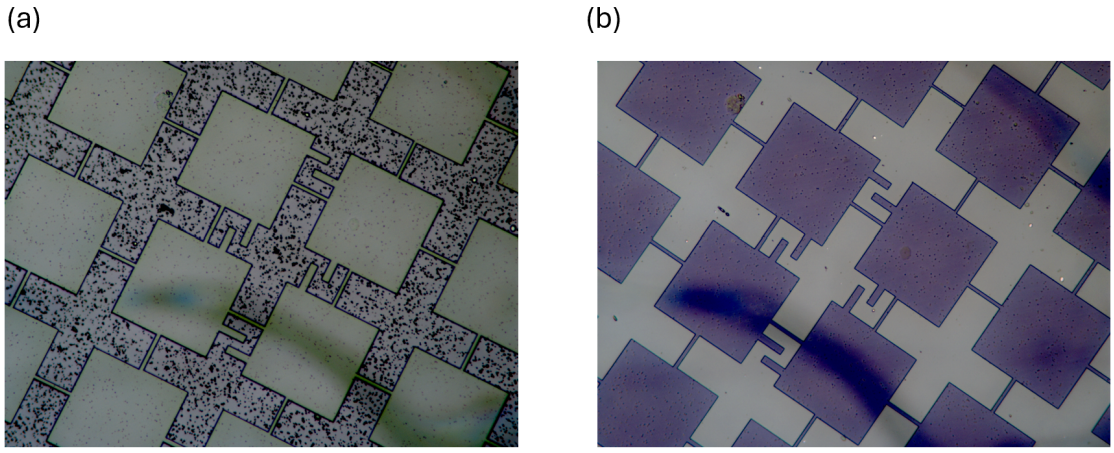

FIGURE 4.4. Comparison of diamond surface profiles after O_2 plasma etching. When the silicon nitride mask wasn't completely removed during the first mask transfer step, micro-masking and dark grassy profiles show up as in (a); With completely removed silicon nitride mask in the previous step, a clean profile is left in the patterned area as in (b).

from the Si_3N_4 carrier wafer. A routine of acetone, IPA and DI water is used to clean off any debris or dust before the backside etching.

4.2.2 Back Side Processing

For backside etching, we flip the diamond membrane over and mount the un-patterned half of the membrane with PMMA on a piece of sapphire wafer. To make sure only the patterned half is thinned down so that we still have the other half maintained at 30μm thickness for easy-handling with air-tweezer, we cover the un-patterned half of diamond with a U-shape sapphire shadow mask as shown in Fig. 4.5 (a). The purpose of the backside etching is to thin the diamond down to a thickness desired for the experiments and until the structure is released. However, experience has shown that prolonged plasma etching could lead to ion-trenching at the edge of the shadow mask where plasma gets deflected by the edge of the mask [89], as is shown in Fig. 4.5 (b). This could make the sample fragile or even break when lifted

up from the substrate. To avoid this, we place two pieces of sapphire shards with a thickness of 100μm at two sides of the diamond membrane, so the U-shape sapphire mask is not in direct contact with the diamond membrane which therefore avoids ion-trenching, as is shown in Fig. 4.4 (c)(d).

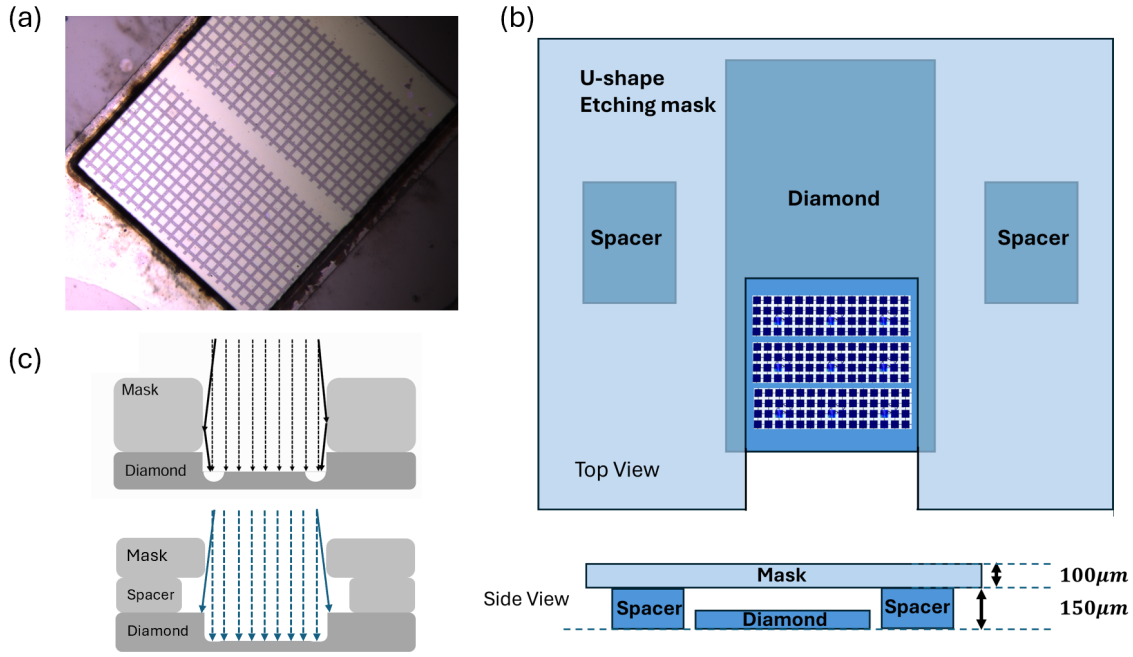

FIGURE 4.5. The use of a sapphire shadow mask for avoiding ion trenching. (a) A U-shape mask covering half of the diamond during the backside etching such that the thickness in this part still remains 30μm at the end. (b) The use of spacers between the shadow mask and the sample to avoid ion trenching. (c) Differences in etching profiles between the mask directly contacting the sample and not contacting the sample. Image is taken from Fig. 1 from Ref.[11].

The diamond thinning recipe is the same used in the etching of the diamond front surface after slicing and cutting. It consists of three repeated steps of 10min Cl_2 etching with a gas flow of 16sccm, then 2min of O_2 etching at a RF power of 100W (hard O_2 step) with a gas flow of 30sccm, then 10min of O_2 etching with zero RF power and 500W ICP power (soft O_2 step) at a gas flow of 30sccm. These combined give an etch rate of $\sim$2.7μm/cycle and we repeat this recipe for 10 or 11 times

until the patterned part thickness is under 1μm. The thickness characterization is carefully carried out with an optical profilometer (Zygo NewView 7300). The diamond membrane will also start to show color fringes when the thickness is below around 2μm.

Near the end of the diamond thinning process, we switch completely to soft O_2 process to gradually thin the membrane down to the desired thickness. Research [87] has shown that hard O_2 and Cl_2 plasma steps tend to induce roughness and contamination into the diamond lattice, causing severe optical degrading of color centers in diamond including spectral diffusion and charge fluctuations, especially for NV^-. Soft O_2 steps [54] have shown to be effective in reducing the damage. We carry out 2h of soft O_2 process at an ICP power of 500W, then 2h of soft O_2 process at an ICP power of 200W, then 0.5h at 100W and 0.5h at 50W. Note that SiV^- comparing to NV^- are less susceptible to surface electric fields and contaminations, therefore soft O_2 etching may not be required for SiV^- except for accurate controlling the final thickness.

Fig. 4.6 shows images of a diamond membrane with released patterned nanomechanical structures. The color fringes indicate thickness variations across the whole sample, with one cycle of color fringe corresponding to a variation of about 110nm thickness for the refractive index of diamond. The shape and placement of the U-shape mask can also be seen in the picture, where non-uniform etch rates near the edges of the mask lead to roughness for the diamond surface underneath the mask.

(a) (b)

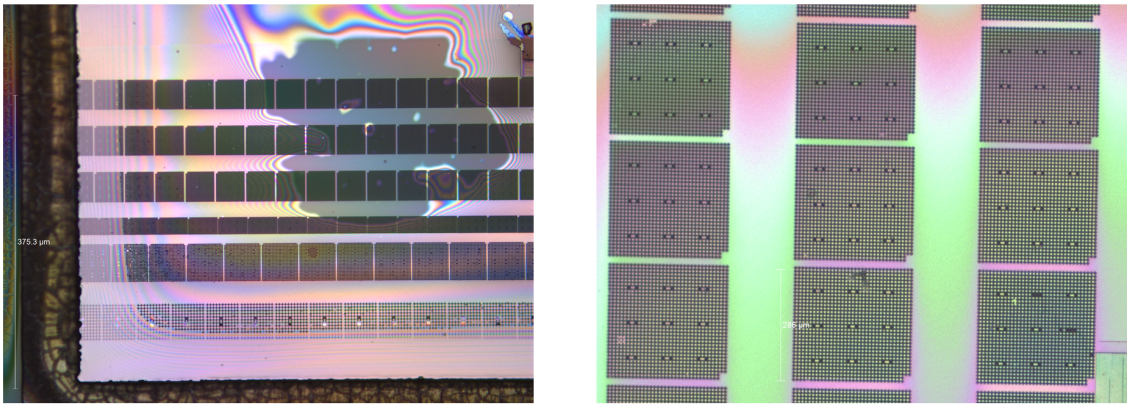

FIGURE 4.6. (a) Released diamond membrane structures after the backside etching. Thickness gradient near the shadow mask can be seen where each cycle of color fringe corresponds to about 110nm of thickness variation. (b) A zoom-in look of the etched patterns with Lamb wave resonators.

4.3 Thermal Annealing and Surface Termination

After plasma etching, we place the diamond membrane together with the attached sapphire substrate into a H_3PO_4 acid solution at 160°C to remove the Si_3N_4 layer on the front side. Then the membrane goes through piranha cleaning, acetone, IPA and DI water to thoroughly remove any dirt attached to the sample. The sample is then placed into a clean shallow glass dish and placed onto a hotplate at above 100°C to dry out any moisture.

The next important step is to do thermal annealing of diamond membranes where color centers including SiV^- and NV^- are formed under high temperatures. The range of 400-1200°C is crucial for the formation of stable color centers [89]. At 400°C, vacancies and interstitial nitrogen atoms diffuse and annihilate with each other. Around 800°C, vacancies gain mobility and combine with nitrogen or silicon atoms to form stable defect centers. At temperatures above 800°C, the vacancies become highly mobile, however reduction of NV formation rates has been indicated.

At even higher temperatures, additional defects - including divacancies, hydrogen and sp^2-type defects become mobile and get eliminated. For temperatures at or above 1200°C, annealing has shown significant improvement for the coherence properties of implanted NV centers.

Fig. 4.7 (a) shows our setup for the thermal annealing process and (b) shows the recipe for the temperature control. The sample is placed onto a ceramic heater plate (HTR100) purchased from Tectra, Inc which is mounted inside a 6" OD stainless steel chamber with CF sealing. A C-type thermometer is mounted in contact with the heater plate at one end and the other end is connected to the electrical feedthroughs on the heater stage. Temperature and vacuum pressure are read out through an Arduino board which transmits the readings to a laptop for data analysis and logging. The chamber is being pumped on with a turbo pump (Leybold Turbovac MAG W 300 iP) and a roughing pump (Edwards vacuum nXDS10i). Ahead of the annealing recipe, the chamber and the connecting bellows are wrapped by heating tapes while pumped by the turbo and roughing pump and are baked overnight to get rid of water vapors inside the system. After the annealing recipe starts, a cold cylinder with water cooling feedthroughs connected to a chiller (NESLAB RTE-110) wraps around the sample chamber and cools it down during high temperature steps.

For NV centers in diamond, an additional O_2 annealing step has shown to be effective in reducing charge fluctuations and producing coherent NV^- centers [90]. Surface exposure and termination with O_2 helps the conversion of NV^0 to NV^- centers at a temperature around 465°C. Specifically, the temperature range of 375-450°C oxidizes sp^2 and sp^3 carbon species with different rates while around 400-430°C, oxidization of sp^2-bonded carbons happens with little or no loss induced to diamond. Fig. 4.8 (a) shows the apparatus of our O_2 annealing setup. The sample

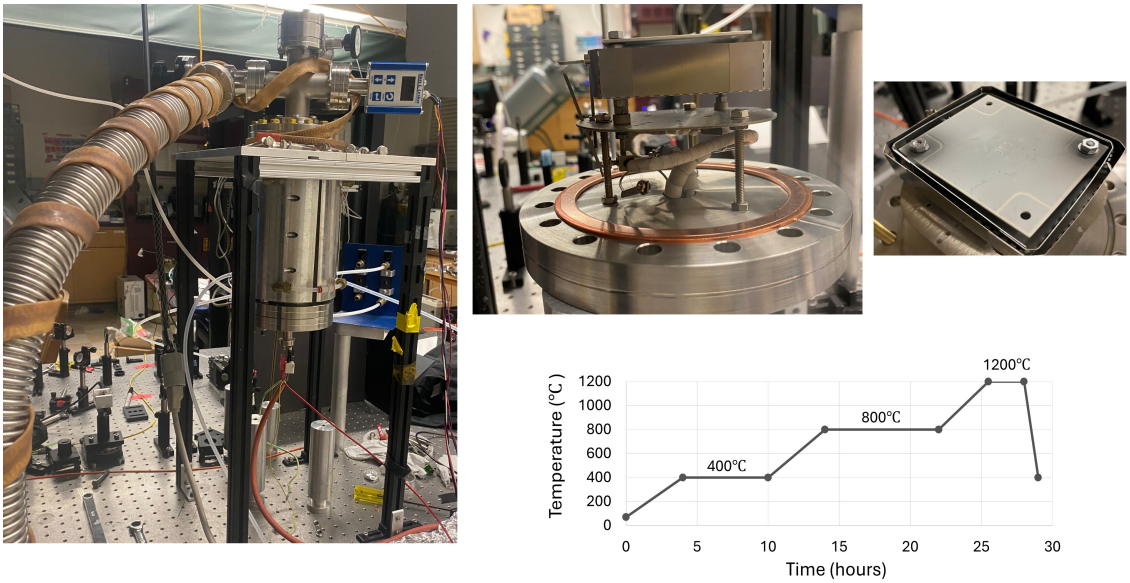

FIGURE 4.7. Thermal annealing setup, heater stage and a ceramic heater plate. The recipe for thermal annealing temperatures is indicated and the whole recipe takes about 29 hours.

is placed inside a glass tubing mounted inside a heater furnace (Lindberg/Blue M Tube Furnace). Several pump-and-purge cycles with O_2 are performed prior to the annealing step to remove any residual gases from the tubing. Fig. 4.8 (b) shows the O_2 annealing recipe where temperature is slowly ramped to 465°C then stays for 2.5h before cooling down.

After the final thermal annealing or O_2 annealing step, the sample goes through one last tri-acid cleaning to remove the surface layer oxidized during the high temperature steps, especially at the stage of 800°C and 1200°C. After drying out, the sample can then be mounted into the cryostation or a room-temperature optical confocal setup for characterizations on color centers.

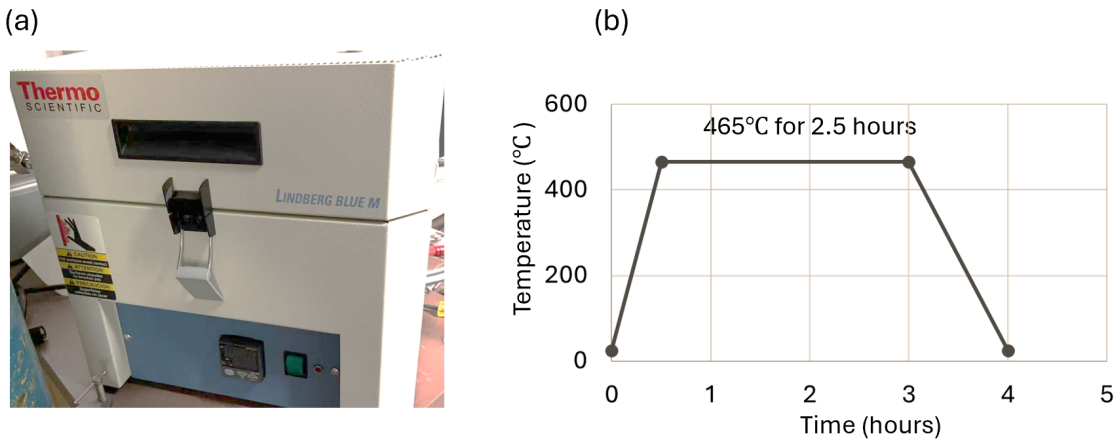

FIGURE 4.8. (a) O_2 annealing setup with the use of a heating tube furnace. Recipe for annealing temperatures is indicated in (b).

CHAPTER V

DIAMOND CANTILEVERS PROTECTED BY A PHONONIC BAND GAP

This work was done in collaboration with Ignas Lekavicius and Hailin Wang and has been published in Nano Letters as Ref. [43]. Ignas developed the diamond nanofabrication techniques and Hailin designed, supervised the research project, analyzed the results and prepared the manuscript. I performed the fabrication and characterization of the sample and conducted the experiment.

5.1 Introduction

Among various choices of resonator geometries, cantilevers stand out for their simple first-order out-of-plane motion which can be detected with optical interferometry and driven easily. Here we talk about the design, fabrication, and characterization of diamond cantilevers attached to phononic crystals. We show how the phononic band gap can effectively protect the mechanical modes and enable a Q-factor of 10^6 for diamond resonator frequencies as high as 100MHz.

5.2 Device Design and Phonon Band Gap

In the design, we choose cantilevers with a width of 4 μm and with various lengths attached to the squares in the phononic crystal lattice. An optical image is shown in Fig. 5.1(a) and Fig. 5.1(b) shows an optical image of a section of the phononic structure. The lengths of the cantilevers range from 11.5 to 15 μm. The width is chosen such that enough color centers can be found in one cantilever. The squares with cantilevers attached are surrounded by at least four layers of squares that have no cantilevers attached for an effective isolation of mechanical modes. The width

and length of the thin bridge is 1.3 and 20 μm, respectively. Simulation shows that thinner bridges lead to wider band gaps but also face the risk of breaking during membrane processing.

The band structure is calculated with the finite element COMSOL Multiphysics software package [75] and with diamond Young's modulus E= 1050 GPa, Poisson ratio ν= 0.2, and mass density ρ= 3539 kg/m^3. Fig. 5.1(c) shows calculated phononic band structures of the square lattice with a film thickness of 2.5 μm where the shaded areas highlight phononic band gaps. The lattice period is 76 μm for a band gap centered around 30MHz, and we also see phononic band gaps near 50 MHz and 95 MHz from the band structure at the same time. The desired final thickness of membrane is 2.5 μm for maintaining good coherence properties of NV^- centers. NV^- centers in diamond membrane with thickness below 1um have shown broad linewidth and unstable charge states due to surface fluctuations [43].

5.3 Thickness Variation of Diamond Thin Film

The fabrication of diamond phononic structures follows closely the membrane-in-bulk approach described in Chapter IV, for which a suspended 2D phononic structure is fabricated directly from a bulk diamond film. A limitation of our diamond nanofabrication approach is that the suspended structure retains the thickness variation of the initial diamond film, which results from the slicing and polishing of the thicker diamond film [54]. The thickness of the phononic structure can vary from 2.2 μm to 2.7 μm across the sample, leading to optical interference fringes as shown in Fig. 5.1(b). Each color fringe corresponds to an estimated thickness variation of 110 nm. Since the phononic band gap depends on the thickness of the structure, it can be difficult to determine the precise spectral positions of the phononic band gap.

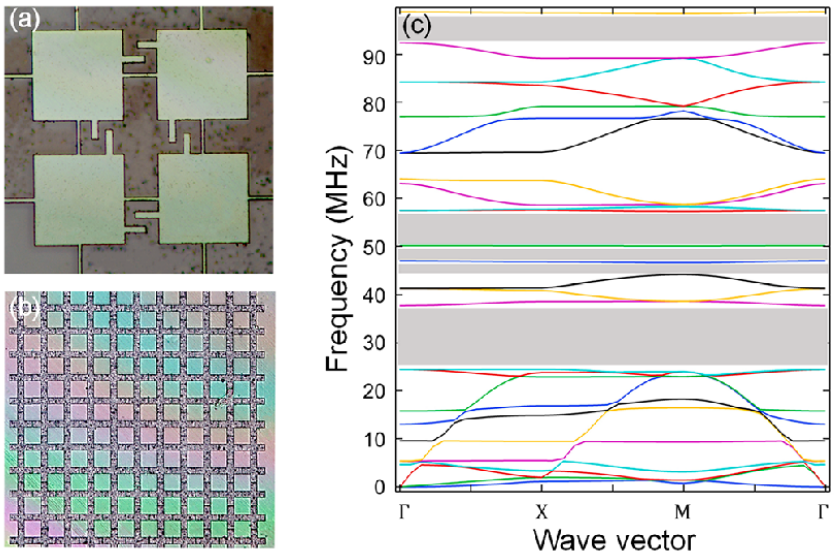

FIGURE 5.1. Optical image highlighting cantilevers embedded in a square phononic lattice structure. The lengths of the cantilevers range from 11.5 to 15 μm. The lattice period is 76 μm. The width and length of the bridge is 1.3 and 20 μm, respectively. (b) Optical image of a section of the phononic structure. The structure is completely released, with a thickness near 2.5 μm. The color fringes in the image reflect thickness variations about 110 nm across one fringe. (c) Calculated phononic band structures of the square lattice with a film thickness of 2.5 μm. The shaded areas highlight phononic band gaps.

For an estimation, we plot in Fig. 5.2 the calculated edges of the lowest frequency phononic band gap as a function of the thickness of the structure. The calculation shows that the variations of the lower band edge are on the order of 2 MHz and are considerable smaller than the variations of the higher band edge. Therefore, our design of band gap structures is robust against thickness variations in our sample.

5.4 High Q-Factor Diamond Cantilever Modes

5.4.1 Optical Interferometry Setup

For the characterization of out-of-plane mechanical modes in a cantilever, we have used the radiation pressure from a focused laser beam (with a wavelength

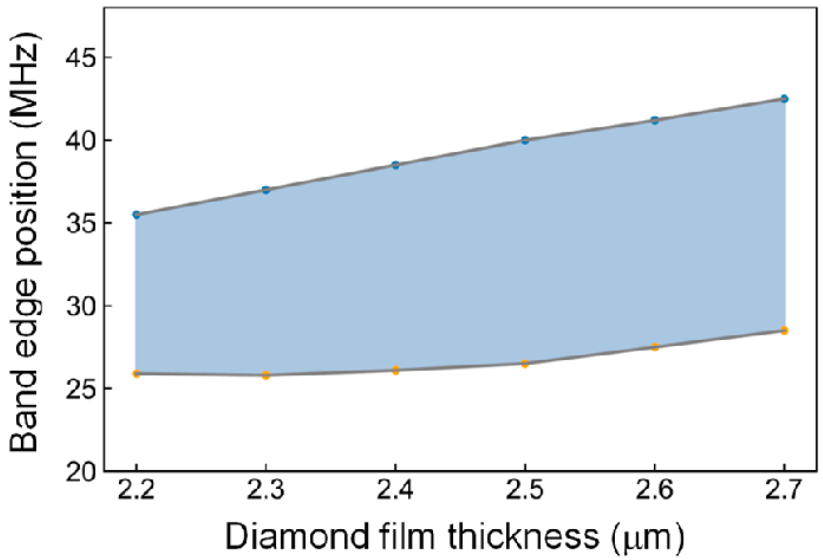

FIGURE 5.2. Calculated phononic band edge positions as a function of the diamond film thickness.

near 1.55 μm) to excite the mechanical modes in the cantilever, for which the intensity of the laser beam is modulated sinusoidally in time with an Intensity Electro-Optic Modulator (Thorlabs LN81S-FC). The intensity-modulated laser is then amplified in a fiber optical amplifier (Amonics AEDFA-33-B-FA). At the output end, an adjustable fiber collimator (Thorlabs CFC11A-C) changes the beam profile of the 1.55μm laser to optimize its spot size on the diamond cantilever, since general objectives feature considerable spherical aberration for wavelengths at 1.5μm compared to visible wavelengths. For the cantilever dimensions utilized in this experiment, a 40× objective (Olympus LUCPlanFL N) is enough to create a tight focus for effective mechanical driving.

Mechanical vibrations of the cantilever are detected with the standard approach of laser interferometry, with the diamond phononic structure mounted on a sapphire wafer, as illustrated in Fig. 5.3(a). For the laser interferometry, the reflection of a red laser beam (with a wavelength near 637 nm) from the cantilever and that

from the sapphire wafer are coupled into a single mode fiber. The air gap between the two reflection surfaces can be from a few μm to a few tens of μm, creating a phase difference between the reflections from two surfaces. The output from the fiber is detected with a photodiode (New Focus 1801). A network analyzer (Keysight P5001A) is used for the measurement of the spectral power density of the detected signal as a function of the excitation frequency. For experiments at low temperature, the sample is mounted on a cold finger in an optical cryostat (Montana Instrument S50) operating from temperatures between 4K to 300K. Fig. 5.3(b) shows an example of the spectral response of the fundamental out-of-plane mode in a cantilever obtained at 8 K. The spectral linewidth obtained (7.6 Hz) corresponds to Q=4 $\times$ 10^6.

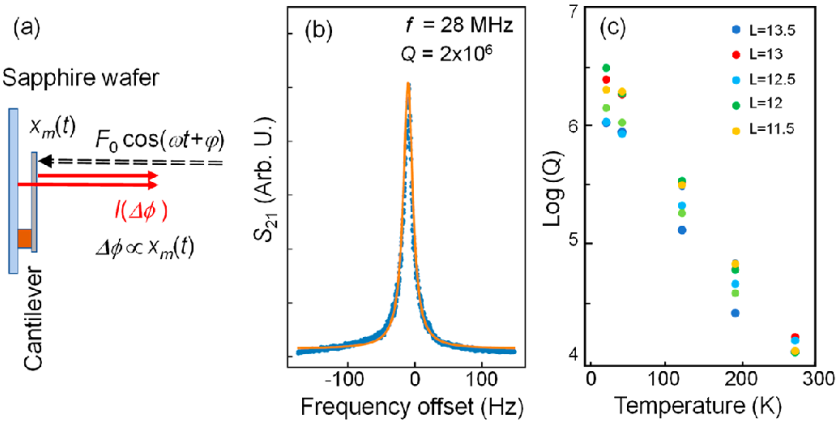

FIGURE 5.3. (a) Schematic depicting the excitation of out-of-plane modes in a cantilever with an intensity-modulated laser beam and the detection of the mechanical vibration with laser interferometry. (b) Spectral response of the fundamental out-of-plane mode in a cantilever obtained at T=8 K. The solid line is a least square fit to a Lorentzian. (c) Temperature dependence of Q for fundamental out-of-plane modes in cantilevers with their lengths indicated in the figure.

5.4.2 Effects of Phononic Band Gap

An important question, which needs to be resolved experimentally, is whether robust protection of the mechanical modes by the phononic band gap can still be

preserved in the presence of the inevitable thickness variations. To demonstrate the protection of the mechanical modes by the phononic band gap even in the presence of the thickness variations, we have used a large number of cantilevers, which feature different lengths and thus different resonance frequencies. Fig. 5.4 plots the Q-factors of the mechanical modes obtained from these cantilevers at temperatures near 8 K as a function of the corresponding resonance frequencies. For comparison, we also plot as shaded areas in Fig. 5.4 spectral ranges of the calculated band gaps for the square lattice, for which a structure thickness of 2.5 μm is used. Note that in addition to the fundamental out-of-plane modes, higher order modes can also be observed in the interferometry measurements. The Q-factors plotted near the second and third band gaps in Fig. 5.4 are obtained from the higher order mechanical modes.

As shown in Fig. 5.4, mechanical modes that are inside the band gaps of the phononic crystal feature Q-factors near or significantly above 10^6. For many of these modes, a product greater than 10^{14} is observed. Note that it is much more difficult to excite and observe higher order mechanical modes with frequencies above the second band gap than the modes with much lower frequencies. For the high frequency modes, only modes with ultrahigh Q can be observed. As such, we have only examined the high frequency modes in the third band gap in a few cantilevers.

Fig. 5.4 also shows that as the mechanical resonance frequencies approach and then cross the lower frequency band edges, the Q-factors increase by nearly three orders of magnitude. Although we cannot precisely determine the band edge as discussed earlier, this large increase in the Q-factor occurs in a frequency range of only a few MHz, in agreement with the band gap calculations presented in Fig. 5.3.

The protection and isolation of the mechanical modes by the phononic band gap can also be seen from the COMSOL simulations. The inset in Fig. 5.4 shows, as an

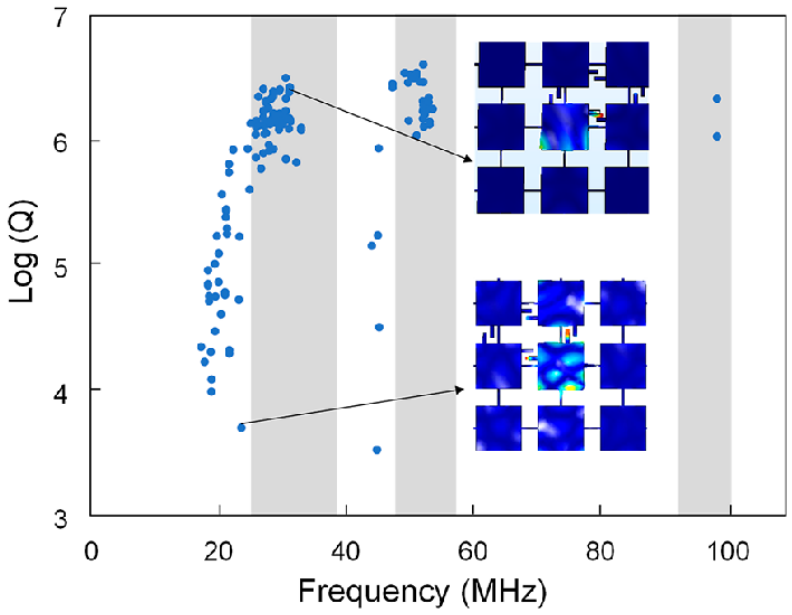

FIGURE 5.4. Q-factors obtained as a function of the resonance frequencies. The shaded areas indicate the calculated phononic band gaps of the square lattice with a diamond film thickness of 2.5 μm. The inset shows the COMSOL simulation of the mechanical displacement patterns of the two mechanical modes indicated in the figure. For the mode inside the gap, the displacement is confined to the square that hosts the cantilever. For the mode outside the gap, the displacement spreads out to neighboring squares.

example, the calculated mechanical displacement patterns of two mechanical modes. For the high Q mode inside the band gap, the displacement is confined within the square attached to the cantilever, indicating the isolation of the mechanical mode by the phononic band gap. In comparison, for the low Q mode outside the band gap, the displacement spreads out to neighboring squares.

5.4.3 Temperature Dependence of Mechanical Q-Factor

As we have discussed in Chapter III, quality factors of mechanical resonators depend strongly on temperature. Especially, the strong temperature dependence of intrinsic material losses highlights the importance of conducting measurements

across a broad temperature range, from room temperature down to millikelvin levels. In Fig. 5.3(c), we show that the Q-factors increase by more than two orders of magnitude as the temperature decreases from room temperature to 8 K. Since we expect the clamping or structural loss to be independent or only weakly dependent on temperature, the strong temperature dependence shown in Fig. 5.3(c) indicates that Q-factors at temperatures as low as a few K are primarily limited by materials loss. In this regard, additional experiments at temperatures as low as a few mK are needed to determine the relevant mechanisms of mechanical damping in diamond nanomechanical resonators.

We briefly introduce our experiments and measurements on mechanical Q-factors while collaborating with Oak Ridge National Laboratory. To characterize mechanical modes at temperatures as low as possible, our cantilever sample was thermally anchored to the mixing chamber of a dilution refrigerator (Leiden Cryogenics CFCS81-1000M) with temperature ranging from ∼50mK to 4K. We implement two types of measurements on acoustic modes: Spectra scan and Ringdown measurements. Spectra scan at 4K is convenient for searching mechanical modes in a broad range but could induce the broadening of mechanical linewidth due to long time averaging of frequency jitters. Ringdown measurements otherwise is capable of measuring the mechanical lifetime while at the same time minimizing power inputs into the dilution fridge by adjusting duty cycles of excitation lasers.

The same optical interferometry setup was used for the mechanical modes characterization in a dilution fridge. The reflection of a 532nm laser was collected with an objective with NA=0.82, followed by an optical 8-f collimation system installed in a cold-insertable probe in the refrigerator [91]. The signal exits an optical window at the top of the refrigerator then coupled into a multi-mode fiber with a

diameter of 10 μm and then sent to the photodiode. For the ringdown measurements, the pulse cycle was determined by the power input and lifetime of the mechanical mode. For a cantilever of frequency at 30 MHz with a Q factor of 10^6:

$$Q = \pi \tau f \tag{5.1}$$

Where τ is the phonon lifetime, obtained from fitting the decay curve in a ringdown measurement. f is the frequency of mechanical resonance. We therefore get an estimated lifetime of about 170ms for the cantilever mode used.

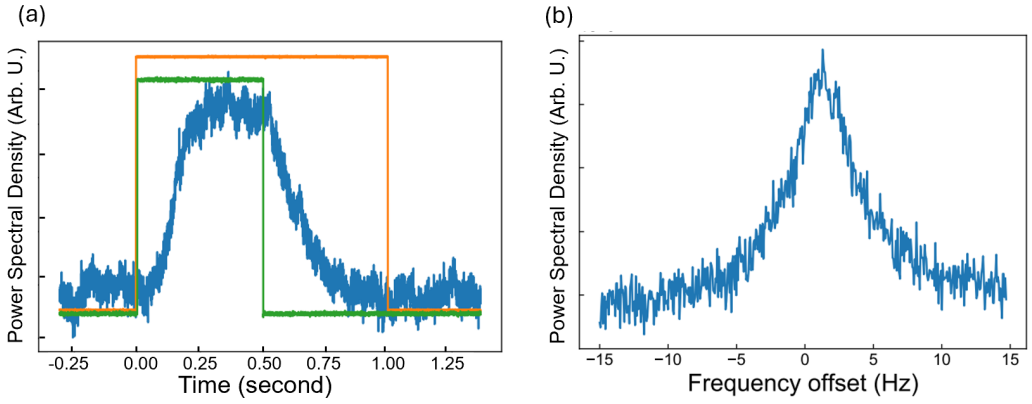

FIGURE 5.5. Ringdown measurement and spectrum scan on the Q-factor of a diamond cantilever at 4K. (a) Excitation laser (green pulse) turns on for 0.5s, followed by the natural decay of the oscillations after turning off. Orange pulse shows the duration of the measurement laser carrying the information of the mechanical motion. (b) A spectrum scan of the mechanical resonance by scanning the driving laser frequency.

Fig. 5.5 (a) shows an example of a ringdown measurement at a temperature of 60mK. We turn on the 1550nm excitation laser (green pulse) for about 0.5s, during which the cantilever oscillations build up and stabilize. Then the excitation laser is turned off, the decaying oscillator signals carried by the reflection of 532nm laser (orange pulse) from sample gets sent to a Lock-in Amplifier (Stanford Research

Systems SR844), which has a reference signal set at the same frequency of the mechanical driving (excitation). We choose a duty cycle of 1:100 and an averaging time of 15min per data point. From (a), we extract a Q-factor of about 14 million. Fig. 5.5 (b) shows a spectrum scan of one cantilever mode at 4K, with frequency at 25MHz and a Q-factor of 2.5million, obtained from the FWHM.

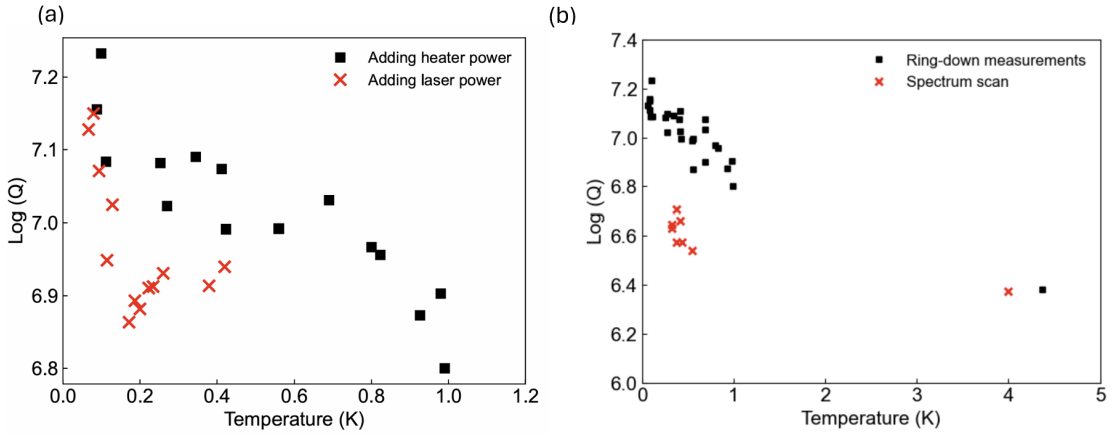

FIGURE 5.6. Temperature dependence of Q-factors of a diamond cantilever measured in a dilution refrigerator at low temperatures. (a) A comparison of Q-factors measured with gradually increasing input laser powers (red cross) or adding heat from a stage heater (black square). It can be seen that Q-factors show faster decline while adding laser powers compared to adding heat from heater, possibly due to poor thermal anchoring of the sample to the stage. (b) A comparison of Q-factors obtained from ringdown measurements (black) and spectrum scan(red) as adding heat from a stage heater. The temperature gap between 4K and 1K is due to the difficulties of achieving stable temperatures within this temperature range in our dilution fridge setup.

Next, we lower the temperature of the mixing chamber of the dilution fridge to below 100mK and then slowly heat it up to 1Kelvin. During heating up, we measure the Q-factors at different temperatures through ring-down measurements and spectrum scan. Ring-down measurements are necessary for maintaining the low temperature below 1K through reducing the duty cycle of power used, and spectrum scan is suitable for higher temperature measurements. We choose two approaches

for heating up the sample: We can gradually increase the power of input lasers, or we can raise the temperature by adding heat from a stage heater. Fig. 5.6 (a) shows a comparison of Q-factors measured with two approaches. It can be seen that Q-factors show faster decline while adding laser powers compared to adding heat from heater. This is possibly due to poor thermal anchoring of the sample to the stage. Fig. 5.6 (b) shows a comparison of Q-factors obtained from ringdown measurements and spectrum scan as temperature goes up. As can be seen, spectra scans show lower Q measurements compared to ringdown measurements, possibly due to the long-time averaging of frequency jitters from the spectra scans. Note that there is a temperature gap in Fig. 5.6(b) from 4K to 1K and this is due to the difficulties of achieving stable temperatures within this temperature range in our dilution fridge setup.

In summary, we have achieved a product exceeding 10^{14} by using diamond cantilevers attached to a phononic square lattice. Our detailed experimental studies demonstrate the robust protection of mechanical modes by phononic band gaps and indicate that the mechanical Q-factors obtained at a few K are still limited by materials loss. Diamond nanomechanical resonators protected by a phononic band gap can therefore open exciting opportunities for spin-mechanics studies. Our numerical estimations indicate that $C > 1$ is achievable with the parameters of the cantilevers realized here, for example through the strong excited-state strain coupling via a Raman transition [92].

CHAPTER VI

ULTRACOHERENT GIGAHERTZ DIAMOND SPIN-MECHANICAL LAMB WAVE RESONATORS

This work was done in collaboration with Ignas Lekavicius, Jens Noeckel and Hailin Wang and has been published in Nano Letters as Ref. [44]. Ignas developed the diamond nanofabrication techniques, Jens conducted the theoretical calculation, simulation based on experimental data and Hailin designed, supervised the research project,analyzed the results and prepared the manuscript. I performed the design, fabrication, characterization of the sample and conducted the experiment.

6.1 Introduction

As discussed in Chapter III, the further experimental advance of quantum spin-mechanics requires the development of ultracoherent diamond nanomechanical resonators at a GHz frequency. Ultracoherent GHz nanomechanical resonators have been realized with silicon optomechanical crystals embedded in a phononic crystal lattice [64]. Fabricating a diamond optomechanical crystal while integrating with a phononic band gap shield however remains difficult [9]. Here we demonstrate a diamond LWR featuring a fundamental compression mode with f_m=0.977 GHz and with Q as high as 1.2×10^7 at temperatures near 7K. The $Q \cdot f_m$ product achieved is comparable to or exceed that of the state-of-the-art silicon optomechanical crystals embedded in a phononic band gap acoustic shield at similar temperatures [64, 93].

6.2 Device Design and Phonon Band Gap

A Lamb wave resonator (LWR), which is essentially a thin elastic plate with free boundaries, provides a simple geometric structure for GHz nanomechanical resonators. As illustrated in Fig. 6.1(a), a thin rectangular diamond plate with a length of 9.5 μm, embedded in a square phononic crystal lattice, features a fundamental compression mode with f_m near 1 GHz. For the square lattice, the phononic band structure of the symmetric (with respect to the midplane of the plate) compression modes exhibits a large energy gap that protects the fundamental compression mode as in Fig. 6.1(b). Fig. 6.1(c) shows a scanning electron micrograph (SEM) of a diamond phononic structure fabricated with the design shown in Fig. 6.1(a).

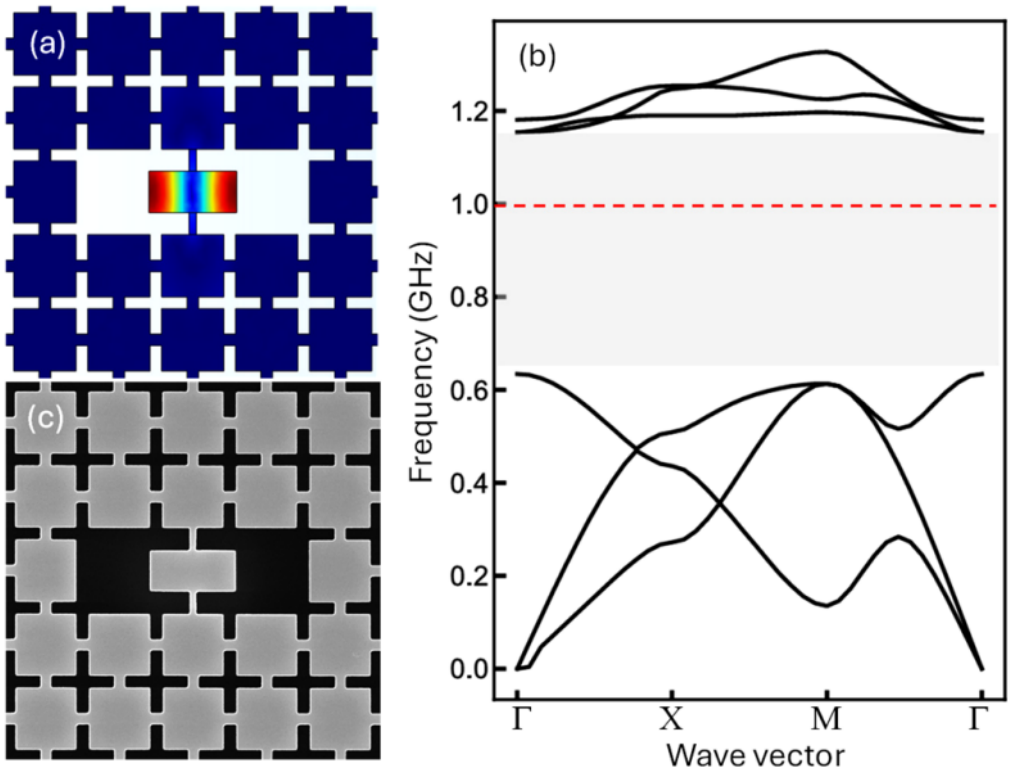

FIGURE 6.1. (a) A LWR with dimension (9.5, 4.5) μm, along with the calculated displacement pattern of the fundamental compression mode, embedded in a square phononic crystal lattice with a period of 8 μm. The dimension of the bridges in the lattice is (1.25, 1.25) μm. (b) Phononic band structure of the symmetric modes (with respect to the midplane of the plate) of the square lattice calculated with the finite element COMSOL Multiphysics software package and with Young's modulus E= 1200 GPa, Poisson ratio ν= 0.07, and mass density ρ= 3500 kg/m^3. The phononic band gap shields the fundamental compression mode with a frequency near 1 GHz (the dashed line). (c) Scanning electron micrograph of a LWR embedded in a phononic square lattice fabricated from a diamond thin film according to the dimensions given in (a). The sample thickness is 1.5 μm.

For the design, we also included 2GHz, 3GHz and 4GHz Lamb wave resonators in the fabrication. This is achieved by scaling the overall dimensions of 1GHz resonators and phononic structures down by different scaling factors. As dimensions go smaller, the ratio of the width of band gap versus the resonator frequency, however maintains

rather constant. Fig. 6.2 shows the band gap structures for 2GHz and 4GHz design where a gap of 1.2GHz and 2.5GHz can be seen.

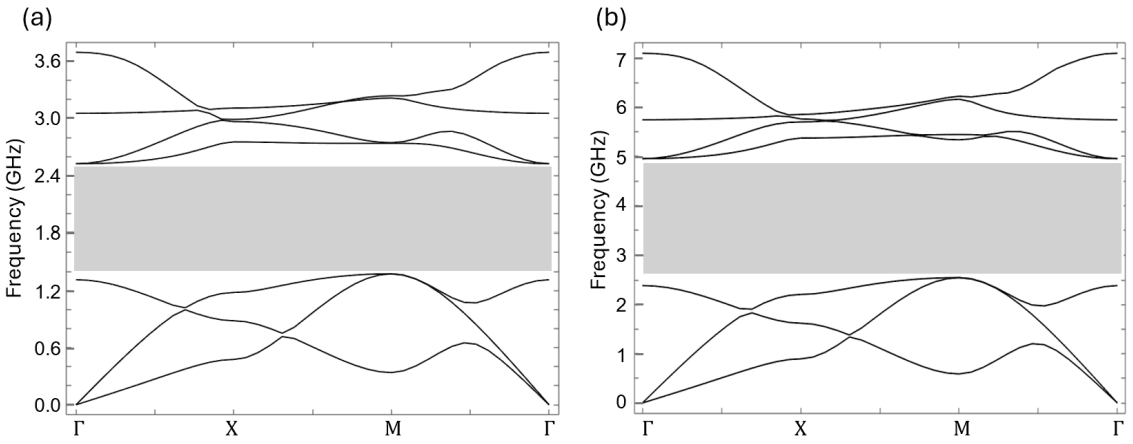

FIGURE 6.2. Band gap structures of phononic crystal designs centered around 2GHz (a) and 4GHz (b), featuring a band gap of around 1.2GHz and 2.5GHz respectively. For (a), the period of the phononic crystal is 3.7μm with dimension of the bridges in the lattice (1.2, 0.7) μm. For (b), the period of the phononic crystal is 2μm with dimension of the bridges in the lattice (0.6, 0.4) μm.

To verify theoretically that the phononic band gap can protect in-plane compression modes from propagating to the surrounding environment, we calculate with COMSOL Multiphysics on mechanical Q-factors. As is shown in Fig. 6.3 (a), this is done with the setup of perfectly matched layer (PML) around the mechanical structure to be tested. We see from (a) that the mode pattern is well constrained inside the LWR without propagating to the surrounding structures. Fig. 6.3 (b) shows the Q factors of all mechanical modes within the range of interest. All other modes show low Q-factors except one LWR mode with a theoretical Q of 10^7. Note that different from experimental results, the COMSOL simulation does not include effects of material loss including fabrication-induced surface roughness and acoustic absorption by two-level systems in the material.

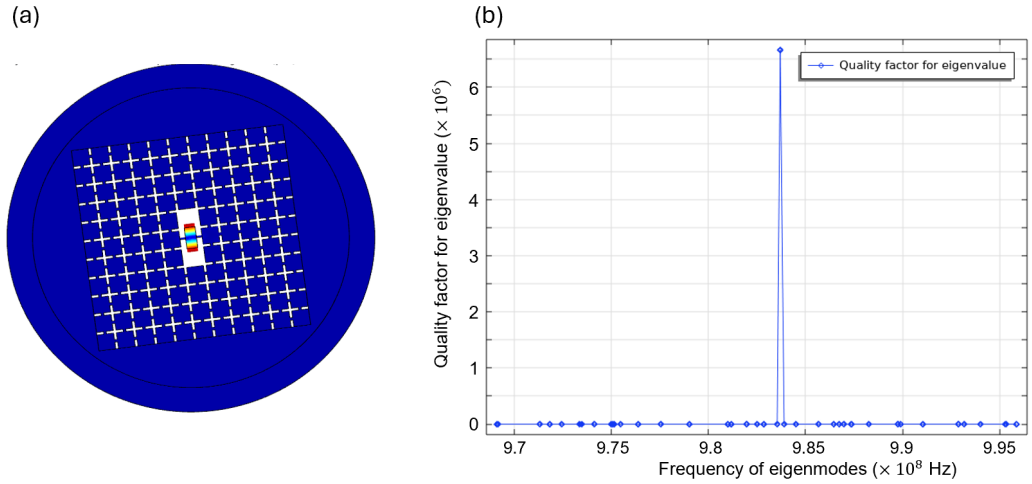

FIGURE 6.3. Perfectly matched layer and Q-factor calculations of mechanical eigenmodes. (a) Mode pattern of the first order Lamb wave resonator mode with phononic structures showing confinement of modes inside the resonator. (b) Calculated Q-factors of mechanical modes around the frequency of the Lamb wave mode. The LWR mode shows an estimated Q-factor of 6×10^6.

6.3 Device Fabrication and Patterning

The diamond phononic structure shown in Fig. 6.1(c) was fabricated from an electronic grade bulk diamond film with a thickness near 30 μm. For ion implantation, we chose ^{28}Si ions implanted about 45 nm below the diamond surface by CuttingEdge Ions. The kinetic energy and dosage of the silicon ion beam are 50 keV and $1 \times 10^9/cm^2$, respectively. Fig. 6.4 (a) to (c) shows SEM pictures of LWRs with different frequencies. Fig. 6.4(d) shows an optical image of the entire sample with six rows of patterns, frequencies are (3,3,3,2,4,1) GHz starting from the right. We dissect the pattern into $100\mu m \times 100\mu m$ blocks where the magnification for E-beam writing can be high inside each single block. This is also beneficial for recording locations of specific LWRs being worked with in the experiments by recording which

block they reside in. We use a beam current of 50pA at a voltage of 30keV and the whole pattern writing took about 7 hours until completion.

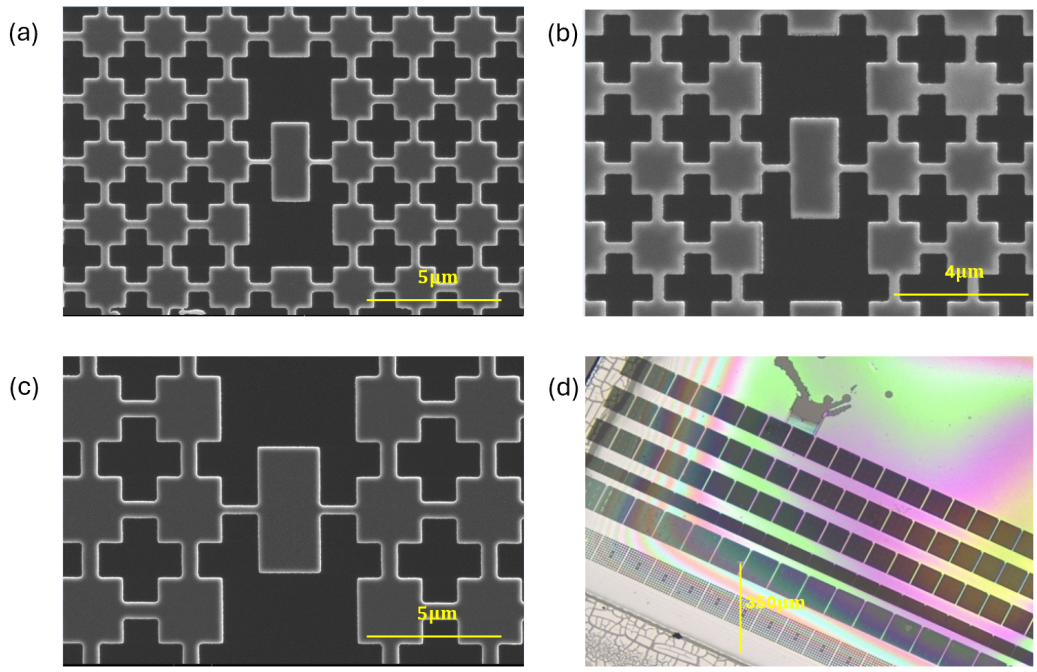

FIGURE 6.4. SEM and optical images of Lamb wave resonators fabricated at different frequencies. (a)-(c) SEM images of 4,3,2 GHz LWRs surrounded by phononic crystals. (d) Optical image of the entire sample, with six rows of LWRs featuring frequencies of (3,3,3,4,2,1) GHz from the top right.

6.4 Optical Dipole Force Driving of In-Plane Compression Mode

6.4.1 Introduction

The nearly ideal protection and isolation provided by the phononic band gap can make it difficult to excite and detect compression modes in a LWR, since unlike in a cavity optomechanical system, these modes do not couple to an optical cavity. The conventional approach of using SAWs to excite and detect mechanical vibrations in LWRs is not compatible with achieving ultrahigh Q, because of the complications of putting a SAW transducer on or near a LWR and also since by design, the phononic

band gap should shield the LWRs from the SAWs. Furthermore, while commonly used optical interferometric techniques are highly sensitive to out-of-plane mechanical displacements, these techniques are not effective for detecting the in-plane vibrations of the compression modes.

Here we solve the issue by placing the LWR in a sharply focused laser beam and use a temporally modulated optical gradient force to drive the fundamental compression mode. The induced mechanical vibrations are probed through their coupling to a SiV^- center. Resonant excitations of the fundamental compression mode by the optical gradient force can induce strong phonon sidebands in the SiV^- optical excitation spectrum. Mechanical vibrations with an amplitude as small as a picometer can then be detected through the sideband optical transitions. Sideband optical interferometry, instead of conventional optical interferometry, can also be used for the detection of the in-plane vibrations of the compression modes.

6.4.2 Theory

The LWR with a thickness of d is placed at the waist of a sharply focused 1550 nm laser beam, with the laser beam normal to the LWR surface, as shown schematically in Fig. 6.5(a). The focused laser beam exerts two types of mechanical forces on the LWR: a radiation pressure force that scales with the total incident laser power and a gradient force that scales with the gradient of the electric field amplitude. The radiation pressure force is normal to the LWR surface and is thus not effective in exciting compression mechanical modes. In comparison, at the waist of the laser beam, the gradient force, which is widely used in optical dipole traps, points to the center of the laser beam, as illustrated in Fig. 6.5(a). By modulating the intensity

of the laser beam at the mechanical resonance frequency, we can resonantly excite the compression vibration of the LWR via the gradient force.

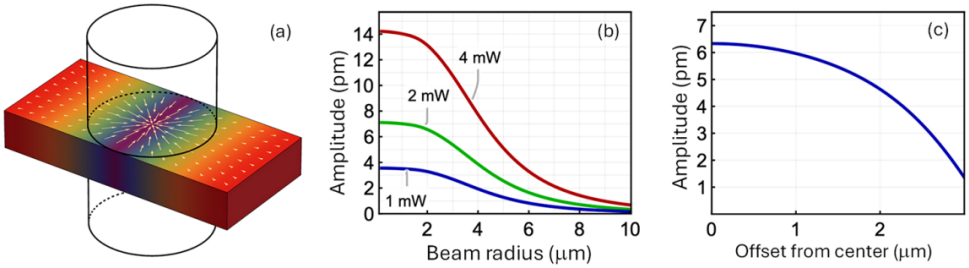

FIGURE 6.5. (a) Schematic illustrating a LWR placed at the waist of a laser beam. The arrows illustrate the directions of the gradient force. (b) Calculated amplitude of the induced mechanical vibration as a function of the laser beam radius, with the incident laser power indicated in the figure. (c) The vibration amplitude decreases as the laser beam, with a power of 2 mW and a radius of 2.25 μm, is offset from the center of the LWR.

In the limit that d is small compared with the depth-of-focus of the laser beam, the areal density of the gradient force in the dipole approximation is given by

$$\mathbf{f}_a(x,y) = \nabla[\mathbf{p}(\mathbf{r}) \cdot \mathbf{E}(\mathbf{r})] \tag{6.1}$$

where $\mathbf{E}(\mathbf{r})$ is the electric field and $\mathbf{p}(\mathbf{r})$ is the areal density of the induced electric dipoles. For the fundamental compression mode propagating along the x-direction with a mode pattern $\phi(x)$ (see Fig. 6.5(a)), we can decompose $\mathbf{f}_a$ into a component $\mathbf{f}_m = F\phi(x)\hat{\mathbf{x}}$, which is matched to $\phi(x)$, and a remainder, which is orthogonal to $\phi(x)$, where $F = \int dxdy\phi(x)\hat{\mathbf{x}} \cdot \mathbf{f}_a(x,y)$ is the amplitude and $\hat{\mathbf{x}}$ is the unit vector in the x direction.

For a 1550 nm laser with an intensity-modulation frequency, ω, resonant or nearly resonant with the fundamental compression mode, the steady-state mechanical

vibration can be written as $u(x,t) = u_w\phi(x)exp(-iwt) + c.c.$, with

$$u_w = \frac{F}{\rho_a}\frac{1}{\omega_m^2 - \omega^2 - i\omega\gamma_m} \tag{6.2}$$

where ρ_a is the areal mass density and $\omega_m = 2\pi f_m$. For a theoretical estimate, we consider a diamond LWR with dimension (9.5, 4.5) μm and $\gamma_m/2\pi$= 83 Hz and with corrections to both external and internal optical reflections of the LWR. To be consistent with experiments, an intensity-modulation depth of 80% is used. Fig. 6.5(b) plots the calculated amplitude of the induced vibration as a function of the laser beam radius. An amplitude of a few P_m can be induced with an incident laser power of a few mW and with a beam radius near 2 μm. As shown in Fig. 6.5(c), the induced amplitude decreases gradually as the laser beam is offset from the center of the LWR.

6.4.3 Experimental Setup

The diamond Lamb wave resonator (LWR) sample is mounted on a cold-finger closed cycle cryostat (Montana Instruments Cryostation S50) and kept near 7 K. A 532 nm diode laser (Laserglow Technologies) is used for the initialization of the silicon vacancy (SiV^-) center. A tunable diode laser with a wavelength near 737 nm (Toptica DL pro) is used for the resonant excitation of the SiV^- center. For the sideband optical interference experiment, an electro-optic modulator (EOM) from Jenoptic is used to generate the two optical fields needed to drive the carrier and the first red sideband transitions. For the resonant excitation of the fundamental compressional mode in the LWR, a 1550 nm laser is intensity-modulated with an EOM from Thorlabs (LN81S-FC). The intensity-modulated laser is then amplified in

a fiber optical amplifier (Amonics AEDFA-33-B-FA). The output from the amplifier features an intensity modulation with a depth of 80%.

All three laser beams, including the 1550 nm, 532 nm, and 737 nm lasers, are focused onto the sample with a 100× objective (Nikon L Plan 0.85 NA) mounted outside of the cryostat. Fluorescence from the SiV^- is collected by the 100× objective and then coupled into a 10 μm diameter optical fiber. An avalanche photodiode (Perkin-Elmer SPCM-AQR-16-FC) is used for photon counting. A pulse generator (SpinCore) provides electrical pulses that gate the acousto-optic modulators (AOMs) and synchronize the optical pulses needed for the experiments. The pulse sequence used for photoluminescence excitation (PLE) experiments and mechanical excitation, along with the experimental setup is shown in Fig. 6.6. The 1550 nm laser was positioned at the center of the resonator, while the 532 nm and 737 nm lasers were centered at a SiV^- center. The powers of the lasers were measured after the 100× objective.

The beam radius of the 1550 nm laser on the sample as measured by an infrared camera, is 2.3 μm. The image is processed in Python and the dimensions are calibrated with the size of the Lamb wave resonator. Fig. 6.7 (b) shows a Gaussian fit to the laser spot brightness by integrating along the y-direction in Fig. 6.7 (a).

6.5 Strain Coupling with SiV^- Centers in Diamond

The excitation of a longitudinal-acoustic phonon mode in diamond leads to local variations in the lattice constant, which induces a periodic change in the energy gap and a corresponding shift in the energy separation between a ground state, $|g\rangle$, and an excited state, $|e\rangle$ of the SiV^- center, with the electron-phonon interaction

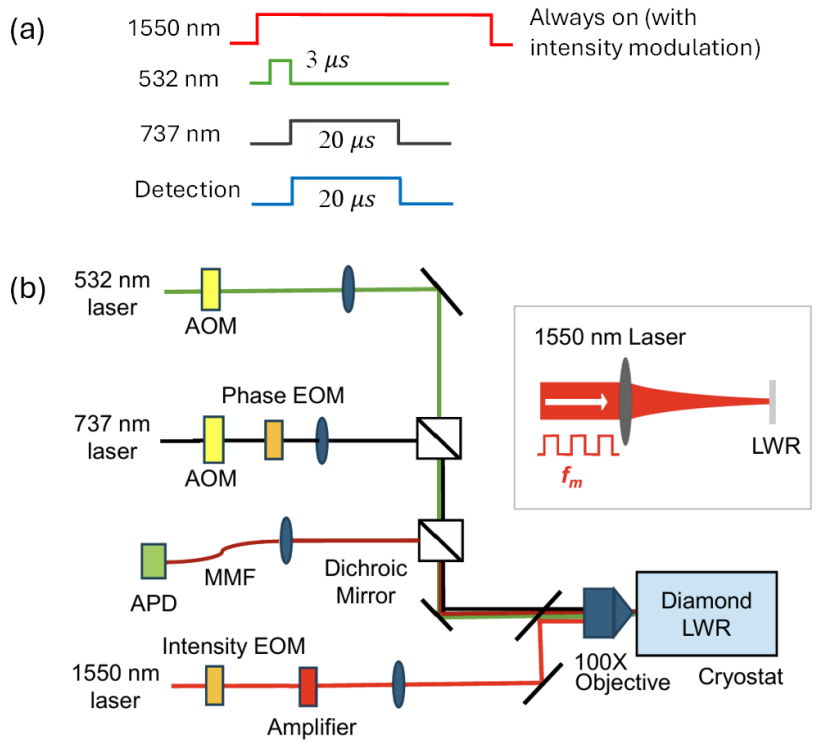

FIGURE 6.6. (a) Pulse sequence for the PLE experiment. A 532 nm laser pulse initializes the SiV^- center, which is followed by a 737 nm laser pulse to excite the SiV^- center. The intensity-modulated 1550 nm laser is always on. (b) Schematic of the experimental setup used for exciting and detecting compression mechanical modes.

Hamiltonian given by

$$V = i\hbar G(\hat{b} - \hat{b}^+)|e\rangle\langle e| \tag{6.3}$$

where $G = Dk_m x_{zpf}$ is the effective electron-phonon coupling rate, with D being the deformation potential and k_m being the wave number of the mechanical mode,$\hat{b}^+$ and $\hat{b}$ are the creation and annihilation operators for the mechanical oscillator, and $x_{zpf} = \sqrt{\hbar/2m_{eff}\omega_m}$ is the zero-point fluctuation. For a dipole optical transition between $|g\rangle$ and $|e\rangle$, the above Hamiltonian leads to sideband optical transitions induced by absorption or emission of the phonons, as illustrated in Fig. 6.8(a). With a laser field at the red sideband of the optical transition, the effective interaction

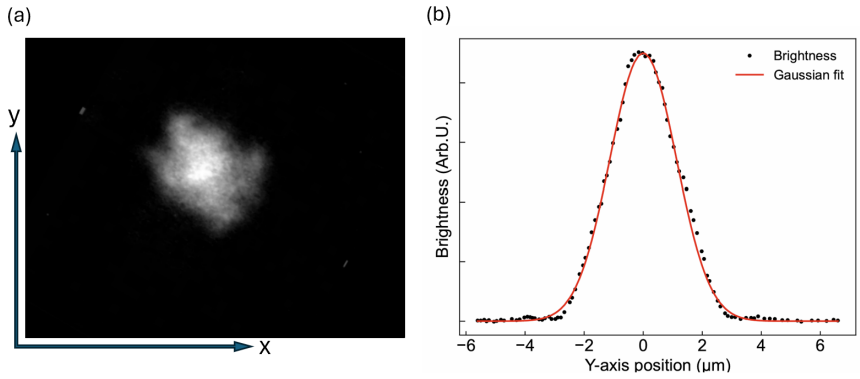

FIGURE 6.7. Beam profile of 1550nm laser on the Lamb wave resonator. (a) CCD image captured on an infrared camera with a USB converter into the OBS Studio software. (b) A gaussian fit to the brightness integrated along the y direction in (a).

Hamiltonian for the first red sideband transition is given by [40],

$$V_r = \frac{\hbar G \Omega_0}{2\omega_m}(\hat{b}|e\rangle\langle g| + \hat{b}^+|g\rangle\langle e|) \tag{6.4}$$

where Ω_0 is the Rabi frequency for the direct dipole transition, i.e., the carrier transition. The Rabi frequency for the first red sideband transition is thus $\Omega_1 = \Omega_0 G\sqrt{n}/\omega_m$, where n is the average phonon occupation of the mechanical mode. The first blue sideband transition is described by a similar Hamiltonian.

Fig. 6.8(b) shows the SiV^- energy level structure and optical selection rules. Experimental studies presented in this chapter were carried out on the C-transition and with a 737 nm laser power of 0.17 μW, unless otherwise specified. The experiments employed a SiV^- center slightly offset from the center of the resonator, with the SiV^- position indicated in a confocal fluorescence microscopy image of the LWR shown in Fig. 6.8(c). The PLE spectrum of the SiV^- center features a linewidth of 310 MHz (see Fig. 6.8(d)), compared to the radiative-lifetime limited linewidth near 100 MHz. The additional line broadening is in large part due to the power broadening induced by the 737 nm laser. With the application of a 5 mW

continuous wave (CW) 1550 nm laser, the PLE linewidth broadens to 460 MHz. More detailed studies on line broadening induced by the 1550 nm laser are discussed in Appendix. A.

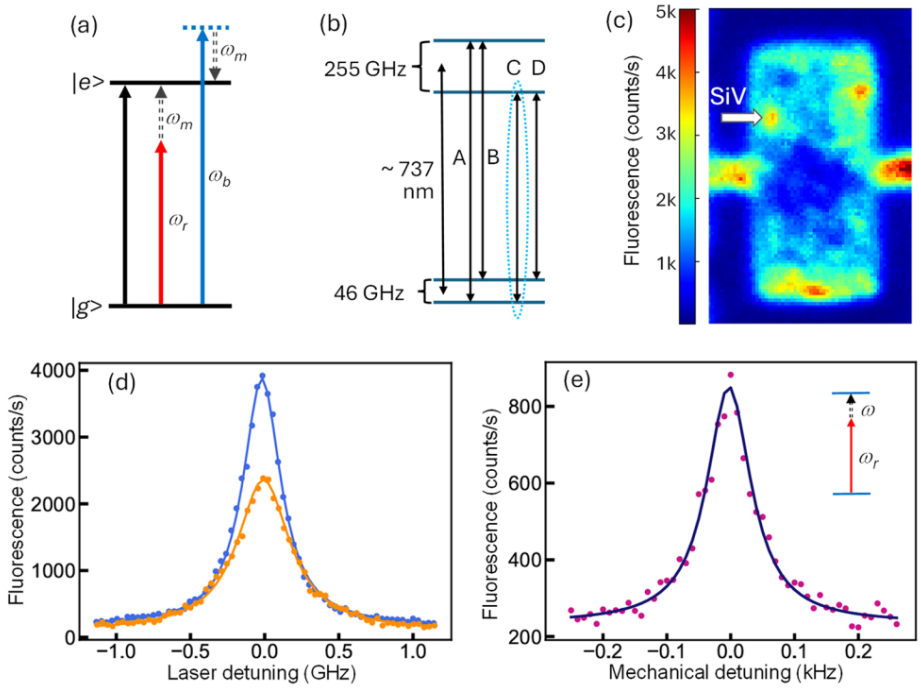

FIGURE 6.8. (a) Schematic illustrating the first red and blue sideband transition due to the absorption and emission of a phonon, respectively. (b) Energy level structure and optical selection rules for SiV^-. (c) A confocal fluorescence microscopy image of the LWR indicating the SiV^- used for the experiment. The image was taken with an excitation laser resonant with the SiV^-. (d) PLE spectra for the SiV^- C-transition with (orange dots) and without (blue dots) the application of a CW 1550 nm laser. (e) Detection of the mechanical resonance via the first red sideband, for which SiV^- fluorescence is measured as a function of the detuning between the mechanical resonance and the intensity-modulation frequency of the temporally modulated 1550 nm laser, with the 737 nm laser fixed at nearly 1 GHz below the optical resonance. Solid lines in (d) and (e) are the least-square fits to a Lorentzian.

6.5.1 Direct Phonon Sideband Coupling with SiV^- Centers

In the resolved sideband regime with $\omega_m > \gamma$, where γ is the linewidth for the optical transition, the phonon sidebands are spectrally resolved in the excitation

spectrum of the two-level system. For the detection of the compression mechanical vibration via the first red sideband, the SiV^- center is subject to an optical field with a frequency fixed at nearly 1 GHz below the optical resonance (i.e., at the red sideband), while the compression mode in the LWR is excited by a temporally modulated 1550 nm laser beam with an average power of 2 mW. Fig. 6.8(e) shows the fluorescence from the SiV^- center as a function of the intensity-modulation frequency. In this case, the resonant excitation of the compression mode leads to the excitation of the SiV^- center via the phonon-assisted transition. The mechanical resonance observed in Fig. 6.8(e) occurs at f_m =0.977 GHz and features $\gamma_m/2\pi$ =83 kHz, corresponding to Q=1.2×10^7.

6.5.1.1 Searching of Mechanical Resonance. A major challenge in our early experimental efforts was to find the fundamental compressional mode in a LWR. While the frequency of the mechanical mode can be calculated, the uncertainty in the parameters used limits the accuracy of the theoretical prediction. It was thus necessary to scan an adequate frequency range in order to locate the fundamental compressional mode. For a GHz resonator, a 1% error in predicting the resonance frequency will require a scan range of 20MHz. Fig. 6.9 shows the result of our first successful scan, with a frequency scan range near 20MHz. The entire scan (with 100 MHz in total scan range) took about 28 hours, with each data point taking about 1 second. For a fixed total scan time, the scan range inversely scale with the step size. For the scan in Fig. 6.9, we made a guess that the Q-factor is of order 10^6 and thus chose a step size of 1 kHz. We would have missed the mechanical resonance if a significantly greater step size were to be chosen. We would have also missed the mechanical resonance if we had chosen a much smaller step size and thus smaller scan range, while keeping the total scan time fixed.

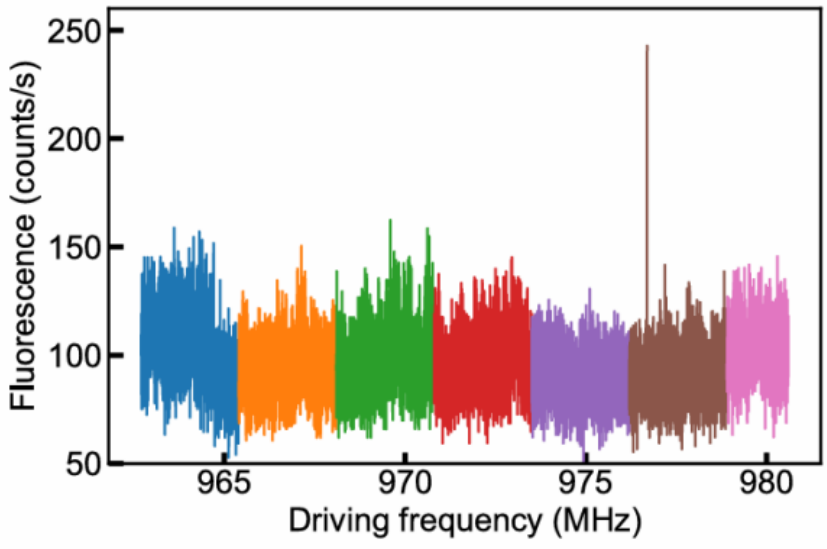

FIGURE 6.9. SiV^- Fluorescence as a function of the intensity-modulation frequency of the 1550 nm laser. The SiV^- is driven by a 737 nm laser at the red sideband and by the mechanical vibration induced by the intensity-modulated 1550 nm laser.

Another major issue we showed briefly is the quenching and broadening of SiV^- centers fluorescence by the 1550nm laser. Since the searching of mechanical modes depends strongly on the signal-to-noise ratio of the system, which is essentially the brightness of the SiV^-, it is crucial to minimize the quenching effects of telecom laser on SiV^- centers. One way to mitigate this is to adjust the position of the 1550nm laser slightly off the SiV^- by walking the mirrors. This could be tricky since the 1550nm CCD camera is not sensitive to visible light and therefore hard to show specific locations of the beam. Walking the mirrors by too much will possibly cause the beam to wander off the resonator unknowingly. Another way to mitigate the quenching effect is to use ringdown measurements of 1550nm. We switch the laser on for a time τ, during which oscillations of lamb wave modes build up. Then we switch off the 1550nm and turn on the PLE pulse sequence for the SiV^- for a time window τ_2, during which strain coupling happens through phonon sideband

transitions of SiV^-. The on-and-off status of 1550nm laser is controlled by an AOM (IntraAction FM-40). From an estimation of 10^6 Q-factor and 1GHz frequency mode, lifetime of LWR mode is about 300μs. Fig. 6.10 (a) shows the pulse sequence for the ring-down measurement. We found that with ring-down measurements, PLE spectra of SiV^- under high power telecom laser is almost as good as the spectra without any telecom lasers. Fig. 6.10 (b) shows a spectrum scan of the mechanical mode under ring-down measurement. There're three or more peaks appearing with frequency separations at a few kHz. This is due to the extra frequency component of 8 kHz brought by the ringdown pulse sequence.

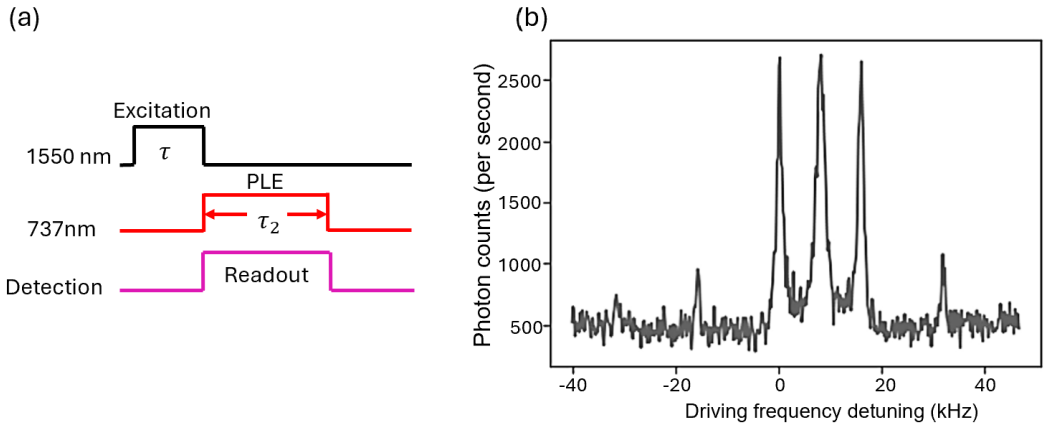

FIGURE 6.10. Mechanical Q-factor measurement and spectrum scan with the 1550nm driving laser turned off during the measurement window (ring-down). (a) Pulse sequence for the ring-down process including driving of mechanical modes and PLE measurements. (b) A spectrum scan showing two extra sidebands owing to the recurring frequency of ring-down pulses.

6.5.1.2 Sidebands in PLE spectra: Theory and Data. For a detailed study of the phonon sidebands in the SiV^- optical excitation spectra, we measure the PLE spectra of the SiV^- center, while fixing the intensity-modulation frequency of the 1550 nm laser at the observed mechanical resonance. Fig. 6.11 shows the

PLE spectra obtained with increasing average power, P_m, for the 1550 nm laser. At relatively small P_m, only the first sidebands are observed in the PLE spectra. Higher order phonon sidebands emerge at relatively high P_m, indicating the relatively strong excitation of the compression mechanical mode by the optical gradient force. The amplitude of the first sideband increases initially with P_m, corresponding to increased mechanical excitations, and then starts to saturate. This saturation is primarily due to the excitation of second and higher order phonon sidebands. As expected, the increase in the sideband contribution in PLE spectra is accompanied by a decrease in the amplitude of the carrier resonance.

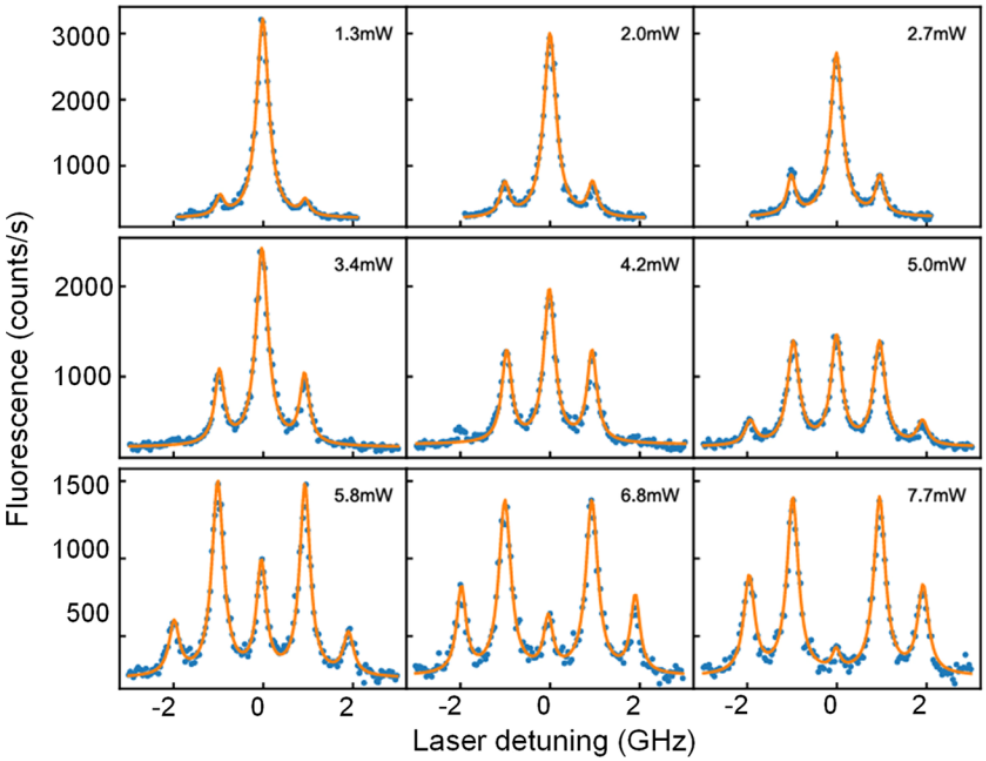

FIGURE 6.11. Phonon sidebands in PLE spectra induced by the excitation of the fundamental compression mode. The intensity-modulation frequency for the 1550 nm laser is fixed at the mechanical resonance. The 1550 nm laser power used is indicated in the figure. The solid lines are the least-square numerical fits to multiple Lorentzians.

The relative amplitudes of the carrier and the sideband transitions can be qualitatively understood without including the line broadening induced by the 1550 nm laser. In the limit of weak optical excitation and with the optical sideband transitions described by Hamiltonian, $V = i\hbar G(\hat{b} - \hat{b}^{+})|e\rangle\langle e|$, the excited state population for a laser field with frequency ω_L is given by [33]

$$\rho_{ee}(\omega_L) \propto \sum_{n=-\infty}^{+\infty} \frac{J_n^2(B)}{(\omega_L - \omega_0 - n\omega_m)^2 + (\gamma/2)^2} \tag{6.5}$$

where ω_0 is the resonance frequency of the two-level optical transition, J_n is the Bessel function of the first kind, $B = D \cdot cos(\pi x/L) \cdot A_m/v$ is a dimensionless parameter, with v being the acoustic velocity, L being the length of the LWR, x being the SiV^- offset from the center of the LWR, and $A_m = 2x_{zpf}\sqrt{n}$ being the classical amplitude of the mechanical vibration. The $cos(\pi x/L)$ term accounts for the strain profile across the LWR. As shown in Eq. 5, the relative amplitudes of the carrier and the sideband transitions are determined by $J_n^2(B)$. Fig. 6.12 plots the calculated excitation spectra with increasing B, which are in qualitative agreement with the observed PLE spectra shown in Fig. 6.11. A quantitative description of the PLE spectra will require a detailed understanding of the effects of 1550 nm laser on the SiV^- transition.

6.5.1.3 Estimation of Vibration Displacement . As discussed above, the amplitude of the mechanical vibration is determined by $A_m = 2(\Omega_1/\Omega_0)v/D$, when the SiV^- is at the center of the resonator. For a SiV^- that is offset by x from the center, the amplitude is given by $A_m = 2(\Omega_1/\Omega_0)v/[D \cdot cos(\pi x/L)]$, where L is the resonator length. The $cos(\pi x/L)$term accounts for the strain profile across the sample.

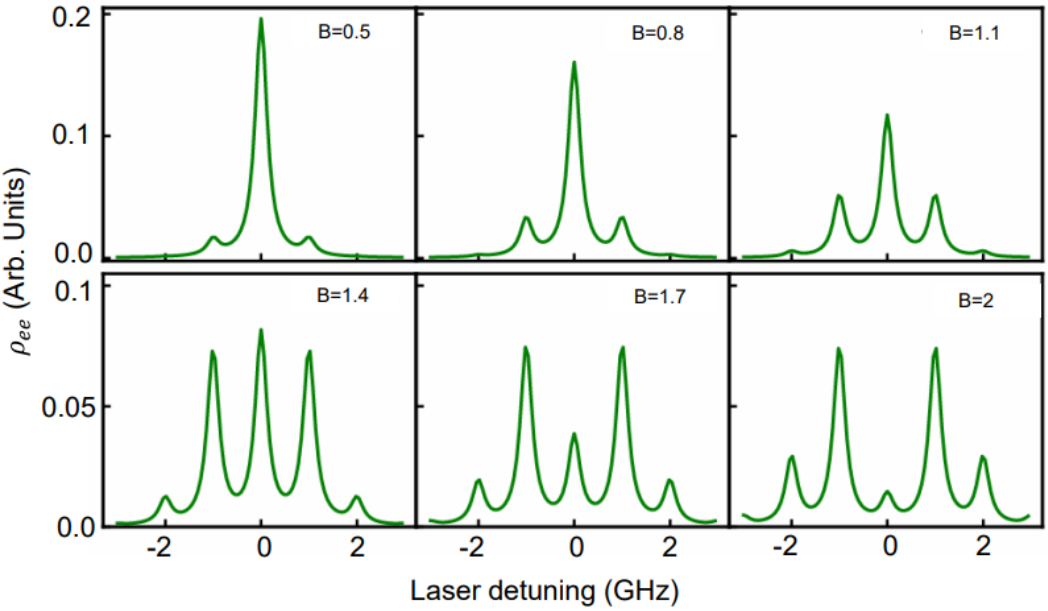

FIGURE 6.12. Calculated optical excitation spectra with increasing amplitude for the fundamental compression mode. B is a dimensionless parameter characterizing the mechanical amplitude. The calculation assumes a weak optical excitation, with the excited state population $\rho_{ee} \ll 1$ and with $\gamma/2\pi$=300 MHz.

With significant power broadening induced by the 737 nm laser, $(\Omega_0/\Omega_1)^2$ is no longer the ratio of the spectrally integrated areas for the carrier resonance and the first red sideband resonance in the corresponding PLE spectrum. For the first sideband resonance in the PLE spectrum shown in Fig. 6.11, the power broadening due to the 737 nm laser is nearly negligible, since the Rabi frequency for the sideband transition is still relatively small. In this case, we take the linewidth obtained from the first sideband resonance for the carrier resonance. In this limit, we have

$$(\Omega_1/\Omega_0)^2 = \frac{A_s}{A_c}\frac{\gamma_s^2}{\gamma_c^2} \tag{6.6}$$

where A_c and A_s are the respective amplitudes for the carrier and sideband resonance in the PLE spectrum, and γ_C and γ_s are the respective linewidth. The

estimate of the vibration amplitude given earlier has included the offset of the SiV^- from the center of the LWR and the power broadening of the carrier resonance discussed above. In the limit of weak mechanical excitation, the ratio of the Rabi frequency, Ω_1/Ω_0, directly measures the amplitude of the mechanical vibration. From Eq. 4, the classical amplitude of the mechanical vibration is given by,

$$A_m = 2(\Omega_1/\Omega_0)v/D \tag{6.7}$$

for which the SiV^- is assumed to be at the center of the resonator. Without power broadening, $(\Omega_0/\Omega_1)^2$ equals the ratio of the spectrally integrated areas for the carrier resonance and the first red sideband resonance in the corresponding PLE spectrum. Using the PLE spectrum with P_m= 2 mW in Fig. 6.11 and including effects of power broadening in the carrier transition as well as offset of the SiV^- center from the center of the resonator, we estimate that Ω_0/Ω_1 is near 3. The amplitude of the induced mechanical oscillation is then estimated to be 3×10^{-12} m, for which $v = 1.9 \times 10^4 m/s$ and $D/2\pi = 10^{15}$ Hz are used [58]. The experimental result is in general agreement with the theoretical expectation. Overall, the sideband transitions can serve as an effective probe for compression vibrations with an amplitude as small as a picometer.

6.5.2 Sideband Interferometry with SiV^- Centers

As illustrated in Fig. 6.13(a), both the carrier transition and the red sideband transition can excite the two-level system from $|g\rangle$ to $|e\rangle$. Optical emissions from the excited state depend on the relative phase of the two corresponding transition amplitudes. Compression mechanical vibrations can thus be detected through the

interference between these two transition pathways, i.e., through sideband optical interferometry. For sideband optical interferometry, a phase EOM was used for the generation of the two needed optical fields with a fixed relative phase.

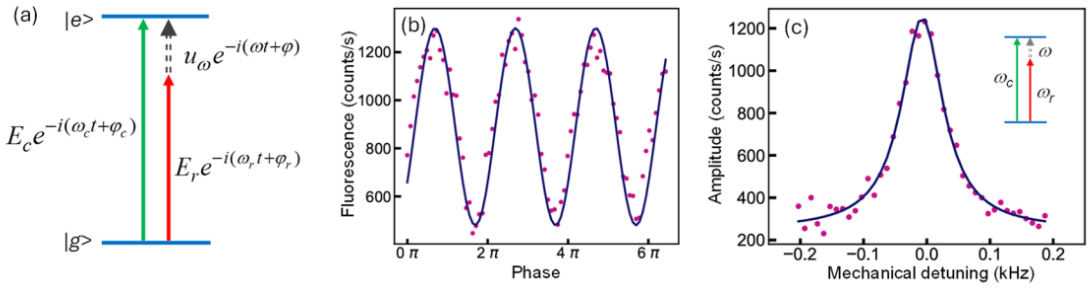

FIGURE 6.13. (a) Schematic illustrating the interference between the direct dipole transition and the first red sideband transition. (b) Fluorescence from the SiV^- center as function of φ, the phase of the intensity modulation, with P_m=2.7 mW and $\omega/2\pi$= 0.977 GHz, showing interference fringes. The solid line is a numerical fit to a sinusoidal with a period of 2π. (c) The oscillation amplitude derived from the interference fringes as a function of the detuning from the mechanical resonance. The solid line is a least-square fit to a Lorentzian.

For the implementation of the sideband optical interferometry, the gradient force generated by an intensity-modulated 1550 nm laser beam, with a power P_m and a modulation frequency ω, excites the fundamental compression mode of the LWR. The SiV^- center is driven by two optical fields with frequency ω_c and ω_r, respectively (see Fig. 6.13(a)). These two fields feature a fixed relative phase and a detuning set to ω_c-ω_r=ω, for which ω_c is near the optical resonance. Fluorescence from the SiV^- center is measured as a function of φ, the phase of the intensity modulation. The resulting sideband optical interference fringes shown in Fig. 6.13(b) demonstrate the coherent excitation of the compression mechanical mode in the LWR. Fig. 6.13(c) plots the amplitude derived from the respective interference fringes as a function of the intensity-modulation frequency. The sharp mechanical resonance observed features f_m =0.977 GHz and $\gamma_m/2\pi$ =80 Hz, in good agreement with those obtained

from the excitation of the SiV^- center through only the first sideband transition shown in Fig. 6.8(e).

It should be noted that sideband optical interferometry does not require that the sideband transition is spectrally resolved from the carrier transition. The interferometry should thus function well even when the spin-mechanical system is not in the resolved sideband regime. In this regard, the sideband interferometry provides a general and powerful experimental approach for detecting and characterizing in-plane mechanical vibrations in spin-mechanical systems, for which conventional optical interferometry is not effective.

6.6 Estimation of Spin-Mechanical Cooperativity

Ultracoherent diamond LWRs are especially suitable for phononic cavity QED of electron spins. For a SiV^- center, direct acoustic transitions between spin states are allowed by the mixing of the spin states induced by an off-axis magnetic field [58]. The single-phonon spin-mechanical coupling rate is thus

$$g = \eta D k_m x_{zpf} \tag{6.8}$$

where η is the effective mixing ratio. As discussed earlier, the cooperativity for the phononic cavity QED system is given by $C = 4g^2/(\gamma_m \gamma_s)$. For a numerical estimate, we write the cooperativity in terms of the relevant SiV^-, material, and resonator parameters,

$$C = \frac{2\hbar(\eta D)^2}{v^2 \gamma_s} \cdot \frac{Q}{m_{eff}} \tag{6.9}$$

with all parameters defined earlier. Note that C does not depend directly on the mechanical resonance frequency. For a LWR with dimensions (9.5, 4.5, 1.5)μm, m_{eff} =125 picogram as calculated by the COMSOL program. For a Q-factor of 10^7, an η of 0.2 and a $\gamma_s/2\pi$ of 1MHz, C is estimated to exceed 10.

6.7 Conclusion

In conclusion, we have demonstrated the use of optical gradient force to drive compression mechanical modes in a diamond LWR. The induced vibrations couple to a SiV^- center through deformation potential, leading to strong phonon sidebands in the SiV^- optical excitation spectrum. The in-plane vibrations of the compression modes can be effectively detected through the sideband optical transitions as well as sideband optical interferometry. We show that GHz diamond LWRs protected by a phononic band gap can feature a Q-factor exceeding 10^7, enabling an experimental platform for quantum spin-mechanics, especially for phononic cavity QED of electron spins. Ultracoherent GHz LWRs can also be extended to other material systems such as silicon carbide that hosts suitable spin qubits [94]. In addition, spin-mechanical LWRs can be coupled together via phononic waveguides, forming a mechanical quantum network and providing a promising platform for spin-based quantum computers [95].

CHAPTER VII

STRONGLY DRIVEN SPIN-MECHANICAL SYSTEMS

This work was done in collaboration with Hailin Wang and has been published in Physical Review Applied as Ref. [45]. Hailin designed, supervised the research project, analyzed the results and prepared the manuscript. I performed the fabrication and characterization of the sample and conducted the experiment.

7.1 Introduction

In this chapter we discuss our experimental studies of a strongly driven spin-mechanical system in the unresolved sideband regime. For spin-mechanical systems that feature phonon-assisted (i.e., sideband) transitions, earlier experimental studies have emphasized the resolved-sideband regime, for which the mechanical frequency is large compared with the transition linewidth, since this regime is desirable for cooling and amplification of mechanical motion via spin-mechanical coupling [42, 96]. For our system, a nitrogen vacancy (NV^-) center in a diamond cantilever couples to out-of-plane modes of the cantilever via the deformation potential of the NV^- excited states and through the sideband optical transitions. Photoluminescence excitation (PLE) studies of the NV^- center show that under a strong external driving of the mechanical mode, the excitation spectra from a NV^- optical transition feature two spectrally sharp peaks with a large strain-induced frequency separation [97], in contrast to the multiple sidebands observed in earlier experimental studies in the resolved sideband regime [10, 33].

7.2 Device and Experimental Setup

Devices discussed in this chapter are based on the diamond cantilevers used in Chapter V, with a width of 4 μm, length near 15 μm, and a thickness near 2.5 μm. The cantilevers are embedded in a square phononic crystal lattice, as shown in Fig. 7.1(a). A phononic band gap protects the fundamental out-of-plane mode of the cantilevers from its surrounding environment, and the NV^- centers are created about 100 nm below the diamond surface with ion implantation.

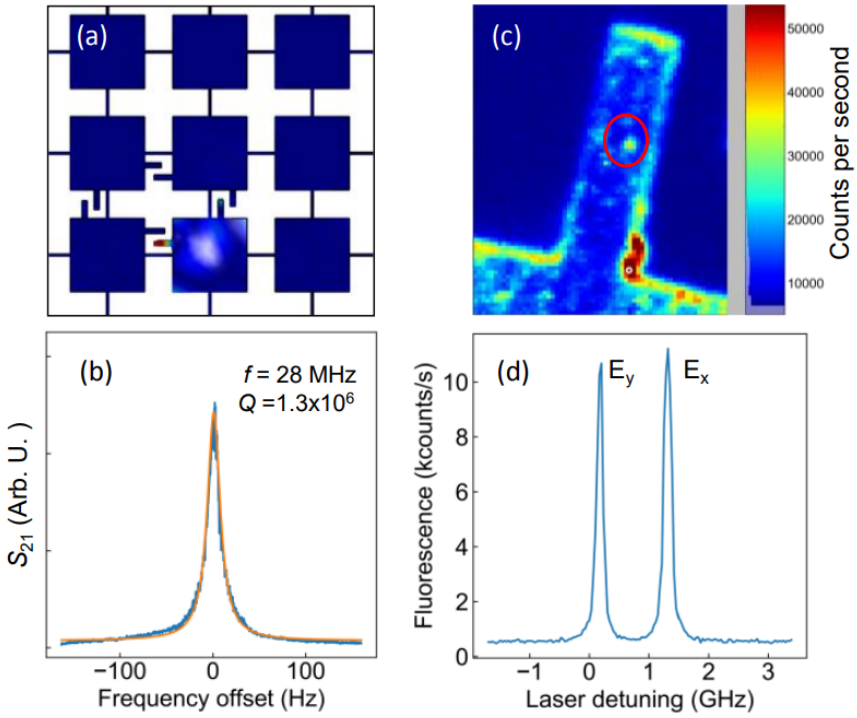

FIGURE 7.1. (a) Simulated displacement pattern of diamond cantilevers embedded in a square phononic crystal lattice with a period of 76 μm. (b) Spectral response of the fundamental out-of-plane mode of the cantilever used. (c) Confocal optical image of the cantilever. The red circle highlights the NV^- center used in the PLE study. (d) PLE spectrum of the NV^- center. The two ZPLs correspond to optical transitions from the $|m_s = 0\rangle$ ground state to the E_x and E_y excited states.

The fundamental out-of-plane mode of the cantilever has a frequency, $\omega_m/2\pi$=28 MHz, and a linewidth, $\gamma_m/2\pi$=22 Hz, corresponding to a Q-factor, Q=1.3 $\times$ 10^6 (see Fig. 7.1(b)). PLE studies were carried out in a NV^- center near the middle of the cantilever, as shown in the confocal optical image in Fig. 7.1(c). The PLE spectrum of the NV^- center obtained at T=8 K and in the absence of external mechanical driving is characterized by two ZPLs, corresponding to the transitions from the $|m_s = 0\rangle$ ground state to the E_x and E_y excited states (see Fig. 7.1(d)). The ZPLs feature a spectral linewidth near 100 MHz, indicating the high optical quality of the NV^- center, though the spin-mechanical coupling via the sideband optical transitions is in the unresolved sideband regime.

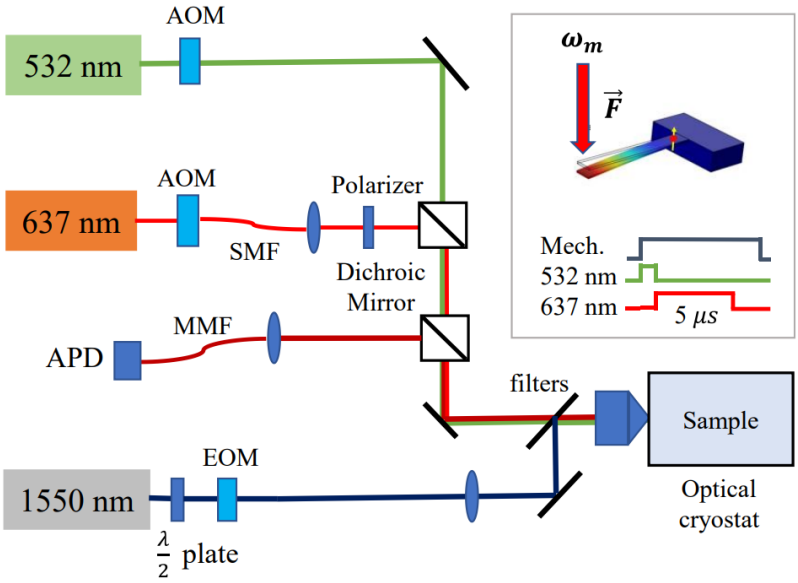

FIGURE 7.2. Schematic of the experimental setup. AOM: Acousto-optic modulator. APD: Avalanche photodiode. MMF: Multimode fiber. SMF: Single mode fiber. The inset illustrates a schematic of resonantly driving the vibrations of the cantilever with radiation pressure force and shows the pulse sequence for the PLE experiment.

Fig. 7.2 shows a schematic of the experimental setup, which is based on a home-built low-temperature scanning confocal microscope. The thin diamond phononic

structure is glued to a bulk diamond plate mounted on the cold finger of an optical cryostat (Montana Instrument S50). All experimental results presented in this paper were obtained at T=8 K unless otherwise specified. For the PLE experiment, a green laser pulse (λ=532 nm) initializes the NV^- center into the $|m_s = 0\rangle$ ground state. A tunable diode laser (New Focus Velocity TLB-6712) near 637.2 nm excites the NV^- center. To avoid the power broadening of the ZPL, the red laser power is kept below 1 μW. NV^- fluorescence with $\lambda > 645$ nm is collected with a 100$\times$ objective (Nikon L Plan 0.85 NA) and then coupled into an optical fiber connecting to an avalanche photodiode (APD) for single-photon counting. A pulse sequence of the PLE experiment is shown in the inset of Fig. 7.2.

To resonantly drive the mechanical modes of the cantilever, we use radiation pressure force from a focused laser beam with λ=1.55 μm, for which the intensity of the laser beam is sinusoidally modulated with an electro-optical modulator (EOM). An additional lens is also used such that the 1.55 μm laser beam can be focused onto the cantilever surface along with the green and red laser beams. Within the range of the laser power used (<50 mW), no ZPL broadening due to sample heating induced by the 1.55 μm laser has been observed. Note that optical powers given in the paper were measured before the 100$\times$ objective in the setup.

7.3 Photoluminescence Excitation of a Driven Spin-Mechanical System

To investigate the coupling between the NV^- center and the driven mechanical vibration, we measure the PLE spectra of the NV^- center, while resonantly driving the fundamental out-of-plane mode. As shown in Fig. 7.3(a), at relatively weak mechanical driving, a broadening of the E_y resonance is observed, which is expected

since the spin-mechanical system is in the unresolved band regime. With increasing mechanical driving, two peaks appear in the PLE spectra of the E_y transition (see Fig. 7.3(b)). Similar behaviors have also been observed in an earlier study [97], as well as for the E_x transition (not shown). The frequency separation between the two peaks is linearly proportional to the amplitude of the driving force, in this case, the average power of the 1.55μm laser beam (see Fig. 7.3(c)). Overall, the excitation spectra of the spin-mechanical system in the unresolved sideband regime differ qualitatively from those observed in the resolved sideband regime, which are characterized by distinct sideband resonances corresponding to emission or absorption of integer numbers of phonons [10].

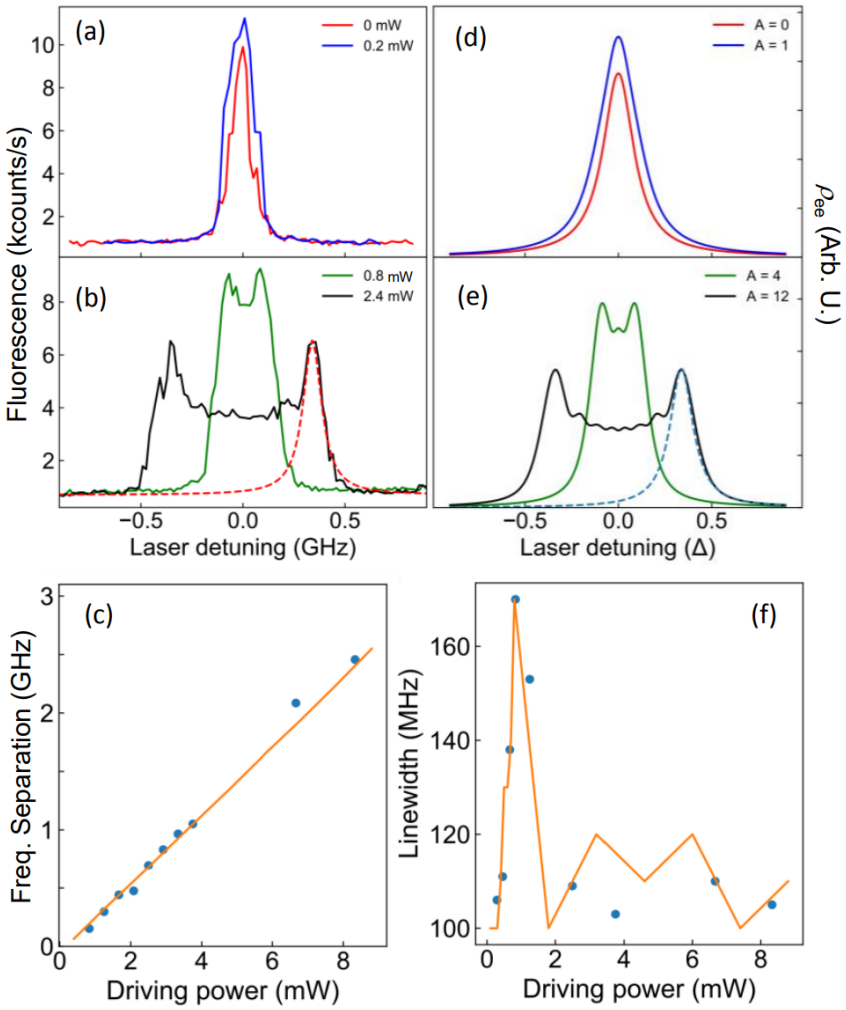

FIGURE 7.3. (a) and (b) PLE spectra of the NV^- center under resonant mechanical driving, with the 1.55 μm laser power indicated in the figure. (c) Frequency separations of the two peaks in PLE spectra as a function of the mechanical driving power. (d) and (e) Theoretically calculated PLE spectra as discussed in the text. The dashed line is a Lorentzian fit to the steep side of the peak. (f) Spectral linewidth of the PLE peaks versus the mechanical driving power. The solid lines in (c) and (f) are derived from the theoretically calculated PLE spectra, for which a conversion factor of 0.2 mW laser power corresponding to A=1 is used.

To understand the excitation spectrum of the driven mechanical system in the unresolved sideband regime, we model the NV^- center as a two-level system, which couples to the long wavelength mechanical vibration through the excited-state

deformation potential, D. The electron-phonon interaction Hamiltonian describing the strain-induced energy shift of the excited state, $|e\rangle$, can be written as [33, 98]

$$V_{e-phonon} = \hbar A \omega_m sin(\omega_m t + \phi)|e\rangle\langle e| \tag{7.1}$$

where A is a dimensionless driving amplitude proportional to both D and the amplitude of the mechanical vibration. For resonant or nearly resonant optical excitations, this interaction Hamiltonian leads to sideband optical transitions corresponding to the absorption or emission of integer numbers of phonons. To calculate the excited state population of the NV^- center, we solved the density matrix equations in the steady state, assuming that the NV^- is initially in the $|m_s = 0\rangle$ ground state and ω_m is large compared with the excited-state population decay rate. In the limit of weak optical excitation, the excited state population for an optical excitation field with frequency ω is given by

$$\rho_{ee}(\omega) \propto \sum_{n=-\infty}^{+\infty} \frac{J_n^2(A)}{(\omega - \omega_0 - n\omega_m)^2 + (\gamma/2)^2} \tag{7.2}$$

where γ and ω_0 are the linewidth and resonance frequency of the ZPL, respectively, and $J_n(x)$ is the Bessel function of the first kind. As shown in Eq. 2, the excitation of the NV^- center includes the contributions from all relevant sidebands, i.e., phonon-assisted optical transitions, with a relative weighting determined by $J_n^2(A)$. Fig. 7.3(d) and (e) show the theoretically calculated PLE spectra obtained for A=0, 1 and for A=4, 12, respectively, with $\gamma/2\pi$= 100 MHz. For $A \gg 1$, the frequency separation between the two PLE peaks derived from the calculation is linearly proportional to A. For a direct comparison between the experimental and theoretical results, we plot in Fig. 7.3(c) the calculated frequency separation with

a fixed conversion factor between A and the power of the 1.55 μm laser. A good agreement between the theory and experiment is achieved with 0.2 mW laser power corresponding to A=1. The same conversion factor is also used for the theoretical results shown in Fig. 7.3(f).

The linear scaling between the frequency separation of the two peaks in the PLE spectra and the amplitude of the external driving force shown in Fig. 7.3(c) suggests a classical interpretation of the PLE spectra at relatively large A. In this case, the frequency separation corresponds to the strain-induced relative shift of the excited state between the two turning points, i.e., the maximum displacements of the cantilever vibration. Furthermore, the excitation spectra at the turning points are expected to retain the spectrally sharp NV^- zero-phonon resonance except for a spectral shift. This is confirmed by the experimental and theoretical results shown respectively in Fig. 7.3(b) and (e). The experimental results on the linewidth of the PLE peaks as a function of the 1.55 μm laser power shown in Fig. 7.3(f) provide additional confirmation. As shown in Fig. 7.3(f), after a large increase in the linewidth, which occurs before the two peaks appear, the linewidth at relatively large A returns to values, which only slightly exceed the ZPL linewidth. The measured linewidths are also in general agreement with the calculated linewidths plotted in Fig. 7.3(f). Note that for the asymmetric PLE peaks, we determined the linewidth from the steep side of the peaks (see Fig. 7.3(b) and (e)).

7.4 Mechanical Photoluminescence Excitation Spectra

In the limit that the strain-induced frequency separation between the two PLE peaks far exceeds the ZPL linewidth, the PLE spectra depends sensitively on mechanical detuning (i.e., the detuning between the modulation frequency of the

1.55 μm laser and the resonance frequency of the mechanical mode), even when the detuning is small compared with γ_m, as shown in Fig. 7.4(a) and (b). Fig. 7.4(c) and (d) plot the NV^- fluorescence obtained as a function of the mechanical detuning at two different 1.55 μm laser powers, where the optical excitation frequency is fixed near a peak of the corresponding PLE spectrum obtained at zero mechanical detuning.

The NV^- fluorescence vs mechanical detuning shown in Fig. 7.4(c) and (d) can be viewed as mechanical PLE (mPLE), for which varying the mechanical detuning effectively shifts the resonance frequency of the NV^- optical transition. These spectra are characterized by two sharp resonances. Each resonance occurs at a mechanical detuning, for which the spectrally shifted optical transition at a turning point of the mechanical oscillation is resonant with the optical excitation field. The mPLE spectra shown in Fig. 7.4(c) and (d) feature the unusual behavior that the linewidth of the individual resonance,γ_{mPLE}, can be orders of magnitude smaller than the intrinsic mechanical linewidth, γ_m. Furthermore, the stronger the external mechanical drive, the sharper the resonance becomes.

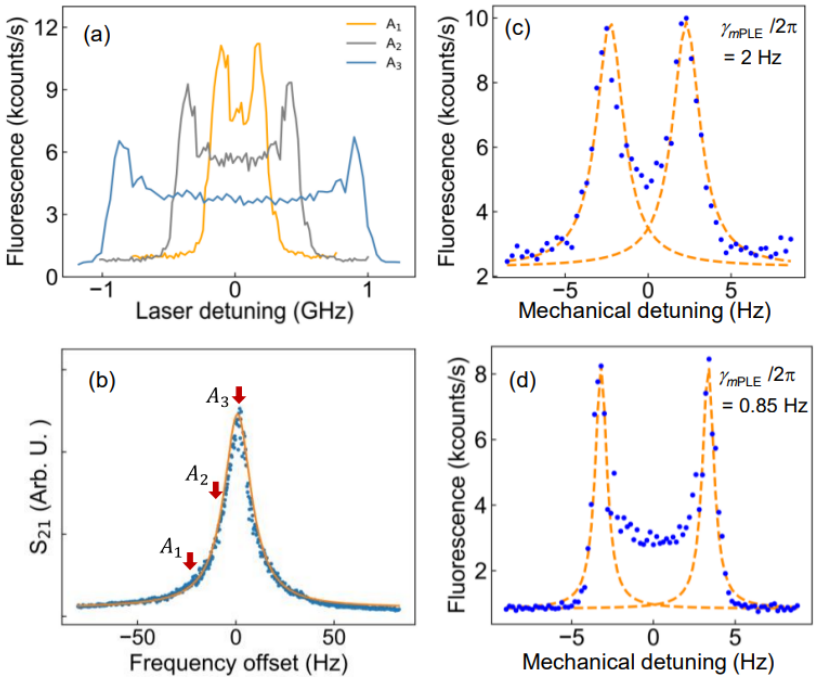

FIGURE 7.4. (a) PLE spectra of the NV^- center obtained with a 1.55 μm laser power of 6 mW, with the mechanical detuning indicated in (b). (b) Mechanical frequencies (indicated by the arrows) used for the PLE spectra in (a) relative to the resonance of the fundamental out-of-plane mode of the cantilever. (c) NV^- fluorescence as a function of the frequency detuning of the mechanical drive, obtained with a 1.55 μm laser power of 9 mW and with the optical excitation frequency fixed near a peak of the corresponding PLE spectrum obtained at zero mechanical detuning. The dashed lines are Lorentzian fits to the steep side of the resonances. (d) The same as (c) except for a 1.55 μm laser power of 14 mW.

7.5 Mechanical Sensing with NV^- Center Fluorescence

As shown in Fig. 7.4(a), the spectral position, s, of the NV^- optical transition at a cantilever turning point shifts with mechanical tuning, δ. For a mPLE resonance centered at δ_0, the linewidth of the resonance is determined by the mechanical detuning needed to induce a frequency shift of γ for the corresponding NV^- transition, i.e.,

$$\gamma_{mPLE} \cdot \frac{ds}{d\delta}|_{\delta=\delta_0} \approx \pm\gamma \tag{7.3}$$

In the limit that $S/\gamma \gg 1$, where S is the strain-induced frequency separation between the two peaks in the PLE spectra obtained at δ=0, we have

$$\gamma_{mPLE} \approx \frac{(4\delta_0^2 + \gamma_m^2)^2}{4|\delta_0|\gamma_m^2} \cdot \frac{\gamma}{S} \tag{7.4}$$

For Fig. 7.4(c) and (d), $|\delta_0|/2\pi$=2.3 and 3.5 Hz and S/2π=2.97 and 4.62 GHz (derived from the linear dependence between S and the 1.55 μm laser power in Fig. 7.3(c)), respectively. Theoretical estimates using Eq. 4 yield γ_{mPLE}/γ_m=0.088 and 0.041, in agreement with the experimentally obtained linewidth reduction,γ_{mPLE}/γ_m=0.091 and 0.039, for Fig. 7.4(c) and (d), respectively.

The sharp resonance in a mPLE spectrum can provide an effective mechanism to enhance the sensitivity of mechanical oscillator-based sensing [41], for example, mass sensing by monitoring the frequency shift of the mechanical oscillator [99]. The diamond cantilever used in this study has a mass near 0.5 nanogram. A mass change of 1 attogram results in a frequency shift of order 0.03 Hz. As shown in Fig. 7.4(d), the linewidth of the resonances in the mPLE is 0.85 Hz, compared with the intrinsic mechanical linewidth of 22 Hz. A greater reduction in the linewidth can be achieved with a stronger external mechanical drive. For the experimental implementation of mechanical sensing, a straightforward approach is to monitor the NV^- fluorescence while fixing the frequency of the nearly resonant external mechanical drive near the middle of the steep slope of a resonance in the mPLE spectrum.

To determine the sensitivity for measuring mechanical frequency shifts, we monitor the NV^- fluorescence while sinusoidally varying the mechanical detuning

(see Fig. 7.5), where the zero frequency-detuning corresponds to the midpoint of the steep side of a mPLE resonance. The sensitivity for the frequency-shift measurement can be defined as [100]

$$\eta = \frac{\sigma^{1s}}{|dF/d\delta|} \tag{7.5}$$

where σ^{1s} is the uncertainty for the fringe contrast F for 1 second averaging and $dF/d\delta$ is the gradient of F with respect to the mechanical detuning. From the results shown in Fig. 7.5, we estimate that η=0.01 and 0.02 $Hz/\sqrt{Hz}$ when a 1.55 μm laser power of 11 and 6 mW is used, respectively. The better sensitivity at stronger mechanical driving arises from the increase in the gradient due to the reduction in γ_{mPLE}. For comparison, frequency noise floor for traditional mass sensing experiments using cantilevers with $Q < 5000$ typically exceeds $0.1Hz/\sqrt{Hz}$ [99]. Note that the sensitivity shown in Fig. 7.5 is limited by the relatively small photon count rate used in the experiment and can thus be significantly improved.

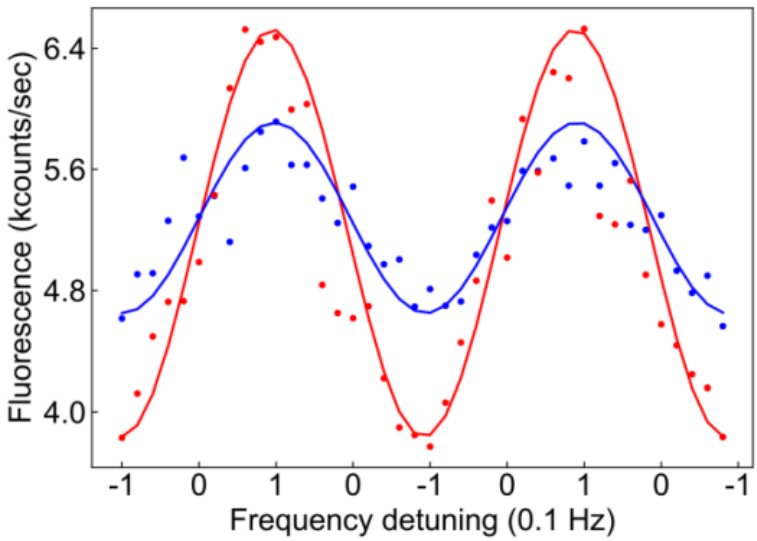

FIGURE 7.5. NV^- Fluorescence as a function of oscillating mechanical detuning. The solid lines are least-square fits to sinusoidal oscillations. For red (and blue) dots, a 1.55 μm laser power of 11 (and 6) mW is used, with other conditions nearly the same as those for Fig. 7.4.

In summary, using a diamond cantilever as a model spin-mechanical system, we have shown that in the unresolved sideband regime and under strong resonant mechanical driving, the excitation spectra of a NV^- optical transition feature two sharp peaks, corresponding to the two turning points of the oscillating cantilever. While the frequency separation increases linearly with the amplitude of the mechanical vibration, the linewidth of the peaks remains close to that of the zero-phonon line (ZPL). In the limit that the strain-induced frequency separation between the two peaks is large compared with the ZPL linewidth, the spectral position of the individual peak becomes highly sensitive to minute detuning of the mechanical drive, leading to sharp resonances in mechanical PLE spectra with a linewidth, which can be orders of magnitude smaller than the intrinsic mechanical linewidth. This enhanced sensitivity to mechanical detuning can provide an effective mechanism

for mechanical sensing, for example, mass sensing via measurements of induced mechanical frequency shifts. For earlier mechanical sensing studies, mechanical frequencies are monitored via piezo-resistive, capacitive, optical interferometric, or optomechanical measurements. These measurements are limited by the intrinsic linewidth of the relevant mechanical mode. While an NV^- center has been used in this study, similar spin-mechanical processes and their potential applications can also be pursued in other defect or material systems.

CHAPTER VIII

HONEYCOMBLIKE PHONONIC NETWORK OF SPINS WITH CLOSED MECHANICAL SUBSYSTEMS

This work was done in collaboration with Mark Kuzyk and Hailin Wang and has been published in Physical Review Applied as Ref. [46]. Mark carried out the theoretical calculations and Hailin designed, supervised the research project and prepared the manuscript. I performed the simulations and analyzed the results.

8.1 Introduction

In this chapter, we report the design of a diamond-based honeycomb-like phononic network, in which a mechanical resonator couples to three distinct phononic crystal waveguides. This two-dimensional (2D) phononic network extends an earlier study on one-dimensional (1D) phononic networks with closed mechanical subsystems [95]. With a special design for the phononic band structures of the waveguides, any two neighboring resonators in the 2D network and the waveguide between them can form a closed mechanical subsystem, which enables nearest neighbor coupling and at the same time circumvents the scaling problems inherent in typical large mechanical systems.

The building block of our 2D phononic network is a single mechanical resonator coupling to three distinct phononic crystal waveguides. Since the phononic band structure developed in the earlier study of 1D networks [95] is no longer adequate for the 2D networks, we have developed a new design principle for the phononic band structure of waveguides in the honeycomb-like 2D network. The key requirement is that one of the three distinct waveguides features two, instead of just one, phononic

band gaps within the spectral range of interest. The honeycomb networks can serve as an experimental platform for studies of topological quantum excitations such as anyons [101] and is of special importance for exploring and understanding topological quantum computing and especially quantum error corrections [102]. Extending the honeycomb networks to square or rectangular networks can potentially enable the implementation of topological quantum error correction schemes such as the surface code [103].

8.2 Honeycomb-Like Phononic Networks

For higher dimensions where a mechanical resonator couples directly to more than two distinct phononic waveguides, we require that a mechanical mode employed in the network can propagate in only one of the distinct waveguides. This mode thus needs to be in the phononic band gaps of other waveguides. For communications among qubits within the same mechanical resonator, a mechanical mode that is in the band gap of all waveguides is preferred. This means an additional requirement that the phononic band gaps of the waveguides involved should have an overlapping or common spectral region, in which no mechanical modes can propagate. For a 2D network, a given mechanical resonator can couple to three or four phononic waveguides. A square, or more generally, rectangular lattice can be formed with the use of four waveguides. Similarly, a honeycomb or honeycomb-like lattice can be formed with the use of three waveguides. In this paper, we focus on the honeycomb-like network, since it is easier to satisfy the requirements discussed above with three waveguides in a honeycomb-like lattice than with four waveguides in a rectangular lattice.

A natural choice for mechanical resonators in a honeycomb-like phononic network is a thin triangular plate with equal side length s. For additional flexibility in tuning mechanical frequencies of the resonator, we cut off the three corners, which have a side length of s', from the triangular plate, as illustrated in Fig. 8.1(a). The phononic network employs the symmetric compressional modes of the thin plate, i.e. modes that are symmetric with respect to the median plane of the plate. For a fixed s, we can adjust the frequencies of these mechanical modes by varying s'.

As shown in Fig. 8.1(a), three phononic waveguides,A, B, and C, are connected to the mechanical resonator along the three symmetry axes of the resonator. These waveguides feature a periodic array of elliptical holes and are effectively 1D phononic crystals [104]. As illustrated in Fig. 8.1(b), the width of the waveguide is w and the distance between neighboring holes is d. The semi-major axis and the semi-minor axis of the elliptical hole are a and b, respectively. Fig. 8.1(c) depicts a honeycomb-like lattice composed of these elementary units, for which waveguides A and B have the same length, with $L_A = L_B$, while waveguides C have a different length, L_C. For the numerical calculation of a diamond-based phononic network presented in this chapter, we take the thickness of the 2D structure to be 0.3μm. Note that we can offset a waveguide from the corresponding symmetry axis to tune the waveguide-resonator coupling rate.

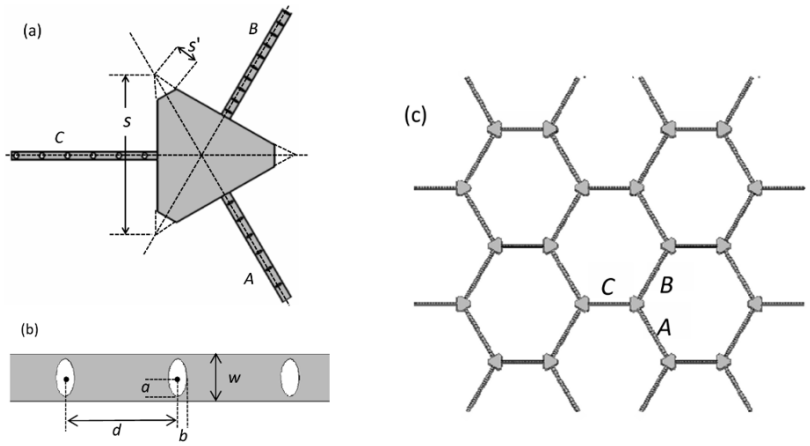

FIGURE 8.1. (a) The building block of the honeycomb-like phononic network, for which an equilateral triangular mechanical resonator, with the three corners cut off, couples to phononic crystal waveguides, A, B,and C, along three symmetry axes of the resonator. (b) The geometry of the phononic crystal waveguide. For the numerical calculations, we have taken (d, w, a, b) to be (6, 3, 1.1, 0.3) μm, (4, 3, 1.1, 0.3) μm, and (7.6, 2.0, 0.8, 0.76) μm for waveguides A, B and C, respectively. (c) A honeycomb-like lattice, for which waveguides$A$and$B$ have the same length, while waveguide C has a different length.

8.3 Phonon Band Gap and Mechanical Modes

For a honeycomb-like phononic network with closed mechanical subsystems, we need three waveguide modes propagating in waveguides A,B, and C, respectively. Each mode is forbidden in the other two waveguides. The three waveguides also need to have a shared or common band gap region, in which no mechanical modes can propagate in any of the waveguides. These requirements are impossible to satisfy, if we consider only a single band gap for each waveguide. However, the above requirements can be satisfied, if within the spectral region of interest, one of the waveguides feature two phononic band gaps, while the other two still have only a single phononic band gap.

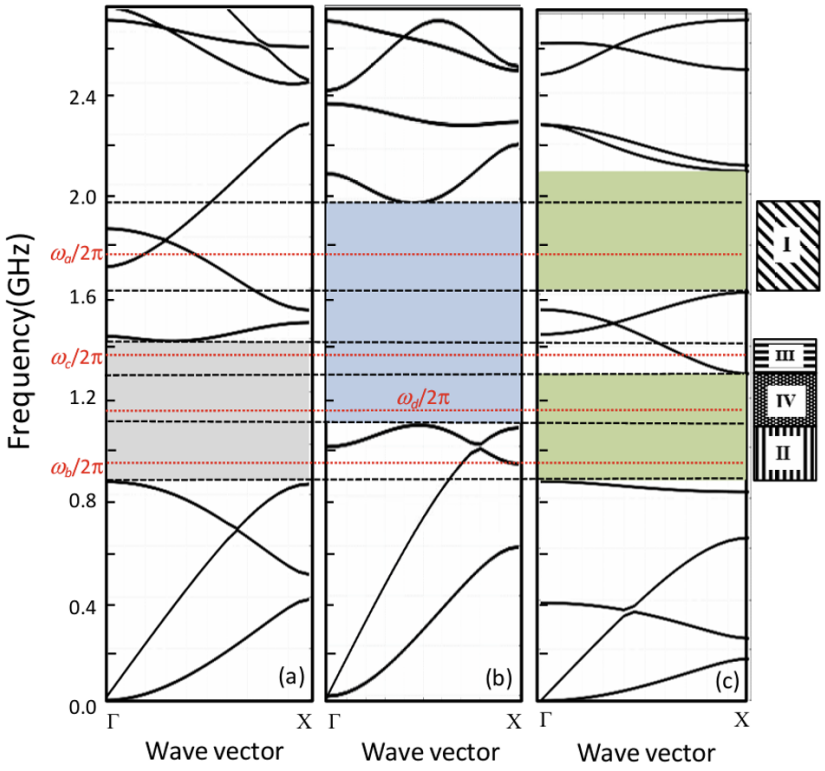

FIGURE 8.2. (a), (b), (c) The phononic band structures of the symmetric compression modes for waveguides A,B, and C, respectively. The shaded areas highlight the band gaps. The dashed lines mark four important regions. Region I is in the band gaps of waveguides B and C, but not A. Region II is in the band gaps of waveguides A and C, but not B. Region III is in the band gaps of waveguides A and B, but not C. Waveguide modes in Regions I, II, and III can only propagate in waveguides A,B and C, respectively. Region IV is a common band gap for all three waveguides. The dotted lines indicate the frequencies of the four resonator modes shown in Fig. 8.4.

Fig. 8.2 shows the phononic band structures of waveguides A,B, and C for the symmetric compression modes, calculated with the COMSOL Multiphysics software package and with $d = 6$, 4, 7.6 μm for waveguides A,B and C, respectively. Within the spectral region of interest, waveguides$A$and$B$ feature single phononic band gaps, while waveguide C features two phononic band gaps. For these calculations, we have taken (w, a, b) to be (3, 1.1, 0.3), (3, 1.1, 0.3), and (2, 0.8, 0.76) μm for

waveguides A,B and C, respectively. Fig. 8.2 highlights four special spectral regions. Region$I$is in the band gap of waveguides$B$ and C, but not A. Region$II$is in the band gap of waveguides$A$and C, but not$B$. Region III is in the band gap of waveguides$A$and$B$, but not C. In this case, waveguide modes in Regions I, II, and III can only propagate in waveguides A,B and C, respectively. Region IV is a common band gap for all three waveguides. Resonator modes in this region can be used for coupling among qubits within a given resonator [95]. The band diagram and especially the selection of the four special spectral regions shown in Fig. 8.2 depend on the geometric parameters of the waveguide. There are inevitable deviations or fluctuations from the design parameters in the fabrication of the waveguides. Fig. 8.3 shows, as an example, how the two band gaps in waveguide C change as we vary the four geometric parameters, d, w, a, and$b$, by up to $\pm$ 100 nm. As shown in the figure, the lower band gap is more stable against parameter variations than the upper band gap and the strongest dependence occurs for the geometric parameters of the elliptical holes, including the semi-major axis, a, and the semi-minor axis, b. For the four special spectral regions shown in Fig. 8.2, the stability of the lower band gap of waveguide C is of more importance than that of the upper band gap. The lower band gap affects the boundaries for regions II, III, and IV, with region III being the narrowest among the four spectral regions. In addition, there are no spectral separations between regions II, III, and IV. In comparison, region$I$is spectrally separated from the other three regions and is the widest among the four spectral regions. In this regard, our design of the four spectral regions for the desired waveguide operations should be able to tolerate considerable variations in the geometric parameters of the waveguides.

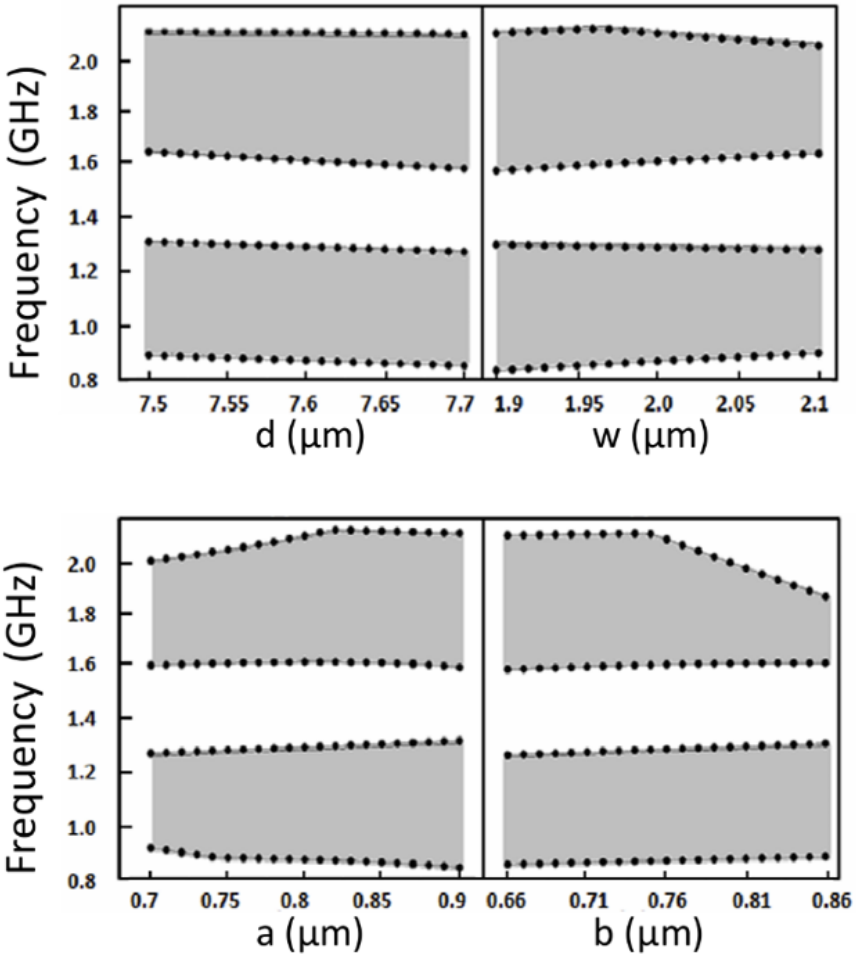

FIGURE 8.3. The two band gaps (highlighted by the shaded areas) of waveguide C as a function of four waveguide parameters, d, w, a, and b. These parameters are varied by up to $\pm$ 100 nm around the desired value, $(d, w, a, b) = (7.6, 2.0, 0.8, 0.76)$ μm.

8.4 Calculation of Phononic Band Structures and Mechanical Modes

We have carried out finite element numerical calculations with COMSOL Multiphysics to analyze the phononic band structures of 1D and 2D phononic crystal structures and to determine the frequencies and field patterns of mechanical normal

modes in a mechanical resonator. For variations or sweeps of geometric parameters, we have combined the use of COMSOL Multiphysics and MATLAB. The diamond material parameters used in the numerical calculations include Young's modulus E = 1050 GPa, Poisson ratio ν=0.2, and the material density ρ = 3539 kg/m^3. For the calculation of mechanical modes in an elastic material, we treat these modes as a continuum field with a time-dependent displacement, $\mathbf{Q}(\mathbf{r}, t)$, which satisfies the wave equation,

$$\rho\partial_t^2 Q = (\lambda + \mu)\nabla(\nabla \cdot Q) + \mu\nabla^2 Q \tag{8.1}$$

where the Lame constants are given by

$$\lambda = \nu E/((1+\nu)(1-2\nu)), \mu = E/(2(1+\nu)) \tag{8.2}$$

8.5 Closed Mechanical Subsystems

The nearest neighbor coupling in our phononic network takes place via closed mechanical subsystems, which consist of any two neighboring resonators and the waveguide between them. The waveguide modes in this closed mechanical subsystem are standing mechanical waves. In the limit of relatively short waveguides, we can approximate a given waveguide as a single-mode waveguide. Because of the relatively small resonator-waveguide coupling rate, quantum state transfers or two qubit gates between spins in neighboring resonators require that the resonator mode is nearly resonant with the corresponding waveguide mode. Specifically, we need three resonator modes, with frequency ω_a, ω_b, and ω_c, to be nearly resonant with the corresponding waveguide modes in waveguides A, B, and C, respectively.

The frequency of a resonator mode depends on the side length s and s' as well as the spatial displacement pattern. The frequency of a waveguide mode depends on the waveguide length as well as other geometric parameters including d, w, a, b. We can tune the frequency of a waveguide mode without affecting the phononic band structure by varying the length of the waveguide. For the honeycomb-like lattice discussed here, we have chosen $L_A = L_B$ (see Fig. 8.1(c)). This means variations of the waveguide lengths alone cannot tune independently the frequencies of all three relevant waveguide modes. An additional tuning parameter, such as s' , can be used to satisfy the resonance condition for all three sets of resonator and waveguide modes.

Fig. 8.4(a), (b) and (c) show the displacement patterns of three resonator modes that can couple to one of the three distinct phononic waveguides and are in the band gap of the other two waveguides. The frequencies of the three modes are respectively $\omega_a/2\pi$=1.7339 GHz, $\omega_b/2\pi$=0.9634 GHz, and $\omega_c/2\pi$=1.3388 GHz. The displacement pattern of a mechanical mode, whose frequency, $\omega_d/2\pi$=1.1691 GHz, is in the band gap of all three waveguides (region IV in Fig. 8.2), is displayed in Fig. 8.4(d).

For a closed mechanical subsystem containing two neighboring resonators and the waveguide between them, the resonator-waveguide coupling leads to the formation of three normal modes. In the single-mode waveguide limit, we can use numerically-determined normal mode frequencies to deduce the effective detuning, Δ, between the resonator and waveguide modes and the resonator-waveguide coupling rate g, according to [95]

$$\Delta = \omega_+ + \omega_- - 2\omega_0, g = \sqrt{((\omega_+ - w_-)^2 - \Delta^2)/8} \tag{8.3}$$

where ω_+ , ω_-, and ω_0 are the frequencies of the three normal modes. Note that with $\Delta = 0$, the normal mode with frequency ω_0 is a dark mode, for which there

is no waveguide mode component. With L_A=L_B=86.55 μm and L_C= 89.62 μm, the three resonator modes shown in Fig. 8.4(a), (b) and (c) are resonant or nearly resonant with the corresponding waveguide modes. The geometric parameters of the waveguides are the same as those used for Fig. 8.2. The waveguide mode spacing is 31, 37, 33 MHz for waveguides A, B,and C, respectively, as determined from numerical calculations of the freestanding waveguides without coupling to adjacent resonators. Fig. 8.4(e) plots the displacement patterns of the normal mode triplets of the closed mechanical subsystems, which feature frequencies, from top to bottom, (1.7344, 1.7361, 1.7378) GHz, (0.9660, 0.9695, 0.9724) GHz, and (1.3399, 1.3451, 1.3503) GHz associated with waveguides A, B, and C, respectively. The corresponding waveguide-resonator detuning and coupling rates are Δ_A =0, g_A=1.2 MHz; Δ_B=0.48 MHz, g_B=2.3 MHz; and Δ_C=0, g_C=3.7 MHz.

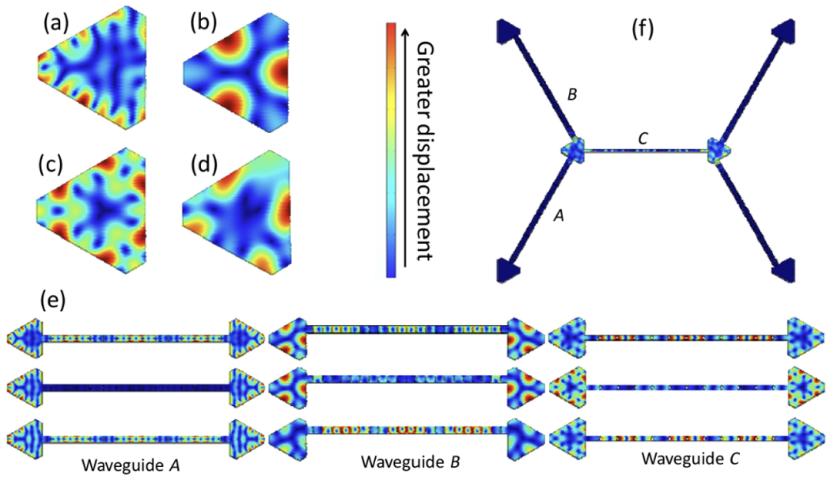

FIGURE 8.4. (a), (b), (c), (d) The displacement patterns of mechanical resonator modes with $\omega_a/2\pi$=1.7339 GHz, $\omega_b/2\pi$=0.9634 GHz, $\omega_c/2\pi$=1.3388GHz, $\omega_d/2\pi$=1.1691 GHz, respectively, and with s=21 μm and s'=3.15 μm. The modes with frequency,$\omega_a, \omega_b, \omega_c$, are nearly resonant with the corresponding waveguide modes in waveguides A, B, C, respectively. The mode with frequency ω_d is in the gap of all three waveguides. (e) The displacement patterns of the normal mode triplets of the closed mechanical systems associated with the three waveguides. Waveguide$B$is offset by 4 μm from the axis connecting the centers of the two resonators. The waveguide parameters and the frequencies of the normal modes are discussed in the text. (f) The displacement pattern of a normal mode in a local region of the phononic network. This mode, which can propagate in waveguide C, is forbidden in waveguides$A$and B, leading to a closed mechanical subsystem containing waveguide C and the two resonators coupled directly to the waveguide.

As shown in Fig. 8.4(e), waveguide$B$is offset by 4 μm from the axis connecting the centers of the two resonators. With a zero offset, g_B would approach the relevant waveguide mode spacing, breaking the single-mode waveguide approximation. We also note that the dark mode is not completely dark for the closed system associated with the waveguide C, even with the zero detuning deduced from Eq. 1. This is due to the residual coupling to nearby waveguide modes, when g_C becomes significant compared to the corresponding waveguide mode spacing.

Fig. 8.4(f) shows the displacement pattern of a normal mode in a local region of the phononic network. As expected, the mechanical vibration is confined in the closed mechanical subsystem containing the waveguide C and the two resonators coupled directly to the waveguide. The frequency of this mode, 1.3570 GHz, however, differs slightly from the corresponding normal mode frequency, 1.3451 GHz, calculated separately for the corresponding closed mechanical subsystem. In this case, while the mechanical vibrations cannot propagate in the other connecting waveguides, evanescent penetration of the mechanical vibrations into these waveguides alter both the spatial pattern as well as the frequency of the mechanical mode.

The relevant mechanical frequencies of a phononic network depend sensitively on the dimensions and geometric parameters of both the resonators and the waveguides. The achievement of the resonance between the resonator and the corresponding waveguide modes thus presents a formidable technical challenge for the experimental realization of the phononic network. In this regard, for the various schemes on the quantum state transfer or two-qubit quantum operations in a closed mechanical subsystem [95], the schemes that can tolerate considerable detuning between the resonator and the corresponding waveguide modes are preferred. It should also be noted that for phononic networks with closed mechanical subsystems, the resonance conditions are only required for local mechanical subsystems. Our architecture is robust against global or long-range variations in the resonator and waveguide frequencies so long as the local resonance conditions are satisfied.

8.6 Phononic Crystal Shield

While it was straightforward to use a square phononic crystal lattice as a phononic shield for 1D phononic networks as well as single mechanical resonators [7], additional

modifications are needed to embed a honeycomb-like phononic network in a phononic crystal lattice because of the special geometry and symmetry of the honeycomb-like network. To provide the needed isolation and protection for the honeycomb-like phononic network, we have used a square phononic crystal lattice as a phononic shield and have made minor modifications in the square lattice, while retaining the protection provided by the relevant phononic band gaps.

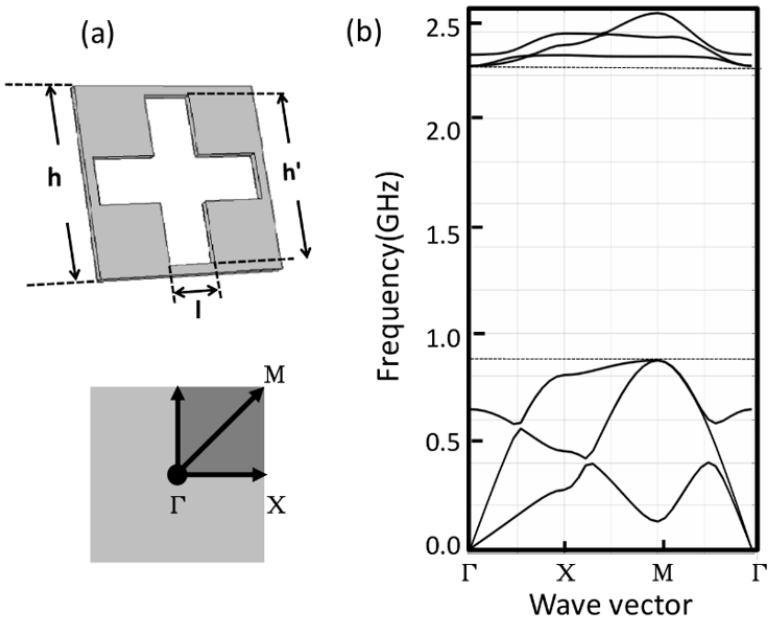

FIGURE 8.5. (a) The unit cell of a square phononic crystal lattice with a period of 3.8 μm, along with the reciprocal space of a square lattice. The lattice parameters are h=3.8μm, h'=3.5μm, and l =1μm. (b) The phononic band structure of the symmetric compression modes of the square lattice, featuring a large gap spanning from 0.85 to 2.35 GHz.

The unit cell of a square phononic crystal lattice, with a period of 3.8 μm, is shown in Fig. 8.5(a). The phononic band structure of the symmetric compression modes of the square lattice features a large band gap spanning from 0.85 to 2.35 GHz (see Fig. 8.5(b)), which can provide excellent protection for all the relevant

mechanical modes in our phononic network. Fig. 8.6 shows schematically the attachment of a honeycomb-like phononic network to a square phononic crystal lattice. The phononic structure highlighted by the dotted line box in Fig. 8.6 shows that phononic crystal waveguide C with a period of 7.6 μm is embedded directly in the square phononic crystal lattice with bridges or linkers of suitable length. In this case, the phononic band gap of the waveguide also provides additional protection for the relevant mechanical modes in the network.

The phononic structure highlighted by the dashed line box in Fig. 8.6 consists of a section of the square phononic crystal lattice attached to phononic crystal waveguide C near the bottom of the structure. Note that adjacent sections of square phononic crystal lattices can be connected together at the boundary with bridges of suitable length. Given the relatively large size of these sections, the section boundaries will have negligible effects on the phononic waveguides.

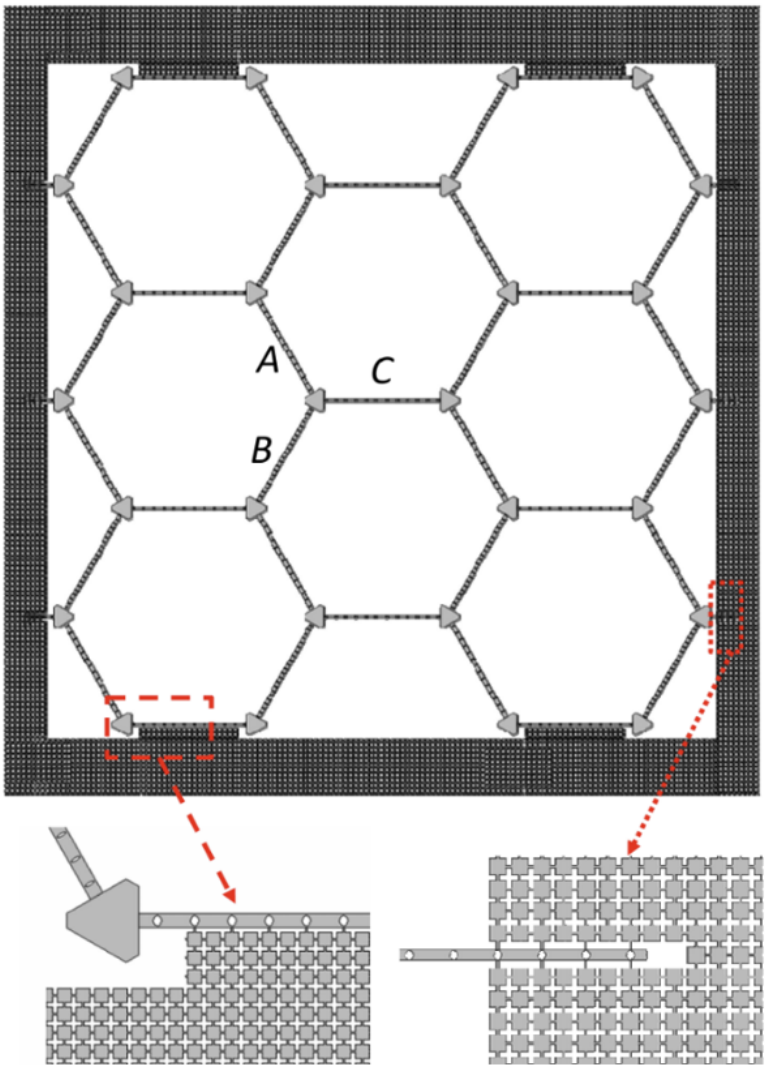

FIGURE 8.6. Schematic of the honeycomb-like phononic network attached to the square phononic crystal shield shown in Fig. 8.5. The expanded drawings show in detail the attachment of the waveguide C with a period of 7.6 μm to the square phononic crystal lattice.

8.7 Conclusions

In summary, we have extended the earlier theoretical work of 1D phononic networks with closed mechanical subsystems to 2D phononic networks by using a honeycomb-like lattice and by designing a special band structure for the phononic

crystal waveguides. For the 2D honeycomb-like network, a closed mechanical subsystem can be formed from any two neighboring resonators and the waveguide between them. These closed subsystems enable the nearest neighbor coupling in the 2D network and overcome the scaling problems inherent in large mechanical systems. Experimental realization of this type of 2D phononic networks of spin qubits can open up a new platform for pursuing fault-tolerant quantum computers and for exploring topological quantum error corrections. Finally, we note that while our numerical design is based on the use of diamond, for which both photonic and optomechanical crystals have been successfully fabricated [9], the design can be easily extended to other material systems.

CHAPTER IX

CONCLUSION AND OUTLOOK

9.1 Ultracoherent Diamond Spin-Mechanical Resonators

Spin-mechanical systems stand out as a promising hybrid platform for quantum computing due to the superior properties of color centers in diamond and mechanical resonators. Such hybrid systems combine strengths from its individual parts – defect centers in diamond offer long spin coherence time and mechanical waves couple to a wide range of systems while featuring loss rate orders of magnitude lower than photons. The exciting experimental progress on electro-mechanical systems has further motivated the development of spin-mechanical systems. However, challenges remain to be addressed to fully access the quantum regime of spin-phonon coupling.

One of the major challenges was the underdevelopment of diamond nanofabrication techniques compared to materials like silicon. We were able to develop our own diamond processing protocols including backside thinning and soft-O_2 etching, which have shown to effectively produce diamond membranes with precisely defined nanostructures while maintaining coherence properties of color centers in diamond. This was presented in Chapter IV, following Chapter II and III where we give a brief review on color centers in diamond and mechanical resonators.

The second major challenge lies in the conditions for reaching the quantum regime of spin-mechanical coupling – to achieve a cooperativity greater than one. This emphasizes the necessity of attaining high Q-factor nanomechanical resonators, which could be realized through phononic band gap engineering to eliminate structural clamping losses. With our diamond processing capabilities, we are able to design

and fabricate diamond nanomechanical resonators embedded in large area phononic band gap structures.

Our first success comes from diamond cantilevers – with the protection of phononic shields, a three-orders-of-magnitude increase in mechanical Q-factors was achieved, leading to Q-factors of 10^6 in mechanical resonances of up to 100MHz. Temperature dependence was also carried out from room temperature to millikelvin temperatures, showing that the Q-factors obtained at a few Kelvins are still limited by the materials loss.

However, gigahertz frequency diamond resonators are highly desired for spin-mechanical studies in the resolved sideband regime. This led us to explore geometries outside of cantilevers and find Lamb wave resonators – a thin plate featuring gigahertz in-plane compression motions. We overcome the difficulties of driving in-plane motions with the use of optical gradient force from a highly focused telecom laser, and detected the displacement as small as a few picometers with strain coupling to silicon-vacancy centers. We demonstrated a diamond LWR at 0.977GHz featuring a Q-factor as high as 1.2×10^7 at around 7 K, with the Qf-product comparable to the state-of-the-art silicon optomechanical crystals.

A driven mechanical system under the unresolved sideband regime could have applications in mechanical sensing. Photoluminescence excitation spectra of an NV center under strong mechanical driving could feature enhanced sensitivity to minute mechanical detuning, leading to applications including mass and frequency detuning sensing.

Another application of the spin-mechanical system is to form diamond-based honeycomb-like phononic networks. A mechanical resonator could couple to multiple phononic crystal waveguides, with two resonators and the waveguide between them

forming a closed mechanical subsystem. This two-dimensional phononic network could enable nearest neighbor coupling and offers a pathway to circumvent the scaling problems typically encountered in large mechanical systems.

In summary, our work demonstrates the development of an ultra-coherent diamond spin-mechanical resonator platform, paving the way towards accessing the quantum regime of spin-phonon coupling. On the basis of this, spin-mechanical hybrid systems could become comparable to electromechanical systems for quantum computing. Characterization of cooperativity and temperature dependence are still needed, and we will leave these to future studies.

9.2 Phononic Cavity-QED with SiV^- in Diamond

There are different schemes for realizing spin-phonon coupling and cooperativity characterizations. Especially, the spin states of SiV^- centers in diamond can couple directly to phonon modes at a few GHz and enable a phononic cavity-QED type of experiment. The cooperativity can be significantly higher than SiV^- excited states coupling due to the narrow spin linewidth especially at temperatures below 1K. For these types of experiments, characterizations on coherent population trapping (CPT) processes and phonon-induced relaxation at millikelvin temperatures are required in the first place.

We collaborated with Oak Ridge National Lab on characterizations of SiV^- centers at millikelvin temperatures [105]. The sample was mounted inside a dilution refrigerator (Leiden Cryogenics CFCS81-1000M) with a three-dimensional (3D) vector magnet installed (American Magnetics). Spin linewidth determined by T_2^* can be extracted from the CPT linewidth, and our measurement showed a near 100-

fold increase in spin lifetime when the sample gets cooled down from 4K to below 1K [105].

Combined with our experimental advances on ultra-coherent GHz diamond spin-mechanical resonators, we can carry out several types of spin-phonon coupling experiments: Phononic cavity QED with Raman-assisted spin transition as in Fig. 9.1 (a), $T_{1,spin}$ measurements of SiV^- spin through acoustic Purcell effect as in Fig. 9.1 (b), or characterization of spin-phonon coupling through an optomechanically induced transparency-type (OMIT) of experiment as in Fig. 9.1 (c). These experiments feature different parameter-based cooperativity, for example $T_{1,spin}$ or T_2^*-based cooperativities. For example, benefiting from the low temperature environment in a dilution fridge, we could potentially obtain a $\gamma_s/2\pi$ of $\sim$1kHz with a ^{12}C-enriched diamond sample and expect a Q-factor of 10^7 following the temperature dependence behavior observed earlier. We have also been able to scale down the dimensions of our LWR to 4GHz (Fig. 6.4(a)). These combined lead to an estimated spin-phonon coupling cooperativity approaching 10^6 - potentially rivaling electromechanical systems in quantum computing applications.

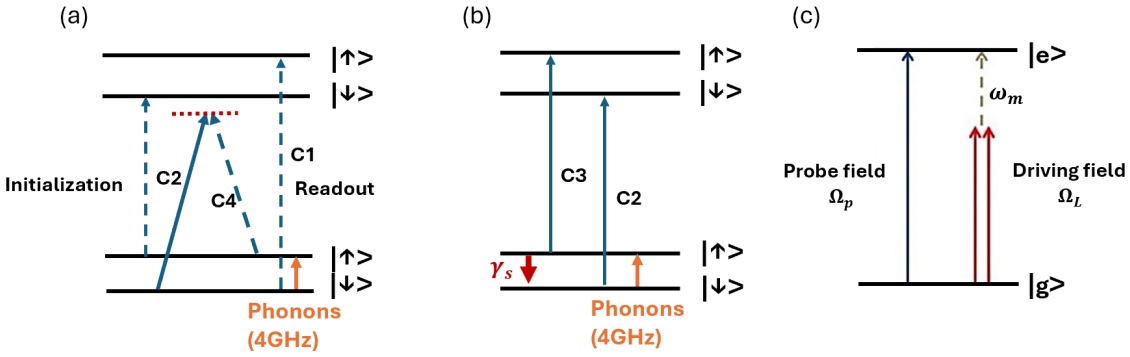

FIGURE 9.1. Possible future experimental schemes for characterizing spin-phonon coupling cooperativity. (a) Phononic cavity QED with Raman-assisted spin transition. (b) $T_{1,spin}$ measurements of SiV^- spins through acoustic Purcell effect. (c) OMIT-type of experiment for characterizing spin-phonon coupling strength.

9.3 Phononic Networks with Coupled Mechanical Resonators

As a hybrid quantum system, diamond spin-mechanical resonators can furthermore serve as the building block for a mechanical-type quantum network. Past research studies have proposed designs for one and two-dimensional quantum networks based on mechanical resonators [46, 95]. For these types of networks, long-range coupling between spin qubits will be mediated by phonons and controlled by spin-phonon coupling processes, for example strain coupling to the spin states or orbital states of color centers in diamond.

A design of Wannier-Stark ladders of diamond LWRs has been proposed in [106]. Formed by a linear chain of mechanical resonator, the effective range of phonon-mediated spin couplings is determined by the degree of localization in the mechanical Wannier-Stark ladder. Three distinct coupling schemes with different geometry designs can enable a large range of nearest neighbor coupling rates: The nodes of two LWRs (NN coupling), the antinodes of two LWRs (AA coupling) and between the node of one LWR and the antinode of another LWR (AN coupling). [106]. The combination of these three geometries can further enable a two-dimensional mechanical network where long and short range of connectivity can be realized in different regions across the whole network structure.

The entire mechanical network can also be embedded in a phononic structure where the band gap protects the mechanical modes from coupling to the outside environment [106]. This type of mechanical network structure can also be extended to other material platforms which feature spin qubits with excellent optical and spin properties, for example silicon-carbide and silicon platforms. Moreover, mechanical quantum networks of spins with long-range connectivity can contribute to the

implementation of newly developed quantum low-density parity-check(QLDPC) codes in a solid-state system for quantum computing [107].

APPENDIX

QUENCHING AND BROADENING OF SIV^- CENTERS UNDER 1550NM LASER

This work was done in collaboration with Hailin Wang and will be published in future. Hailin designed, supervised the research project and edited the manuscript. I performed the experimental measurements, data analysis and prepared the draft. In this part of the appendix we present our experimental findings on the quenching and broadening of SiV^- centers under the illumination of 1550nm laser.

Telecom wavelength lasers operating at around 1200nm-1600nm is crucial in applications including optical communication, networking and fiber optics technologies [108]. In quantum information science, telecom lasers also play a crucial role in photonic integrated circuits [109], quantum dot-based light sources [110, 111] and quantum teleportation protocols [112]. In our spin-mechanical studies, lasers at around 1.55μm is a great light source for optical driving of mechanical modes due to the easy accessibility of high-power optical amplifiers, fibers and electro-optical modulators. We observed unexpected quenching and broadening of SiV^- excitation spectra under application of 1.55μm laser beams. Here we report our experimental findings and characterization of the effects.

We use the same SiV^- as in Chapter VI with its location indicated in Fig. 6.8(c). The sample is mounted in a Cryostation at a temperature of 7K. To overlap the 1.55μm laser with the red laser well so that both lasers are placed on the same SiV^-, we simply align them by walking the mirrors and making sure the two laser spots overlap at a near and far point. In order to reduce spectral diffusion and complications in the pulse sequence brought by the green laser, we illuminated the

SiV^- beforehand with a blue laser (CivilLaser 100mW Blue Laser) for prolonged time (>5h) at a power of about 50mW. This stabilizes the charges of the SiV^- and removes the requirement for green initialization completely [59]. The experimental setup is the same as in Fig. 6.6(b) for our spin-phonon coupling experiment with SiV^- except a time-tagger (Swabian 20) is used for getting time-domain characteristics for the 1.55 μm effects.

Fig. A.1 shows the quenching and broadening of the SiV^- photoluminescence excitation (PLE) spectra under continuous-wave 1.55μm illumination. Pulse sequence used is indicated as an inset in Fig. A.1(a). To check if green laser in this case could mitigate the quenching and broadening effects due to its charge stabilization capability, we test this SiV^- under different green powers and telecom powers, adopting 0, 50nW, 25μW and 1mW of green laser power with a duration of 3μs, while scanning the telecom laser power from 0 to 35mW. From Fig. A.1(a) we can see that the PLE height quenched significantly as 1.55μm laser power went up for all green powers. However with the presence of green laser, higher green power leads to slower and less quenching, even if with only 50nW of green power. As green laser power continues going up, quenching of PLE signal caused by green laser itself dominates over quenching by the 1.55μm, as can be seen from the first data point at 1mW green and 0mW 1.55μm power. From Fig. A.1(b), we can see that higher 1.55μm power significantly broadens the PLE linewidth, while higher green power applied helps mitigate the broadening effect. The exact mechanism for quenching and broadening of SiV^- by 1.55μm is still unclear at this point, but the effects of green laser even at 50nW power indicate mechanisms beyond pure heating brought by the 1.55μm laser.

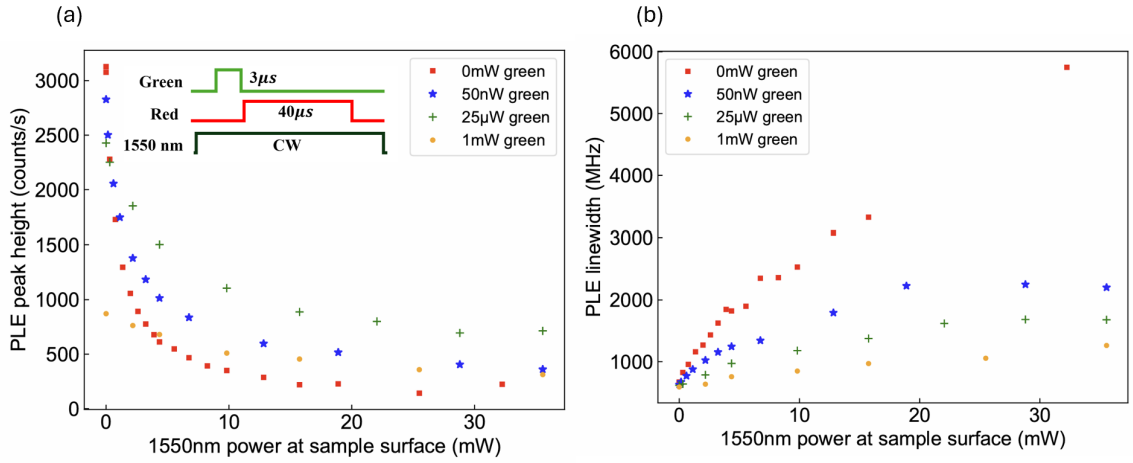

FIGURE A.1. Quenching and broadening of SiV^- PLE spectra under different 1550nm laser powers and green initialization powers. (a) PLE peak height versus 1550nm laser power. (b) PLE spectra linewidth versus 1550nm laser power.

In order to study the mechanism behind this effect, we carry out time domain measurements to learn about the time scale of the quenching of PLE. The pulse sequence is indicated in Fig. A.2 where a 10μs telecom laser pulse at 19mW is applied in the middle of the PLE sequence. We see that upon application of the telecom laser, a sharp rise in the PLE counts shows up, followed by a rapid and significant drop then a slow recovery to the original PLE signal level once the telecom laser beam is turned off. The sharp rise at the beginning happens on a time scale shorter than the time resolution of the measurement which is 100 ns.

The time scale of the slow recovery process could provide insight about the possible mechanisms. We were able to fit the recovery with a single exponential:

$$y = -a * e^{-t/\tau} + b \tag{A.1}$$

Where τ describes the time constant for the slow recovery. Fig. A.2 shows the curve fitting to the recovery process at a red power of 1μW, with a fitted value of τ=149$\pm$4.7μs.

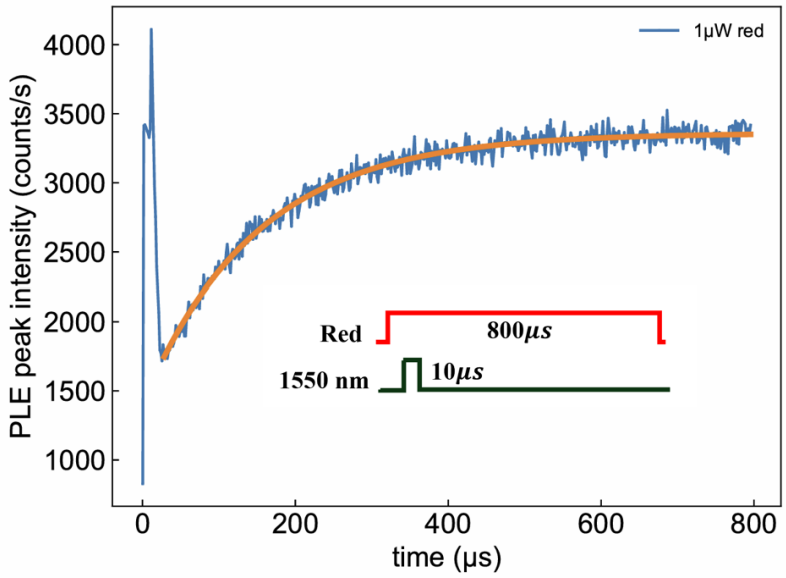

FIGURE A.2. Time characterizations on the effects of 1550nm laser power. A short 10μs 1550nm laser pulse is applied during the red laser pulse for the PLE excitation. The pulse sequence is shown and a single-exponential fit is applied to the slow recovery part of the PLE counts.

It is natural to check the dependence of the slow recovery process on the power of 1.55μm laser. While keeping the red laser power for the PLE sequence constant, we change the power output of the 1.55μm laser amplifier from 4 to 32mW. Fig. A.3 (a) shows the comparison of time domain behaviors on the PLE recovery under different 1.55μm laser power. Higher 1.55μm laser power leads to more severe quenching of the PLE counts, as expected from previous discussions. However, the time constant for the slow recovery process did not show clear dependence on the 1.55μm laser power and remained rather constant for a given red laser power. For a red laser power at 1.2μW and 0.7μW, the slow recovery time constant is τ=190μs and τ=125μs.

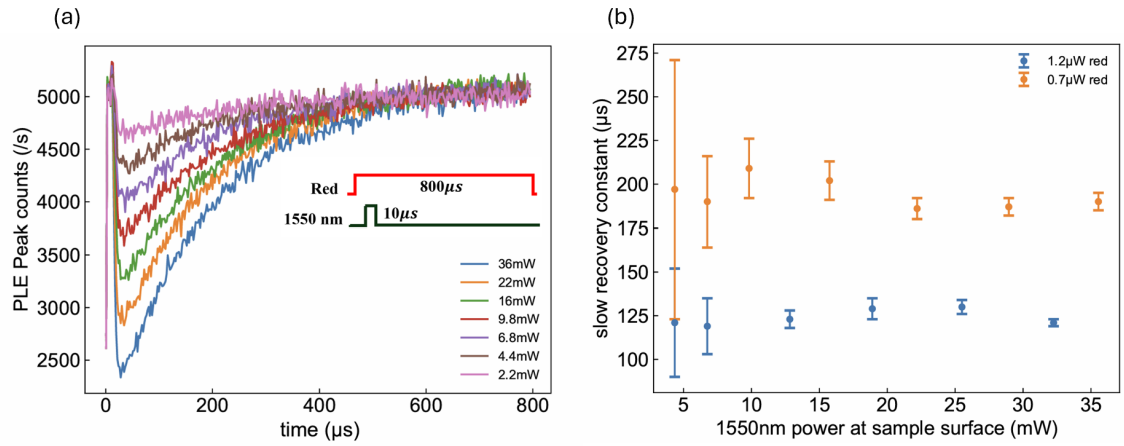

FIGURE A.3. 1550nm laser power dependence on the time constant of the PLE slow recovery process. Pulse sequence used is indicated in (a). (a) Time domain characteristics of the PLE counts under different powers of 1550nm laser power. (b) Slow recovery time constant versus 1550nm laser power at the sample surface for two different red laser powers at 1.2μW and 0.7μW.

We carry out measurements on dependence of the red laser power. Fig. A.4 shows the comparison of the quenching recovery processes under red laser powers ranging from 0.4μW to 3μW. Strong dependence on red laser power is shown in Fig. A.4(b) where higher red laser power leads to exponentially faster recovery time. The strong dependence on red power and independence on the 1.55μm power indicates a quenching mechanism related to the excited states absorptions.

To better understand the quenching mechanism, we do a comparison of the PLE behaviors between when the 1.55μm laser pulse is placed before the red laser pulse and after the red laser pulse, corresponding to the application of telecom laser before and after the SiV^- is in the excited states. Fig. A.5 shows a distinct difference of behaviors under two cases. For telecom laser placed right before the red laser pulse, no evident quenching of PLE photon counts is observed (orange curve), compared to the case where the telecom laser is placed during the PLE excitation pulses (blue curve). The pulse sequences for the two cases are indicated in Fig. A.5. This shows

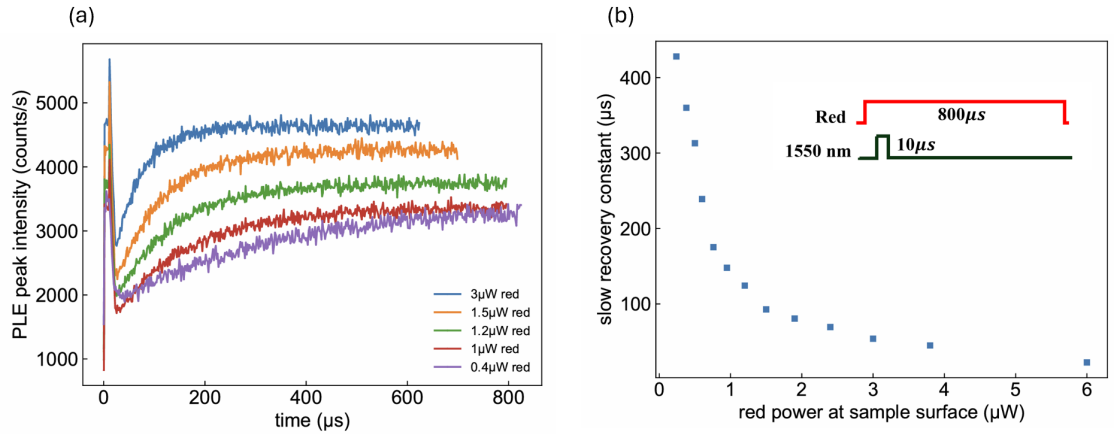

FIGURE A.4. Red laser power dependence on the time constant of the PLE slow recovery process. Pulse sequence used is indicated in (b). (a) Time domain characteristics of the PLE counts under different powers of red laser power for SiV^- excitation. (b) Slow recovery time constant versus red laser power at the sample surface.

that the quenching induced by the 1.55μm laser power is indeed due to excited states absorptions of the SiV^- centers in diamond. It is also worth noting that we do not see quenching or broadening of PLE spectra when working with NV^- centers in diamond at similar temperatures under high power 1.55μm illumination.

Green lasers have shown to be effective in mitigating the quenching and broadening of PLE signals in Fig. A.1. Here we do a more detailed study by looking at the recovery under different green pulse width and power in the time domain. A measurement example is shown in Fig. A.6(a) where the orange curve has one short 100μW green pulse with a width of 200ns superimposed onto the telecom laser pulse at the end. We see that the PLE counts rise by an amount after application of the green laser pulse, followed by a slow recovery to the original level. Fig. A.6 (b) shows the decrease in slow recovery time for different green laser power and duration. Note that the differences in the recovery time at 0ns green laser powers are due to the leak out from acoustic-optical modulator (AOM).

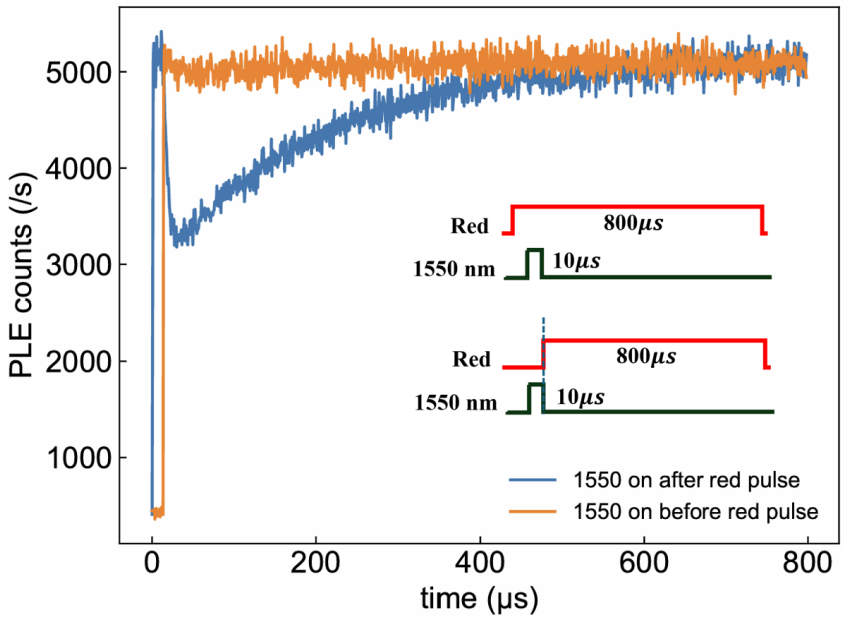

FIGURE A.5. Comparisons between behaviors of PLE counts recovery when the 1550nm laser pulse is placed ahead of (orange curve) and after (blue curve) the red laser pulse. Pulse sequence is indicated as the inset.

In summary, we observed the quenching and broadening of SiV^- PLE spectra under application of telecom laser beam at 1.55μm. Time-domain characteristics show that the recovery of the decay depends strongly on the power of the red laser and rather independent to the 1.55μm laser power. Moreover, placing the 1.55μm laser pulse ahead of the red laser does not induce quenching, showing evidence that the quenching is due to absorptions from the excited states of SiV^-. Green laser also shows effects for mitigating the quenching and broadening of SiV^-. The detailed mechanisms for the induced quenching and broadening still need further studies, but these measurements provided several ways of mitigating the effects, therefore could be useful for quantum optics experiments involving interactions of telecom laser beam and SiV^- centers.

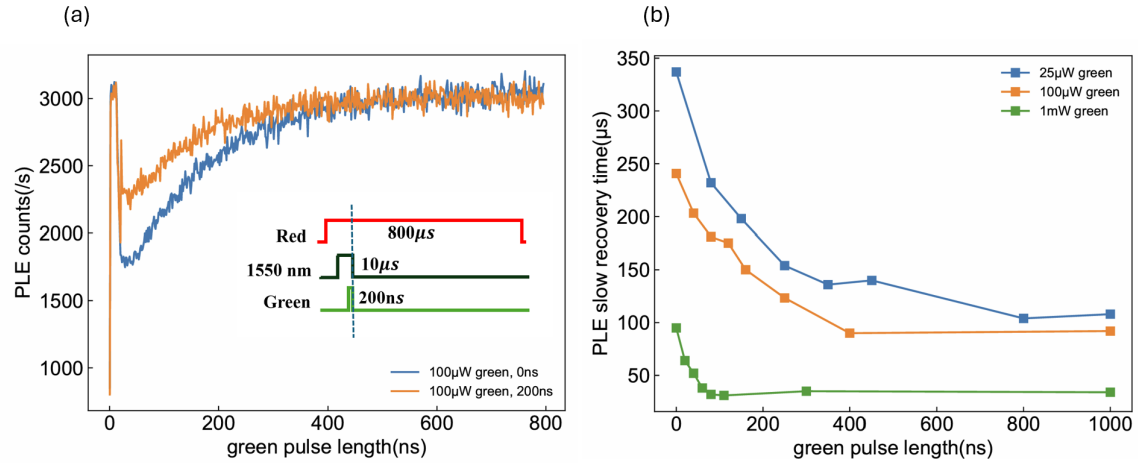

FIGURE A.6. Effects of green initialization laser with different duration and powers on the time constant of the PLE slow recovery process. Pulse sequence used is indicated in (a). (a) A comparison of time-domain characteristics of PLE recoveries when a 200ns green initialization laser at a power of 100μW (orange curve) is applied and no green is applied. (b) Slow recovery time constant versus green initialization laser durations under different green powers.

REFERENCES CITED

[1] Gabriel Popkin. Quest for qubits, 2016.

[2] Donghun Lee, Kenneth W Lee, Jeffrey V Cady, Preeti Ovartchaiyapong, and Ania C Bleszynski Jayich. Topical review: spins and mechanics in diamond. *Journal of Optics*, 19(3):033001, 2017.

[3] Jeronimo R Maze, Adam Gali, Emre Togan, Yiwen Chu, Alexei Trifonov, Efthimios Kaxiras, and Mikhail D Lukin. Properties of nitrogen-vacancy centers in diamond: the group theoretic approach. *New Journal of Physics*, 13(2): 025025, 2011.

[4] Marcus W Doherty, Neil B Manson, Paul Delaney, Fedor Jelezko, Jörg Wrachtrup, and Lloyd CL Hollenberg. The nitrogen-vacancy colour centre in diamond. *Physics Reports*, 528(1):1–45, 2013.

[5] Amicia D Elliott. Confocal microscopy: principles and modern practices. *Current protocols in cytometry*, 92(1):e68, 2020.

[6] Christian Hepp. Electronic structure of the silicon vacancy color center in diamond, 2014.

[7] Yeghishe Tsaturyan, Andreas Barg, Eugene S Polzik, and Albert Schliesser. Ultracoherent nanomechanical resonators via soft clamping and dissipation dilution. *Nature nanotechnology*, 12(8):776–783, 2017.

[8] Matthew Mitchell, David P Lake, and Paul E Barclay. Realizing Q> 300 000 in diamond microdisks for optomechanics via etch optimization. *Apl Photonics*, 4 (1), 2019.

[9] Michael J Burek, Justin D Cohen, Seán M Meenehan, Nayera El-Sawah, Cleaven Chia, Thibaud Ruelle, Srujan Meesala, Jake Rochman, Haig A Atikian, Matthew Markham, et al. Diamond optomechanical crystals. *Optica*, 3(12): 1404–1411, 2016.

[10] Huiyao Y Chen, ER MacQuarrie, and Gregory David Fuchs. Orbital state manipulation of a diamond nitrogen-vacancy center using a mechanical resonator. *Physical review letters*, 120(16):167401, 2018.

[11] Michel Challier, Selda Sonusen, Arne Barfuss, Dominik Rohner, Daniel Riedel, Johannes Koelbl, Marc Ganzhorn, Patrick Appel, Patrick Maletinsky, and Elke Neu. Advanced fabrication of single-crystal diamond membranes for quantum technologies. *Micromachines*, 9(4):148, 2018.

[12] Thaddeus D Ladd, Fedor Jelezko, Raymond Laflamme, Yasunobu Nakamura, Christopher Monroe, and Jeremy Lloyd O'Brien. Quantum computers. *nature*, 464(7285):45–53, 2010.

[13] David P DiVincenzo. The physical implementation of quantum computation. *Fortschritte der Physik: Progress of Physics*, 48(9-11):771–783, 2000.

[14] He-Liang Huang, Dachao Wu, Daojin Fan, and Xiaobo Zhu. Superconducting quantum computing: a review. *Science China Information Sciences*, 63:1–32, 2020.

[15] Colin D Bruzewicz, John Chiaverini, Robert McConnell, and Jeremy M Sage. Trapped-ion quantum computing: Progress and challenges. *Applied physics reviews*, 6(2), 2019.

[16] David D Awschalom, Lee C Bassett, Andrew S Dzurak, Evelyn L Hu, and Jason R Petta. Quantum spintronics: engineering and manipulating atom-like spins in semiconductors. *Science*, 339(6124):1174–1179, 2013.

[17] Loïc Henriet, Lucas Beguin, Adrien Signoles, Thierry Lahaye, Antoine Browaeys, Georges-Olivier Reymond, and Christophe Jurczak. Quantum computing with neutral atoms. *Quantum*, 4:327, 2020.

[18] Jeremy L O'brien. Optical quantum computing. *Science*, 318(5856):1567–1570, 2007.

[19] Philip Krantz, Morten Kjaergaard, Fei Yan, Terry P Orlando, Simon Gustavsson, and William D Oliver. A quantum engineer's guide to superconducting qubits. *Applied physics reviews*, 6(2), 2019.

[20] J Van Damme, S Massar, R Acharya, Ts Ivanov, D Perez Lozano, Y Canvel, M Demarets, D Vangoidsenhoven, Y Hermans, JG Lai, et al. Advanced cmos manufacturing of superconducting qubits on 300 mm wafers. *Nature*, 634(8032): 74–79, 2024.

[21] Dietrich Leibfried, Rainer Blatt, Christopher Monroe, and David Wineland. Quantum dynamics of single trapped ions. *Reviews of Modern Physics*, 75(1): 281, 2003.

[22] Guido Burkard, Thaddeus D Ladd, Andrew Pan, John M Nichol, and Jason R Petta. Semiconductor spin qubits. *Reviews of Modern Physics*, 95(2):025003, 2023.

[23] Ville Lahtinen and Jiannis Pachos. A short introduction to topological quantum computation. *SciPost Physics*, 3(3):021, 2017.

[24] Chris Monroe, David M Meekhof, Barry E King, Wayne M Itano, and David J Wineland. Demonstration of a fundamental quantum logic gate. *Physical review letters*, 75(25):4714, 1995.

[25] Peter W Shor. Algorithms for quantum computation: discrete logarithms and factoring. In *Proceedings 35th annual symposium on foundations of computer science*, pages 124–134. Ieee, 1994.

[26] Jan Benhelm, Gerhard Kirchmair, Christian F Roos, and Rainer Blatt. Towards fault-tolerant quantum computing with trapped ions. *Nature Physics*, 4(6):463–466, 2008.

[27] Christopher J Ballance, Thomas P Harty, Nobert M Linke, Martin A Sepiol, and David M Lucas. High-fidelity quantum logic gates using trapped-ion hyperfine qubits. *Physical review letters*, 117(6):060504, 2016.

[28] Ronald Hanson, Leo P Kouwenhoven, Jason R Petta, Seigo Tarucha, and Lieven MK Vandersypen. Spins in few-electron quantum dots. *Reviews of modern physics*, 79(4):1217–1265, 2007.

[29] Lachlan J Rogers, Kay D Jahnke, Marcus W Doherty, Andreas Dietrich, Liam P McGuinness, Christoph Müller, Tokuyuki Teraji, Hitoshi Sumiya, Junichi Isoya, Neil B Manson, et al. Electronic structure of the negatively charged silicon-vacancy center in diamond. *Physical Review B*, 89(23):235101, 2014.

[30] Johannes Görlitz, Dennis Herrmann, Philipp Fuchs, Takayuki Iwasaki, Takashi Taniguchi, Detlef Rogalla, David Hardeman, Pierre-Olivier Colard, Matthew Markham, Mutsuko Hatano, et al. Coherence of a charge stabilised tin-vacancy spin in diamond. *npj Quantum Information*, 8(1):45, 2022.

[31] TE Northup and R Blatt. Quantum information transfer using photons. *Nature photonics*, 8(5):356–363, 2014.

[32] Audrey Bienfait, Kevin J Satzinger, YP Zhong, H-S Chang, M-H Chou, Chris R Conner, É Dumur, Joel Grebel, Gregory A Peairs, Rhys G Povey, et al. Phonon-mediated quantum state transfer and remote qubit entanglement. *Science*, 364(6438):368–371, 2019.

[33] Michael Metcalfe, Stephen M Carr, Andreas Muller, Glenn S Solomon, and John Lawall. Resolved sideband emission of inas/gaas quantum dots strained by surface acoustic waves. *Physical review letters*, 105(3):037401, 2010.

[34] Srujan Meesala, Young-Ik Sohn, Haig A Atikian, Samuel Kim, Michael J Burek, Jennifer T Choy, and Marko Lončar. Enhanced strain coupling of nitrogen-vacancy spins to nanoscale diamond cantilevers. *Physical Review Applied*, 5(3):034010, 2016.

[35] Ming-Han Chou, Hong Qiao, Haoxiong Yan, Gustav Andersson, Christopher R Conner, Joel Grebel, Yash J Joshi, Jacob M Miller, Rhys G Povey, Xuntao Wu, et al. Deterministic multi-phonon entanglement between two mechanical resonators on separate substrates. *Nature Communications*, 16(1):1450, 2025.

[36] E Alex Wollack, Agnetta Y Cleland, Rachel G Gruenke, Zhaoyou Wang, Patricio Arrangoiz-Arriola, and Amir H Safavi-Naeini. Quantum state preparation and tomography of entangled mechanical resonators. *Nature*, 604 (7906):463–467, 2022.

[37] Kevin Joseph Satzinger, YP Zhong, H-S Chang, Gregory A Peairs, Audrey Bienfait, Ming-Han Chou, AY Cleland, Cristopher R Conner, Étienne Dumur, Joel Grebel, et al. Quantum control of surface acoustic-wave phonons. *Nature*, 563(7733):661–665, 2018.

[38] Shlomi Kotler, Gabriel A Peterson, Ezad Shojaee, Florent Lecocq, Katarina Cicak, Alex Kwiatkowski, Shawn Geller, Scott Glancy, Emanuel Knill, Raymond W Simmonds, et al. Direct observation of deterministic macroscopic entanglement. *Science*, 372(6542):622–625, 2021.

[39] Hailin Wang and Ignas Lekavicius. Coupling spins to nanomechanical resonators: Toward quantum spin-mechanics. *Applied Physics Letters*, 117(23), 2020.

[40] D Andrew Golter, Thein Oo, Mayra Amezcua, Kevin A Stewart, and Hailin Wang. Optomechanical quantum control of a nitrogen-vacancy center in diamond. *Physical review letters*, 116(14):143602, 2016.

[41] Anja Boisen, Søren Dohn, Stephan Sylvest Keller, Silvan Schmid, and Maria Tenje. Cantilever-like micromechanical sensors. *Reports on Progress in Physics*, 74(3):036101, 2011.

[42] KV Kepesidis, SD Bennett, Stefano Portolan, Mikhail D Lukin, and Peter Rabl. Phonon cooling and lasing with nitrogen-vacancy centers in diamond. *Physical Review B—Condensed Matter and Materials Physics*, 88(6):064105, 2013.

[43] Xinzhu Li, Ignas Lekavicius, and Hailin Wang. Diamond nanomechanical resonators protected by a phononic band gap. *Nano Letters*, 22(24): 10163–10166, 2022.

[44] Xinzhu Li, Ignas Lekavicius, Jens Noeckel, and Hailin Wang. Ultracoherent gigahertz diamond spin-mechanical lamb wave resonators. *Nano Letters*, 24(35): 10995–11001, 2024.

[45] Xinzhu Li and Hailin Wang. Mechanical photoluminescence excitation spectra of a strongly driven spin-mechanical system. *Physical Review Applied*, 19(6): 064068, 2023.

[46] Xinzhu Li, Mark C Kuzyk, and Hailin Wang. Honeycomblike phononic networks of spins with closed mechanical subsystems. *Physical Review Applied*, 11(6):064037, 2019.

[47] Carlo Bradac, Weibo Gao, Jacopo Forneris, Matthew E Trusheim, and Igor Aharonovich. Quantum nanophotonics with group iv defects in diamond. *Nature communications*, 10(1):5625, 2019.

[48] Michael Tinkham. *Group theory and quantum mechanics*. Courier Corporation, 2003.

[49] A Lenef and SC Rand. Electronic structure of the n-v center in diamond: Theory. *Physical Review B*, 53(20):13441, 1996.

[50] John Frederick Nye. *Physical properties of crystals: their representation by tensors and matrices*. Oxford university press, 1985.

[51] A Batalov, V Jacques, F Kaiser, P Siyushev, P Neumann, LJ Rogers, RL McMurtrie, NB Manson, F Jelezko, and J Wrachtrup. Low temperature studies of the excited-state structure of negatively charged¡? format?¿ nitrogen-vacancy color centers in diamond. *Physical review letters*, 102(19): 195506, 2009.

[52] Robert H Webb. Confocal optical microscopy. *Reports on progress in physics*, 59(3):427, 1996.

[53] Paul R Berman and Vladimir S Malinovsky. *Principles of laser spectroscopy and quantum optics*. Princeton University Press, 2011.

[54] Ignas Lekavicius, Thein Oo, and Hailin Wang. Diamond lamb wave spin-mechanical resonators with optically coherent nitrogen vacancy centers. *Journal of Applied Physics*, 126(21), 2019.

[55] Y Tao, Jens M Boss, BA Moores, and Christian L Degen. Single-crystal diamond nanomechanical resonators with quality factors exceeding one million. *Nature communications*, 5(1):3638, 2014.

[56] Maximilian Ruf, Mark IJspeert, Suzanne Van Dam, Nick De Jong, Hans Van Den Berg, Guus Evers, and Ronald Hanson. Optically coherent nitrogen-vacancy centers in micrometer-thin etched diamond membranes. *Nano letters*, 19(6):3987–3992, 2019.

[57] Benjamin Pingault, David-Dominik Jarausch, Christian Hepp, Lina Klintberg, Jonas N Becker, Matthew Markham, Christoph Becher, and Mete Atatüre. Coherent control of the silicon-vacancy spin in diamond. *Nature communications*, 8(1):15579, 2017.

[58] Srujan Meesala, Young-Ik Sohn, Benjamin Pingault, Linbo Shao, Haig A Atikian, Jeffrey Holzgrafe, Mustafa Gündoğan, Camille Stavrakas, Alp Sipahigil, Cleaven Chia, et al. Strain engineering of the silicon-vacancy center in diamond. *Physical Review B*, 97(20):205444, 2018.

[59] Josh A Zuber, Minghao Li, Marcel li Grimau Puigibert, Jodok Happacher, Patrick Reiser, Brendan J Shields, and Patrick Maletinsky. Shallow silicon vacancy centers with lifetime-limited optical linewidths in diamond nanostructures. *Nano Letters*, 23(23):10901–10907, 2023.

[60] Aedan Gardill, Ishita Kemeny, Matthew C Cambria, Yanfei Li, Hossein T Dinani, Ariel Norambuena, Jeronimo R Maze, Vincenzo Lordi, and Shimon Kolkowitz. Probing charge dynamics in diamond with an individual color center. *Nano Letters*, 21(16):6960–6966, 2021.

[61] Guoqiang Wu, Jinghui Xu, Eldwin Jiaqiang Ng, and Wen Chen. Mems resonators for frequency reference and timing applications. *Journal of Microelectromechanical Systems*, 29(5):1137–1166, 2020.

[62] Simon Rips and Michael J Hartmann. Quantum information processing with nanomechanical qubits. *Physical Review Letters*, 110(12):120503, 2013.

[63] R Tabrizian, M Rais-Zadeh, and F Ayazi. Effect of phonon interactions on limiting the fq product of micromechanical resonators. In *TRANSDUCERS 2009-2009 International Solid-State Sensors, Actuators and Microsystems Conference*, pages 2131–2134. IEEE, 2009.

[64] Gregory S MacCabe, Hengjiang Ren, Jie Luo, Justin D Cohen, Hengyun Zhou, Alp Sipahigil, Mohammad Mirhosseini, and Oskar Painter. Nano-acoustic resonator with ultralong phonon lifetime. *Science*, 370(6518):840–843, 2020.

[65] William A Phillips. Two-level states in glasses. *Reports on Progress in Physics*, 50(12):1657, 1987.

[66] Ryan O Behunin, Francesco Intravaia, and Peter T Rakich. Dimensional transformation of defect-induced noise, dissipation, and nonlinearity. *Physical Review B*, 93(22):224110, 2016.

[67] Gyaneshwar P Srivastava. *The physics of phonons*. CRC press, 2022.

[68] Mo Chen, John Clai Owens, Harald Putterman, Max Schäfer, and Oskar Painter. Phonon engineering of atomic-scale defects in superconducting quantum circuits. *Science Advances*, 10(37):eado6240, 2024.

[69] DeLamar T Bell and Robert CM Li. Surface-acoustic-wave resonators. *Proceedings of the IEEE*, 64(5):711–721, 1976.

[70] Lorenzo Dania, Dmitry S Bykov, Florian Goschin, Markus Teller, Abderrahmane Kassid, and Tracy E Northup. Ultrahigh quality factor of a levitated nanomechanical oscillator. *Physical Review Letters*, 132(13):133602, 2024.

[71] Carlos Gonzalez-Ballestero, Markus Aspelmeyer, Lukas Novotny, Romain Quidant, and Oriol Romero-Isart. Levitodynamics: Levitation and control of microscopic objects in vacuum. *Science*, 374(6564):eabg3027, 2021.

[72] Paul S Epstein. On the resistance experienced by spheres in their motion through gases. *Physical Review*, 23(6):710, 1924.

[73] Yan Pennec, Jérôme O Vasseur, Bahram Djafari-Rouhani, Leonard Dobrzyński, and Pierre A Deymier. Two-dimensional phononic crystals: Examples and applications. *Surface Science Reports*, 65(8):229–291, 2010.

[74] Amir H Safavi-Naeini and Oskar Painter. Design of optomechanical cavities and waveguides on a simultaneous bandgap phononic-photonic crystal slab. *Optics express*, 18(14):14926–14943, 2010.

[75] COMSOL Multiphysics v.5.6. www.comsol.com.

[76] Mario Khoury and Marco Abbarchi. A bright future for silicon in quantum technologies. *Journal of Applied Physics*, 131(20), 2022.

[77] Thomas Koch, Clement Godfrin, Viktor Adam, Julian Ferrero, Daniel Schroller, Noah Glaeser, Stefan Kubicek, Ruoyu Li, Roger Loo, Shana Massar, et al. Industrial 300 mm wafer processed spin qubits in natural silicon/silicon-germanium. *npj Quantum Information*, 11(1):59, 2025.

[78] Scott S Verbridge, Harold G Craighead, and Jeevak M Parpia. A megahertz nanomechanical resonator with room temperature quality factor over a million. *Applied Physics Letters*, 92(1), 2008.

[79] Alexander Eichler. Ultra-high-q nanomechanical resonators for force sensing. *Materials for Quantum Technology*, 2(4):043001, 2022.

[80] Scott S Verbridge, Jeevak M Parpia, Robert B Reichenbach, Leon M Bellan, and Harold G Craighead. High quality factor resonance at room temperature with nanostrings under high tensile stress. *Journal of Applied Physics*, 99(12), 2006.

[81] Quirin P Unterreithmeier, Thomas Faust, and Jörg P Kotthaus. Damping of nanomechanical resonators. *Physical review letters*, 105(2):027205, 2010.

[82] Stefania Castelletto, Lorenzo Rosa, Jonathan Blackledge, Mohammed Zaher Al Abri, and Albert Boretti. Advances in diamond nanofabrication for ultrasensitive devices. *Microsystems & nanoengineering*, 3(1):1–16, 2017.

[83] Matthew Mitchell, Behzad Khanaliloo, David P Lake, Tamiko Masuda, John P Hadden, and Paul E Barclay. Single-crystal diamond low-dissipation cavity optomechanics. *Optica*, 3(9):963–970, 2016.

[84] Graham Joe, Michael Haas, Kazuhiro Kuruma, Chang Jin, Dongyeon Daniel Kang, Sophie Ding, Cleaven Chia, Hana Warner, Benjamin Pingault, Bartholomeus Machielse, et al. Observation of the acoustic purcell effect with a color-center and a nanomechanical resonator. *arXiv preprint arXiv:2503.09946*, 2025.

[85] Smarak Maity, Linbo Shao, Stefan Bogdanović, Srujan Meesala, Young-Ik Sohn, Neil Sinclair, Benjamin Pingault, Michelle Chalupnik, Cleaven Chia, Lu Zheng, et al. Coherent acoustic control of a single silicon vacancy spin in diamond. *Nature communications*, 11(1):193, 2020.

[86] Huiyao Chen, Noah F Opondo, Boyang Jiang, Evan R MacQuarrie, Raphaël S Daveau, Sunil A Bhave, and Gregory D Fuchs. Engineering electron–phonon coupling of quantum defects to a semiconfocal acoustic resonator. *Nano letters*, 19(10):7021–7027, 2019.

[87] CL Lee, E Gu, MD Dawson, I Friel, and GA Scarsbrook. Etching and micro-optics fabrication in diamond using chlorine-based inductively-coupled plasma. *Diamond and Related Materials*, 17(7-10):1292–1296, 2008.

[88] James F Ziegler, Matthias D Ziegler, and Jochen P Biersack. Srim–the stopping and range of ions in matter (2010). *Nuclear Instruments and Methods in Physics Research Section B: Beam Interactions with Materials and Atoms*, 268 (11-12):1818–1823, 2010.

[89] Yiwen Chu, Nathalie Pulmones de Leon, Brendan J Shields, Birgit Hausmann, R Evans, Emre Togan, Michael John Burek, M Markham, Alastair Stacey, Alexander S Zibrov, et al. Coherent optical transitions in implanted nitrogen vacancy centers. *Nano letters*, 14(4):1982–1986, 2014.

[90] KMCMC Fu, C Santori, PE Barclay, and RG Beausoleil. Conversion of neutral nitrogen-vacancy centers to negatively charged nitrogen-vacancy centers through selective oxidation. *Applied Physics Letters*, 96(12), 2010.

[91] Benjamin J Lawrie, Matthew Feldman, Claire E Marvinney, and Yun-Yi Pai. Free-space confocal magneto-optical spectroscopies at millikelvin temperatures. In *Quantum Nanophotonic Materials, Devices, and Systems 2021*, volume 11806, page 1180604. SPIE, 2021.

[92] D Andrew Golter, Thein Oo, Mayra Amezcua, Ignas Lekavicius, Kevin A Stewart, and Hailin Wang. Coupling a surface acoustic wave to an electron spin in diamond via a dark state. *Physical Review X*, 6(4):041060, 2016.

[93] Jasper Chan, Amir H Safavi-Naeini, Jeff T Hill, Seán Meenehan, and Oskar Painter. Optimized optomechanical crystal cavity with acoustic radiation shield. *Applied Physics Letters*, 101(8), 2012.

[94] David J Christle, Abram L Falk, Paolo Andrich, Paul V Klimov, Jawad Ul Hassan, Nguyen T Son, Erik Janzén, Takeshi Ohshima, and David D Awschalom. Isolated electron spins in silicon carbide with millisecond coherence times. *Nature materials*, 14(2):160–163, 2015.

[95] Mark C Kuzyk and Hailin Wang. Scaling phononic quantum networks of solid-state spins with closed mechanical subsystems. *Physical Review X*, 8(4): 041027, 2018.

[96] I Wilson-Rae, P Zoller, and A Imamoğlu. Laser cooling of a nanomechanical resonator mode to its quantum ground state. *Physical review letters*, 92(7): 075507, 2004.

[97] Kenneth W Lee, Donghun Lee, Preeti Ovartchaiyapong, Joaquin Minguzzi, Jero R Maze, and Ania C Bleszynski Jayich. Strain coupling of a mechanical resonator to a single quantum emitter in diamond. *Physical Review Applied*, 6 (3):034005, 2016.

[98] S Ashhab, JR Johansson, AM Zagoskin, and Franco Nori. Two-level systems driven by large-amplitude fields. *Physical Review A—Atomic, Molecular, and Optical Physics*, 75(6):063414, 2007.

[99] KL Ekinci, XMH Huang, and ML Roukes. Ultrasensitive nanoelectromechanical mass detection. *Applied physics letters*, 84(22):4469–4471, 2004.

[100] Hengyun Zhou, Joonhee Choi, Soonwon Choi, Renate Landig, Alexander M Douglas, Junichi Isoya, Fedor Jelezko, Shinobu Onoda, Hitoshi Sumiya, Paola Cappellaro, et al. Quantum metrology with strongly interacting spin systems. *Physical review X*, 10(3):031003, 2020.

[101] Alexei Kitaev. Anyons in an exactly solved model and beyond. *Annals of Physics*, 321(1):2–111, 2006.

[102] Yi-Chan Lee, Courtney G Brell, and Steven T Flammia. Topological quantum error correction in the kitaev honeycomb model. *Journal of Statistical Mechanics: Theory and Experiment*, 2017(8):083106, 2017.

[103] Sergey B Bravyi and A Yu Kitaev. Quantum codes on a lattice with boundary. *arXiv preprint quant-ph/9811052*, 1998.

[104] Daiki Hatanaka, Imran Mahboob, Koji Onomitsu, and Hiroshi Yamaguchi. Phonon waveguides for electromechanical circuits. *Nature nanotechnology*, 9(7): 520–524, 2014.

[105] Shuhao Wu, Xinzhu Li, Ian Gallagher, Benjamin Lawrie, and Hailin Wang. Coherent population trapping and spin relaxation of a silicon vacancy center in diamond at millikelvin temperatures. *Physical Review B*, 111(3):035421, 2025.

[106] Philip Andrango and Hailin Wang. Mechanical wannier-stark ladder of diamond spin-mechanical lamb wave resonators. *Physical Review A*, 110(6): 062603, 2024.

[107] Nikolas P Breuckmann and Jens Niklas Eberhardt. Quantum low-density parity-check codes. *Prx Quantum*, 2(4):040101, 2021.

[108] Dan Botez and Gerald J Herskowitz. Components for optical communications systems: A review. *Proceedings of the IEEE*, 68(6):689–731, 1980.

[109] WJ Tomlinson and Charles A Brackett. Telecommunications applications of integrated optics and optoelectronics. *Proceedings of the IEEE*, 75(11): 1512–1523, 2005.

[110] Xin Cao, Michael Zopf, and Fei Ding. Telecom wavelength single photon sources. *Journal of Semiconductors*, 40(7):071901, 2019.

[111] J Huwer, RM Stevenson, J Skiba-Szymanska, MB Ward, AJ Shields, M Felle, I Farrer, David Alastair Ritchie, and Richard Vincent Penty. Quantum-dot-based telecommunication-wavelength quantum relay. *Physical Review Applied*, 8(2):024007, 2017.

[112] Félix Bussières, Christoph Clausen, Alexey Tiranov, Boris Korzh, Varun B Verma, Sae Woo Nam, Francesco Marsili, Alban Ferrier, Philippe Goldner, Harald Herrmann, et al. Quantum teleportation from a telecom-wavelength photon to a solid-state quantum memory. *Nature Photonics*, 8(10):775–778, 2014.